Technical Physics Letters, Vol. 29, No. 3, 2003, pp. 175–177. Translated from Pis'ma v Zhurnal Tekhnicheskoĭ Fiziki, Vol. 29, No. 5, 2003, pp. 1–7.

Electrical Properties of Thin $Ba_xSr_{1-x}TiO_3$ Films on Silicon Dioxide Substrates

S. V. Razumov, A. V. Tumarkin, M. V. Sysa, and A. G. Gagarin

St. Petersburg State Electrotechnical University, St. Petersburg, Russia

e-mail: thinfilm@eltech.ru

Received August 6, 2002

Abstract—We have studied the electrical properties of thin ferroelectric films of barium strontium titanate ($Ba_xSr_{1-x}TiO_3$) obtained on fused quartz (SiO_2) substrates by RF magnetron sputtering. Dependences of the tuning coefficient and dielectric loss tangent on the synthesis temperature and the film thickness are reported. The results are compared to analogous data for films grown on polycrystalline alumina substrates. © *2003 MAIK "Nauka/Interperiodica".*

In recent years, ferroelectrics have attracted much attention as possible materials for microwave devices [1, 2]. This interest is largely due to the strong dependence of the permittivity of ferroelectric materials on the applied electric field strength and the relatively low level of dielectric losses in the microwave frequency range [3, 4]. These properties make such ferroelectrics promising materials for various microwave devices, such as varactors, phase-shifting devices, tunable filters, and phased antenna gratings, capable of operating at room temperature [5].

Thus, ferroelectric films for microwave devices must combine a sufficiently strong field dependence of the permittivity with low energy losses in the microwave frequency range [6]. One of the most promising candidate materials, characterized by highly nonlinear permittivity and a low level of losses, is barium strontium titanate $Ba_xSr_{1-x}TiO_3$ (BSTO) [4, 7]. Based on BSTO films, some microwave devices such as phase shifters [8, 9] have been successfully implemented, and some others (filters, delay lines, etc.) are now being extensively developed.

An important factor in designing microwave devices is selection of a proper dielectric substrate for BSTO films. Widely used substrate materials for microwave devices are single crystal (sapphire) and polycrystalline (polycor) alumina [6, 7]. We believe that good prospects are also offered by quartz substrates, which are characterized by low dielectric losses and stably low permittivity. The low permittivity of quartz (as compared to that of sapphire and polycor) allows the dimensions of microwave elements to be varied within broad limits, thus facilitating the optimum system design in the range of frequencies above 30 GHz. However, the problem of depositing ferroelectric films onto quartz substrates is still not solved.

This letter reports on a comparative study of the electrical properties of BSTO films obtained by the method of ion-plasma sputtering on polycrystalline alumina (polycor) and fused quartz (silica) substrates.

The samples of BSTO films were prepared by RF magnetron sputtering of $Ba_{0.3}Sr_{0.7}TiO_3$ ceramic targets with a diameter of 76 mm. The target composition was selected based on the results of our previous investigations [7], where the range of technological parameters ensuring the synthesis of ferroelectric films with electrical properties sufficient for microwave applications had been established. The films were deposited in a single technological cycle simultaneously onto quartz and alumina substrates. The substrate temperature during deposition was monitored by a thermocouple fixed on the substrate holder. The holder temperature could be controlled in the interval from 700 to 905°C. The deposition time was varied from 100 to 300 min, which corresponded to the film thicknesses (measured with a profilometer) increasing from 3500 to 10 500 Å, respectively, at a deposition rate of 35 Å/min. The target–substrate distance was about 40 mm. The process was performed in a pure oxygen atmosphere. After deposition, the samples were cooled in oxygen at atmospheric pressure at a rate of 2–3 K/min. Prior to the working deposition cycle, the targets were pretreated by sputtering for 30 min, during which the substrates were shielded.

The electrical properties of the synthesized films were studied using planar capacitor structures with copper electrodes formed on the film surface by photolithographic techniques. The capacitor structures had the following linear parameters: electrode thickness, 0.5 μm; interelectrode gap width, 6 μm; gap length, 0.8 mm. The sample structures were characterized by the controlability (expressed in terms of the tuning coefficient $n = C(0)/C(E_{max})$) and dielectric loss level ($\tan\delta$). These electrical characteristics were measured at room temperature and a frequency of 1 GHz. The voltage U_1 applied to the capacitors varied from 0 to 300 V, which corresponded to the electric field strength

1063-7850/03/2903-0175$24.00

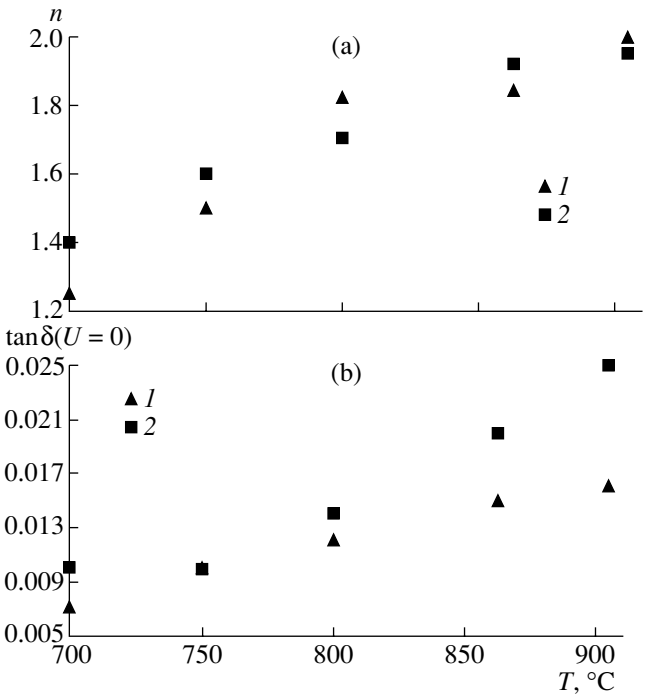

Fig. 1. Plots of (a) the tuning coefficient n and (b) the dielectric loss tangent versus BSTO film synthesis temperature T for the samples grown on (*1*) alumina (polycor) and (*2*) quartz substrates.

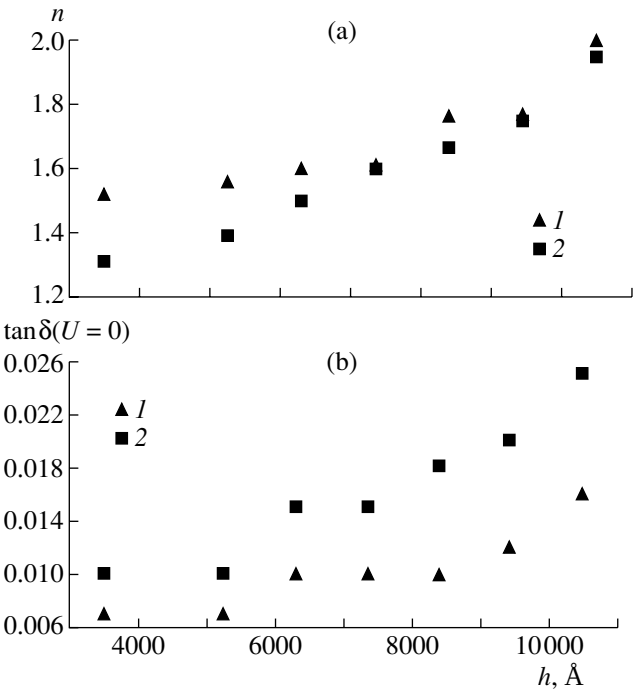

Fig. 2. Plots of (a) the tuning coefficient n and (b) the dielectric loss tangent versus BSTO film thickness for the samples grown at a temperature of T = 905°C on (*1*) alumina (polycor) and (*2*) quartz substrates.

in the interelectrode gap being varied within E = 0–50 V/μm.

The Curie temperature of the ferroelectric films was ~160°C, which is close to the value for bulk BSTO samples. The zero-field permittivity (calculated as described in [10]) fell within 230–240 for the BSTO films on quartz substrates and ranged within 320–450 for the films deposited onto alumina.

Figures 1a and 1b show plots of the tuning coefficient n and the dielectric loss tangent, respectively, versus deposition temperature T for the films obtained on quartz and alumina substrates. Data for the BSTO films on alumina are presented for the comparison, since high-quality BSTO films possessing good electrical properties on this substrate material have been obtained previously [7]. As can be seen from Fig. 1, the levels of controlability and losses tend to increase with temperature for films on both quartz and alumina substrates. It is interesting to note that a similar trend was observed for the BSTO films on sapphire substrates [6, 7]. This analogy suggests that the BSTO films grown on the materials reported here and on the substrates used previously [7] obey common laws. In the case of deposition onto quartz substrates, the tuning coefficient reaches maximum (n = 1.95) for the films grown at 905°C. Further increase in the temperature of synthesis is expedient only from the standpoint of increasing controllability, since the energy losses ($\tan\delta$ = 0.025 at 1 GHz) in the films deposited at 905°C onto quartz substrates already exceed the level acceptable for microwave applications [6].

Figures 2a and 2b present the plots of the tuning coefficient n and the dielectric loss tangent, respectively, versus thickness for the BSTO films deposited at a temperature of T = 905°C on the quartz and alumina substrates. As seen from these data, both the controllability and the microwave energy losses tend to increase with the film thickness. The level of losses is higher for the films grown on quartz than for those on alumina. The increased level of losses in the samples deposited onto quartz is probably explained by the insufficiently high quality of the BSTO films grown on these amorphous substrates and by a significant difference in the coefficients of thermal expansion of the ferroelectric film and quartz substrate. Indeed, the thermal expansion coefficient of polycor (75×10^{-7} K^{-1}) is close to that of a BSTO film (94×10^{-7} K^{-1}), so that the film is subject to insignificant straining as a result of the substrate heating and cooling and, hence, no additional structural defects are formed in the film material. In contrast, the thermal expansion coefficient of quartz (5.5×10^{-7} K^{-1}) is more than one order of magnitude lower as compared to that of the BSTO film [11]. As a result, the BSTO film grown on a quartz substrate exhibits cracking on cooling. The cracks are readily observed in an optical microscope and revealed by film thickness measurements in a profilometer. These additional defects lead to an increase in the level of losses

in the films grown on quartz substrates. Note, however, that the BSTO films grown on quartz exhibit cracking only for the film thickness exceeding 10000 Å.

Thus, the results of our investigation demonstrated that the tuning coefficient and loss tangent increased with the temperature of deposition for BSTO films grown on quartz and alumina (sapphire and polycor) substrates. Measurements of the samples grown at a temperature ensuring the maximum controlability showed that the level of loses in the films grown on quartz is significantly higher than that in the films grown on alumina. We believe that the main factors responsible for increased losses are the amorphous substrate structure (limiting the structural perfection of the deposit) and a significant difference in the coefficients of thermal expansion of the quartz substrate and ferroelectric film. Since the thermal expansion coefficient of quartz is smaller than that of a BSTO film by more than one order of magnitude, the cooling process is accompanied by the formation of cracks leading to a significant increase in the level of losses.

A possible solution to the problem of the compatibility of two materials (quartz substrate and BSTO deposit) possessing different properties can be provided by using a buffer dielectric layer capable of matching the material properties. For example, cerium dioxide (CeO_2) possesses a cubic lattice with a = 5.420 Å, which fits the structure of barium strontium titanate well. In addition, the thermal expansion coefficient of CeO_2 (85×10^{-7} K^{-1} at T = 300 K) is close to that of BSTO.

Despite the fact that the level of losses in BSTO films grown on quartz is higher than that in the films on alumina, the former films with thicknesses below 10000 Å possess properties acceptable in microwave applications: $n = 1.76$ and $\tan\delta = 0.02$ for $U_1 = 0$ V at a frequency of 1 GHz.

Therefore, a compromise between film thickness and acceptable microwave losses allows BSTO films on quartz substrates to be used in the development of microwave devices.

REFERENCES

1. J. M. Ponds, S. W. Kirchoefer, W. Chang, *et al.*, Integr. Ferroelectr. **22**, 317 (1998).
2. F. Miranda, F. W. van Keuls, R. R. Romanofsky, *et al.*, Integr. Ferroelectr. **22**, 269 (1998).
3. Im Jaemo, O. Auciello, P. K. Baumann, *et al.*, Appl. Phys. Lett. **76**, 625 (2000).
4. J. D. Baniecki, R. B. Laibowitz, T. W. Shaw, *et al.*, Appl. Phys. Lett. **72**, 498 (1998).
5. A. B. Kozyrev, A. V. Ivanov, T. B. Samoilova, *et al.*, Integr. Ferroelectr. **24**, 297 (1999).
6. S. V. Razumov and A. V. Tumarkin, Pis'ma Zh. Tekh. Fiz. **26** (16), 17 (2000) [Tech. Phys. Lett. **26**, 705 (2000)].
7. S. V. Razumov, A. V. Tumarkin, O. U. Buslov, *et al.*, Integr. Ferroelectr. **39**, 367 (2001).
8. A. B. Kozyrev, A. V. Ivanov, O. I. Soldatenkov, *et al.*, Pis'ma Zh. Tekh. Fiz. **27** (24), 16 (2001) [Tech. Phys. Lett. **27**, 1032 (2001)].
9. A. B. Kozyrev, M. M. Gaĭdukov, A. G. Gagarin, *et al.*, Pis'ma Zh. Tekh. Fiz. **28** (6), 51 (2002) [Tech. Phys. Lett. **28**, 239 (2002)].
10. O. G. Vendik, S. P. Zubko, and M. A. Nikol'skiĭ, Zh. Tekh. Fiz. **69** (4), 1 (1999) [Tech. Phys. **44**, 349 (1999)].
11. E. K. Gol'man, V. E. Loginov, A. M. Prudan, *et al.*, Pis'ma Zh. Tekh. Fiz. **21** (21), 84 (1995) [Tech. Phys. Lett. **21**, 899 (1995)].

Translated by P. Pozdeev

Technical Physics Letters, Vol. 29, No. 3, 2003, pp. 178–180. Translated from Pis'ma v Zhurnal Tekhnicheskoĭ Fiziki, Vol. 29, No. 5, 2003, pp. 8–14.

Peculiarities of the Magnetization Reversal in Heterophase Nanocomposite Permanent Magnets

Yu. P. Kabanov and V. S. Gornakov

Institute of Solid State Physics, Russian Academy of Sciences, Chernogolovka, Moscow oblast, 142432 Russia

e-mail: gornakov@issp.ac.ru

Received August 6, 2002

Abstract—We have studied the process of magnetization reversal in a thin-film Fe/Sm_2Co_7 exchange coupled bilayer structure under the action of an in-plane external field. An analysis of the local magnetization changes, as measured using the magnetooptical indicator film technique, showed that the magnetization reversal proceeds by inhomogeneous rotation of the magnetic moments in Fe and SmCo layers, both in plane and in the perpendicular direction. It is established that, because of the exchange interaction between layers, the magnetization reversal along the easy axis in the entire structure is determined primarily by the formation of exchange-induced spin helices and domain walls in the magnetically soft layer, whereas the magnetization reversal at an angle of α with respect to the easy axis plays a significant role in the magnetically hard layer and becomes dominating for $\alpha = 90°$. © *2003 MAIK "Nauka/Interperiodica".*

The new class of permanent magnets representing compositions of nanodisperse magnetically soft (MS) and magnetically hard (MH) ferromagnets was originally introduced by Kneller and Hawig [1]. It was shown that, by employing an exchange interaction at the interface between the MS phase (possessing a large magnetic induction $\mathbf{B} = 4\pi\mathbf{M}$) and the MH phase (characterized by a maximum level of the crystallographic anisotropy), it is possible to synthesize materials with record values of the energy product $(\mathbf{BH}_c)_{max}$, where H_c is the coercivity field of the composite. In recent years, owing to the development of methods for the epitaxial growth of heterophase structures, ferromagnetic nanocomposites that are composed of thin, exchange coupled MS and MH layers have been synthesized [2]. Optimization of the properties of such structures requires deeper insight into the process of magnetization reversal in these systems.

A special feature of exchange coupled bilayer structures is the effective inhomogeneous field related to the interfacial exchange interaction, which accounts for the formation of a helical spin spring and leads to essentially inhomogeneous spin-orientational phase transformations [3]. In an analysis of the microscopic mechanisms involved in the magnetization reversal in such heterophase nanocomposite structures, it is necessary to solve the basic problem of describing the influence of the interface on the spin twist and the domain wall (DW) formation in the quasi-two-dimensional layers with thicknesses comparable with (or smaller than) the DW width.

Significant progress in this direction, with respect to both synthesis and study by theoretical and experimental methods, was achieved for bilayer structures composed of exchange coupled SmCo and Fe thin films [1–6]. In these structures, the *c* [0001] axes of the hexagonal SmCo grains occur in the film plane and represent the easy magnetization axes. However, the formation of inhomogeneous spin structures in the course of magnetization reversal in these systems is still incompletely studied.

This letter reports on the results of an experimental investigation of the peculiarities of magnetization reversal in a uniaxial MS/MH Fe(50 nm)/Sm_2Co_7(35 nm)/Cr(20 nm) epitaxial structure deposited by magnetron sputter on a MgO(110) substrate.

The macroscopic magnetic measurements of the Fe/Sm_2Co_7 (for brevity, Fe/SmCo) structure (Fig. 1) were performed with a SQUID magnetometer. On the microscopic level, the magnetization reversal process (Fig. 2) was studied by visualization of the normal component of the local stray field $\mathbf{H}_\perp$ with the aid of a magnetooptical indicator film (MOIF) placed directly onto the sample surface [6]. In the absence of an external field, the MOIF magnetization vector **M** lies in the film plane and deviates from this plane under the action of the field $\mathbf{H}_\perp$. This deviation produces, owing to the double Faraday effect, a magnetooptical (MO) image of the field structure that can be observed in a reflected polarized light, in which the microscopic regions with opposite directions of $\mathbf{H}_\perp$ are manifested by black and white areas.

When the magnetization **M** is homogeneously distributed in the sample plane, the MO contrast is maximum along the axis of symmetry of the MO image (Fig. 2) formed by the stray fields of a Fe/SmCo structure at the edge of a round through hole made in the sample. The magnitude and change of the MO contrast

reflect the amplitude and variation of the $\mathbf{H}_\perp$ field and, hence, of the magnetization **M** averaged over the structure thickness. Thus, a real distribution of **M** in the Fe/SmCo structure is characterized by two parameters: (i) the maximum deviation of the MO signal intensity along the symmetry axis of the MO image (indicated by magnetic pointer in Fig. 2) and (ii) the angle of rotation of this axis relative to the easy axis of the structure studied. An analysis of the behavior of these parameters under the action of an external field **H** oriented at various angles provides information about the distribution of magnetic moments in layers of the structure and reveals the role of the interface.

The hysteresis loops depicted in Fig. 1 were measured with an external field **H** applied parallel to the easy axis (Figs. 1a and 1b), at an angle of 45° relative to this axis (Figs. 1c and 1d), and along the hard axis (Figs. 1e and 1f). An important feature of the magnetization reversal along the easy axis of the nanocomposite structure studied is the two-stage character of this process (Figs. 1a and 1b). In the region of relatively small values of *H*, the magnetization reversal takes place in the MS part of the structure; as the field strength increases, the process involves the MH part as well. This process is essentially inhomogeneous in depth owing to the spin twist in the MS layer [1, 3, 6]. The magnetization reversal must significantly depend both on the anisotropy of the MS layer [3–5] and on the orientation of **H** relative to the easy axis [4, 6].

A deviation of **H** from the easy axis by an angle α leads to a change in the characteristic magnetization reversal fields and the total magnetization of the sample. In the experimental data for $\alpha = 45°$ presented in Figs. 1c and 1d, the value of magnetization exhibits stabilization after the first stage at a lower field strength, whereas the final magnetization reversal to saturation takes place in a stronger field. Note that the total magnetization is lower than that for the magnetization reversal along the easy axis. In the case of the external field **H** oriented along the hard axis ($\alpha = 90°$), we observed only the initial stage of the magnetization reversal process (Figs. 1e and 1f). Here, the **M** value in the saturation state decreases to a still lower level.

Apparently, the mechanisms of the magnetization reversal along the easy axis and at angle to this axis are different. In order to reveal the distinctive features, we have performed microscopic magnetooptical measurements for the process of magnetization reversal both along ($\alpha = 0°$) the easy axis (Figs. 2a–2d) and at an angle ($\alpha = 12°$) relative to this axis (Figs. 2e– 2h). After magnetizing the sample in a field of +7 T to saturation along the easy axis, the field strength was decreased to zero (Figs. 2a and 2e) and then increased again, but with the reverse sign. For $\alpha = 0°$, the increase in the reverse field was initially accompanied by a decrease in the MO contrast, followed by its inversion and growth (Fig. 2b), without any significant deviation of **M** from the easy axis direction. For $\alpha = 12°$, the increase in the reverse field led to a rotation of the magnetization **M** without significant changes in the MO contrast (Fig. 2f). In both cases, subsequent decrease of the field strength to zero returned the sample magnetization virtually in the initial state (cf. Figs. 2a and 2e).

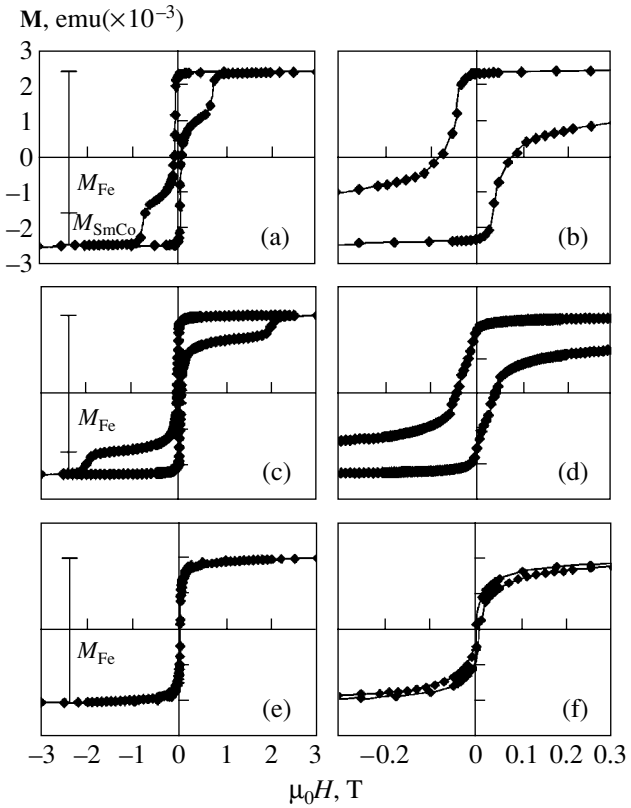

Fig. 1. Magnetization hysteresis loops in a Fe/Sm_2Co_7 structure measured (a, b) along the easy axis, (c, d) at an angle of 45° relative to this axis, and (e, f) in the perpendicular direction. Vertical bars in the left-hand panels show the ratio of saturation magnetizations of the MS (M_{Fe}) and MH (M_{SmCo}) layers.

These results indicate that the process of magnetization reversal in relatively small fields (i.e., in the first stage) proceeds by means of the helical spin twist in the Fe layer and has a reversible character. However, in the first case (where the average magnetization decreases), the spin twist is local and has different signs in various submicron regions of the sample. In the second case (where the rotating **M** has almost constant magnitude), the twist is predominantly unidirectional. As the strength of the reverse field *H* increases further, the magnetization rotation becomes irreversible. This is clearly illustrated in Figs. 2c and 2g obtained by applying a field of –0.7 T, followed by decreasing the field strength to zero. In the course of magnetization along the easy axis, the MO image displays regions with reverse magnetization (Fig. 2c). As the field strength increases, these regions grow and merge together, which results in complete magnetization reversal (Fig. 2d). In the field oriented at an angle relative to the

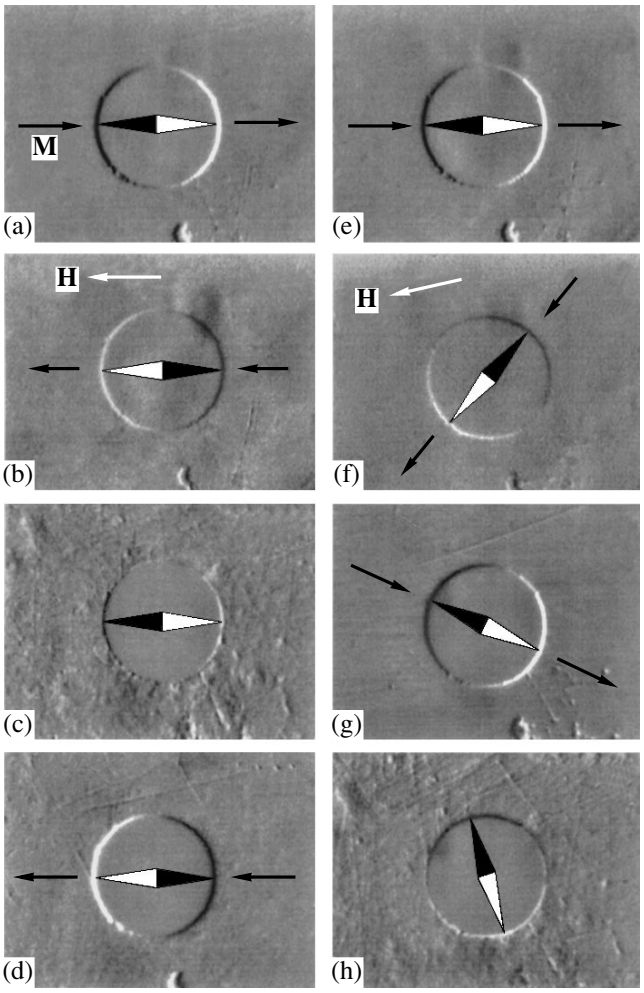

Fig. 2. Magnetooptical images of a sample with a through hole observed in the course of magnetization reversal (a–d) along the easy axis and (e–h) at an angle of 12° relative to this axis in a field of $\mu_0 H = 0$ (a, e), 0.1 (b, f), 0.7 (c, g), and 0.87 T (d, h). The hole diameter is 300 μm.

easy axis, the magnetization reversal was proceeded through the rotation of **M** (Fig. 2g) and only a maximum field strength attained in this experiment gave rise to the ripple magnetic structure (Fig. 2h).

The results of the MOIF pattern analysis showed that the magnetization reversal in a Fe/SmCo bilayer structure proceeds in the first stage by means of a reversible spin twist in the MS layer until its virtually complete saturation to M_{Fe} (Fig. 1). In the second stage, the MH layer is magnetized to M_{SmCo}. However, owing to a large value of the crystallographic anisotropy field (~25 T) [7], this process can take place only as a result of the nucleation and growth of microdomains with reverse magnetization in the SmCo layer. The domain structure is most effectively formed in the case when the external field is applied along the easy axis, whereby the dispersion in orientations of the *c* [0001] axes in SmCo [6] and the exchange interaction at the interface lead to the formation of most inhomogeneous and twisted magnetization distribution in the Fe layer. This, in turn, gives rise to a more effective exchange interaction and accounts for the expansion of microdomains in the MH layer at the interface. In the case of a quasihomogeneous spin twist (Figs. 1c, 1d, and 2h), the microdomains in the MH layer takes place at a greater field strength. When the field is oriented along the hard axis (which corresponds to a homogeneous spin twist in the layers), no magnetization reversal in the MH layer is observed in the range of field strengths accessible in experiment. Therefore, the exchange coupled MS layer and the interface structure determine the mechanism of magnetization reversal in MS/MH bilayer thin-film nanocomposite structures by decreasing the value of the coercive field $\mathbf{H}_c$. This effect should be taken in theoretical calculations and in the development of new types of permanent magnets.

Acknowledgments. The authors are grateful to S.D. Bader for kindly providing the samples for investigation.

REFERENCES

1. E. F. Kneller and R. Hawig, IEEE Trans. Magn. **TM-27** (4), 3588 (1991).
2. E. E. Fullerton *et al.*, Appl. Phys. Lett. **72** (3), 380 (1998).
3. C. Platt *et al.*, Appl. Phys. Lett. **79** (24), 3992 (2001).
4. J. S. Jiang *et al.*, IEEE Trans. Magn. **TM-35** (5), 3229 (1999).
5. M. Bevaissa *et al.*, IEEE Trans. Magn. **TM-34** (4), 1204 (1998).
6. V. S. Gornakov *et al.*, J. Magn. Magn. Mater. **246**, 80 (2002).
7. K. J. Strnat and R. M. W. Strnat, J. Magn. Magn. Mater. **100**, 38 (1991).

Translated by P. Pozdeev

Technical Physics Letters, Vol. 29, No. 3, 2003, pp. 181–183. Translated from Pis'ma v Zhurnal Tekhnicheskoĭ Fiziki, Vol. 29, No. 5, 2003, pp. 15–19.

Fractal Vortex Structure in a Superconductor Lattice Model

S. A. Ktitorov

Ioffe Physicotechnical Institute, Russian Academy of Sciences, St. Petersburg, 194021 Russia
St. Petersburg State Electrotechnical University, St. Petersburg, 197376 Russia
e-mail: ktitorov@mail.ioffe.ru

Received October 10, 2002

Abstract—The vortex structure is considered within the framework of a superconductor lattice model with a kinetic term of the Harper type. The problem is reduced to the analysis of discrete maps typical of the theory of fractal structures. *© 2003 MAIK "Nauka/Interperiodica".*

Introduction. Previously [1–3], it was reported that discreteness of the group of magnetic translations in a superconductor significantly influences the nature of the ground state and the thermodynamic properties of high-T_c superconductors in the vicinity of the upper critical magnetic field strength. Besides the thermodynamic properties and the critical behavior in a magnetic field, it was also of interest to describe the vortex structure in the case when the characteristic distance between vortices is comparable with the crystal lattice parameter. An attempt undertaken in [4] employed the approach based on a small parameter representing the ratio of the lattice constant a to the magnetic length

$$l_H = \sqrt{\frac{\hbar c}{2eH}}$$

or an equivalent quantity $\beta = \Phi/\Phi_0$, where $\Phi = Ha^2$ is the magnetic flux through a crystal lattice plaquette and

$$\Phi_0 = \frac{2\pi\hbar c}{2e}$$

is the London flux quantum. The presence of a small parameter led to a qualitatively weak dependence of the free energy on the vortex structure configuration.

The same problem can be considered using an alternative approach not employing the above parameter. The consideration can be conducted within the framework of the self-consistent field approximation with neglect of the vortex mixing, which allows the problem to be reduced to a two-dimensional (2D) case. The free energy functional can be written as

$$F = \sum_{n,n';\,m,m'} J_{nm;\,n',m'} \exp\left[i\frac{2e}{\hbar c}\int d\mathbf{l}\cdot\mathbf{A}\right]\bar{\phi}_{n'm'}\phi_{nm} + \sum_{nm}[\tau\bar{\phi}_{nm}\phi_{nm} + g(\bar{\phi}_{nm}\phi_{nm})^2], \quad (1)$$

where J is the tunneling integral; $x = ma$ and $y = na$ are the coordinates of the 2D lattice sites; $\bar{\phi}_{nm}$ is the complex-conjugate order parameter; $\mathbf{A}$ is the vector potential; and $\tau = \alpha(T - T_c)/T_c$. In Eq. (1), integration in the exponent is performed along a straight segment connecting lattice sites with the coordinates nm and $n'm'$.

Differentiating Eq. (1) with respect to $\bar{\phi}_{nm}$, we obtain the Ginzburg–Landau lattice (GLL) equation for a superconductor in a strong magnetic field:

$$\sum_{n'm'} J_{nm,\,n',m'} \exp\left[i\frac{2e}{\hbar c}\int d\mathbf{l}\cdot\mathbf{A}\right]\phi_{n'm'} + \tau\phi_{nm} + g|\phi_{nm}|^2\phi_{nm} = 0. \quad (2)$$

Choosing the Landau gauge $\mathbf{A} = \mathbf{e}_y Hx$ and considering the case of a simple square lattice with an electron spectrum in the tight binding approximation (whereby J is the tunneling integral between nearest neighbors), Eq. (2) can be rewritten as follows:

$$J\{\phi_{m+1,n} + \phi_{m-1,n}\} + J\{\phi_{m,n+1}\exp[-i2\pi\beta m] + \phi_{m,n-1}\exp[i2\pi\beta m]\} + \tau\phi_{nm} + g|\phi_{nm}|^2\phi_{nm} = 0. \quad (3)$$

This equation can be converted to a simpler form. First, note that, since Eq. (3) is nonlinear, a Fourier transform offers little help, because the nonlinear term would become integral. However, taking into account the special form of the nonlinear term in the GLL equation, it is possible to make a substitution usually employed in studying the linear Harper equation [5]:

$$\phi_{mn} = u_m \exp(i\kappa m). \quad (4)$$

1063-7850/03/2903-0181$24.00

As a result of this substitution, Eq. (3) acquires the form

$$u_{m+1} + u_{m-1} + 2\cos(2\pi m\beta - \kappa)u_m + \tau u_m + g|u_m|^2 u_m = 0, \quad (5)$$

which can be called the nonlinear Harper equation or the Harper–Ginzburg–Landau equation. Below, we will consider some implications of this equation.

Analysis of the nonlinear Harper equation. Relation (5) is very interesting. This equation implies two mechanisms accounting for quasiperiodic solutions, each being capable of forming a rather irregular structure possessing self-similar and fractal properties. Acting in accordance with the notions about the Abrikosov vortex lattice, we can first linearize Eq. (5) assuming the order parameter amplitude to be small in the vicinity of the H_{c2} line. This yields an equation,

$$u_{m+1} + u_{m-1} + 2\cos(2\pi m\beta - \kappa)u_m + \tau u_m = 0, \quad (6)$$

which differs from the linear Harper equation [5] in the same manner as the Ginzburg–Landau equation for a superconductor in a magnetic field differs from the Schrödinger equation for a charged particle in a magnetic field. Therefore, the H_{c2} line is determined by the condition $\tau = \epsilon_1$, where ϵ_1 is the lower edge of the Harper multiband spectrum. When the quantity β in Eq. (6) is rational, there is a dimensional crossover effect [1] near the lower subband. In this limit, the vortex structure exhibits complete pinning on the lattice. Further decrease in the temperature or the magnetic field strength (i.e., an increase in the absolute value of τ) leads to the appearance of fractal structures.

As is known, the Harper operator spectrum corresponding to an irrational β forms a Cantor set and, hence, no dimensional crossover effect takes place. Here, we will restrict the consideration to a qualitative analysis of the case when the order parameter amplitude is small and the parameter β can be well approximated by finite continued fractions. The scale-invariant properties of the linearized Harper equation were studied by the renormalization group method in [6, 7], while the exact approach using the Bethe ansatz can be found in [8]. The multifractal properties of eigenfunctions and eigenvalues of the Harper operator were studied numerically and using the Bethe ansatz in [9]. Interesting results were also obtained in [10].

Unfortunately, the exact method based on the Bethe ansatz is still not generalized to the nonlinear case, and so this possibility cannot be excluded. The interested reader can find further details in the papers cited above. Here, it should only be noted that a solution to the linearized Harper equation has the form of a chaotic distribution of localized functions of the Wannier type that can be naturally treated as the precursors of the superconducting state. The amplitude of the order parameter can be determined using perturbation theory. Some other approaches are also noteworthy. In particular, Eq. (5) can be written in the form of a nonlinear 2D map in the field of complex numbers:

$$\begin{pmatrix} u_{m+1} \\ u_m \end{pmatrix} = \begin{pmatrix} -\tau - g|u_m|^2 - 2\cos(2\pi m\beta - \kappa) & -1 \\ 1 & 0 \end{pmatrix} \begin{pmatrix} u_m \\ u_{m-1} \end{pmatrix}. \quad (7)$$

Conclusions. The main conclusion from the above analysis is that the fractal vortex structure is determined by 2D maps of complex numbers numerated by real numbers (the 2D character is not related to the space dimension). This implies that, similar to the Abrikosov lattice, the 2D vortex structure in the lattice model is determined by the distribution of superconducting precursors along the real axis. In contrast to the continuum approximation, this distribution in the general case is not periodic. As a first approximation in β, the order parameter distribution can be written as

$$\phi(x, y) = C\exp\left(-\frac{x^2 + y^2}{2l_H^2}\right) \times \sum_{n=-\infty}^{\infty} \exp\left[-\pi(n + u_n)^2 + \frac{\sqrt{2\pi}i(x + iy)}{l_H}(n + u_n)\right], \quad (8)$$

where the quantities u_n are determined by an appropriate discrete map taking into account the fractal effects. Note that, for $u_m = 0$, the sum in Eq. (8) converts into the elliptic theta-function. Therefore, distribution (8) can be considered as a natural generalization to special number fields, by analogy with introduction of the basis functions and the functions on *p*-adic number fields. In addition to the aforementioned maps, this can be, for example, a standard Chirikov map, which is equivalent to the Frenkel–Contorova model:

$$\begin{cases} I_{n+1} = I_n - \dfrac{2\pi V_0}{\lambda b}\sin(2\pi y_n/b) \\ y_{n+1} = y_n + a + I_{n+1}. \end{cases} \quad (9)$$

In the case when the interaction of vortices is taken into account, distribution (8) can be described by a generalized standard map of the type

$$\begin{cases} I_{n+1} = I_n - \dfrac{2\pi V_0}{\lambda b}\sin(2\pi y_n/b) \\ y_{n+1} = y_n + a - \dfrac{1}{\beta}\ln(1 - \beta I_{n+1}). \end{cases} \quad (10)$$

Acknowledgments. The author is grateful to Yu.I. Kuz'min, E.K.Kudinov, and B.N. Shalaev for fruitful discussions.

This study was supported by the Russian Foundation for Basic Research, project no. 02-02-17667.

REFERENCES

1. S. A. Ktitorov, B. N. Shalaev, and L. Jastrabik, Phys. Rev. B **49**, 15248 (1994).
2. S. A. Ktitorov, Yu. V. Petrov, B. N. Shalaev, and V. S. Sherstinov, Int. J. Mod. Phys. B **6**, 1209 (1992).
3. S. A. Ktitorov and B. N. Shalaev, Fiz. Tverd. Tela (St. Petersburg) **37**, 177 (1995) [Phys. Solid State **37**, 94 (1995)].
4. E. S. Babaev and S. A. Ktitorov, Fiz. Tverd. Tela (St. Petersburg) **39**, 1158 (1997) [Phys. Solid State **39**, 1024 (1997)].
5. D. R. Hofstadter, Phys. Rev. B **14**, 2239 (1976).
6. I. M. Suslov, Zh. Éksp. Teor. Fiz. **83**, 1079 (1982) [Sov. Phys. JETP **56**, 612 (1982)].
7. M. Wilkinson, J. Phys. A **20**, 4337 (1987).
8. P. B. Wiegmann and A. V. Zabrodin, Nucl. Phys. B: Field Theory Stat. Syst. **422**, 495 (1994).
9. A. G. Abanov, J. C. Tolstra, and P. B. Wiegmann, cond-mat/9711274.
10. Shao-shiung Liu and Shi-shyr Roan, cond-mat/9912473.

Translated by P. Pozdeev

Technical Physics Letters, Vol. 29, No. 3, 2003, pp. 184–187. Translated from Pis'ma v Zhurnal Tekhnicheskoĭ Fiziki, Vol. 29, No. 5, 2003, pp. 20–29.

Nonlinearity of a Ferroelectric Layer Described Using a Planar Capacitor Model

O. G. Vendik and M. A. Nikol'skiĭ

St. Petersburg State Electrotechnical University, St. Petersburg, 197376 Russia

e-mail: OGVendik@mail.eltech.ru

Received September 18, 2002

Abstract—A method for calculating the capacitance–voltage (*C–U*) characteristic of a planar ferroelectric film capacitor with allowance for the material nonlinearity is proposed. The nonlinear properties of the ferroelectric material are described in terms of the Ginzburg–Devonshir equation under the conditions of minimum free energy of the planar capacitor. An analysis of the results shows that the capacitance of a planar ferroelectric film capacitor can be calculated using the proposed elementary model with a relative error not exceeding 2%. © *2003 MAIK "Nauka/Interperiodica"*.

Formulation of the problem. Presently, there is an urgent need for the numerical calculation of planar microwave devices with allowance for the properties of ferroelectric materials. This is related to extensive research aimed at the implementation of ferroelectrics in microwave integrations, for example, as thin (~1 μm thick) films on dielectric substrates [1, 2].

Thin ferroelectric films are conventionally studied using planar model capacitor structures (Fig. 1), which are simple in both design and calculation. In idealized cases (Fig. 2a), the capacitor gap is provided with conditional electric walls, whereby the field in the gap can be considered as homogeneous. The capacitance of such a structure can be calculated using the simple formula

$$C(E) = \varepsilon_0\varepsilon_f(E)\frac{wh_f}{s}, \quad (1)$$

where ε_0 is the permittivity of vacuum; $\varepsilon_f(E)$ is the permittivity of the ferroelectric material (described, e.g., using a phenomenological model developed in [3, 4]); *s* and *w* are the capacitor gap width and length, respectively; and h_f is the ferroelectric film thickness. The electric field strength is related to the voltage *U* applied between the capacitor electrodes as

$$E = \frac{U}{s}. \quad (2)$$

Owing to the field homogeneity in the model adopted, the nonlinearity of the capacitance $C(E)$ follows the nonlinearity of the permittivity function $\varepsilon_f(E)$. In a real planar capacitor, the electric field distribution is inhomogeneous. The existing calculation methods allow this problem to be solved only in a linear medium [5, 6], since the numerical solution of a nonlinear inhomogeneous problem is very cumbersome. One approach is offered by the method of partial capacitances [6] based on the conformal (angle-preserving) mapping (APM), which allows the field in a planar structure to be transformed into the field of a planar capacitor with homogeneous filling [6]. The capacitance of a planar capacitor formed by the ferroelectric film and the conducting electrodes is conventionally calculated by the following formula derived within the framework of the APM approach:

$$C_f(E) = \frac{w\varepsilon_0\varepsilon_f(E)}{s/h_f + (4/\pi)\ln 2}. \quad (3)$$

Figure 2b shows a qualitative schematic diagram of the field lines in a planar capacitor calculated using the APM method.

Since the APM approach is based on the solution of the Laplace equation for a linear dielectric, nonlinear properties of the ferroelectric material cannot be taken into consideration. Recalculation of the field strength entering in Eq. (3) to the permittivity $\varepsilon_f(E)$, which is conventionally performed using relation (2), is unjustified and can lead to significant errors. Thus, there is a

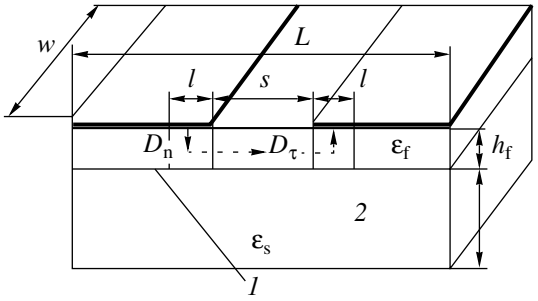

Fig. 1. Schematic diagram of a planar film capacitor showing an average electric field line in a nonlinear approximation: (*1*) magnetic wall; (*2*) substrate.

need to find a simple but correct method for calculating capacitance–voltage characteristic of a planar ferroelectric film capacitor with allowance for the nonlinearity of the ferroelectric material.

Method of calculation. Let us use a model conditionally describing the shape of the field lines. Assume that the "electric walls" at the gap edges (depicted in Fig. 2a) are absent. Then, an average field line, depicted by the dashed curve in Fig. 1, goes beyond the gap edges. This line is characterized by the tangential (D_τ) and normal (D_n) components of the electric induction D:

$$D_n = \frac{Q}{wl}, \quad D_\tau = \frac{Q}{wh_f}, \tag{4}$$

where Q is the charge and l is a parameter (with the dimension of length) taking into account the charge spreading beyond the gap in the near-electrode region.

The nonlinear dielectric response of a ferroelectric material can be described in terms of the Ginzburg–Devonshir equation [7, 8]

$$\varepsilon_0 E = \frac{1}{\varepsilon_f} D + \frac{D^3}{D_N^2}, \tag{5}$$

where $D_N = \varepsilon_0(3\varepsilon_{00})^{1.5}0.5E_N$, ε_{00} is the phenomenological parameter [3, 4] related to the Curie–Weiss constant of the ferroelectric material, and E_N is the normalization electric field value [3, 4].

Assuming the electric field in the planar capacitor to be homogeneous along the selected directions (D_τ and D_n) and using formulas (4) and (5), we obtain an expression for the potential difference between electrodes:

$$U(Q) = \frac{1}{\varepsilon_0 w}\left\{\left[\frac{1}{\varepsilon_f}\frac{Q}{h_f} + \frac{Q^3}{h_f^3 w^2 D_N^2}\right](s+l) + 2\left[\frac{1}{\varepsilon_f}\frac{Q}{l} + \frac{Q^3}{l^3 w^2 D_N^2}\right]kh_f\right\}, \tag{6}$$

where k is a parameter taking into account how deep the electric field lines penetrate into the ferroelectric film. Introducing the notations $p = s/h_f$, $x = l/h_f$ (this parameter determines the field line shape in the near-electrode regions of the planar capacitor), $A = \varepsilon_f^{0.5}/h_f w D_N$, and $q = QA$, we can write expression (6) as follows:

$$U(q) = \frac{1}{A\varepsilon_0\varepsilon_f w}\left[\left(p + x + \frac{2k}{x}\right)q + \left(p + x + \frac{2k}{x^3}\right)q^3\right]. \tag{7}$$

The free energy W of a planar capacitor can be expressed as [9]

$$W(Q) = \int_0^Q U(Q)dQ.$$

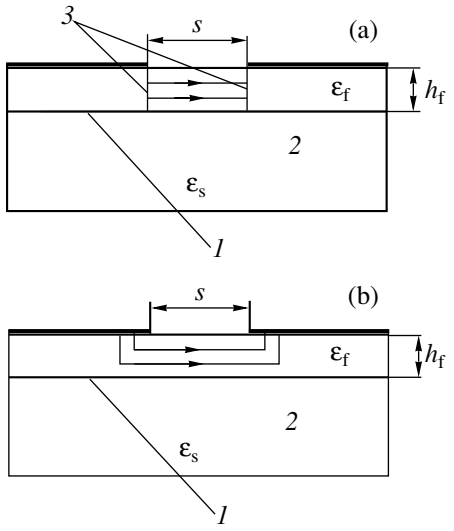

Fig. 2. Schematic diagrams of a planar film capacitor showing electric field lines according to (a) the ideal capacitor model and (b) the APM method: (*1*) magnetic wall; (*2*) substrate; (*3*) electric walls.

Upon substituting expression (7) and integrating, we obtain

$$W(q) = \frac{1}{A^2\varepsilon_0\varepsilon_f w}\left[\frac{1}{2}\left(p + x + \frac{2k}{x}\right)q^2 + \frac{1}{4}\left(p + x + \frac{2k}{x^3}\right)q^4\right]. \tag{8}$$

In the linear case ($q \ll 1$), Eqs. (7) and (8) can be written as

$$U(Q) = \frac{Q}{\varepsilon_0\varepsilon_f w}\left(p + x_0 + \frac{2k}{x_0}\right), \tag{9}$$

$$W(Q) = \frac{Q^2}{2\varepsilon_0\varepsilon_f w}\left(p + x_0 + \frac{2k}{x_0}\right), \tag{10}$$

where x_0 is independent of the capacitor charge. In this approximation, the capacitance $C_f(Q) = Q/U(Q)$ can be determined using expression (9) as

$$C_f = \varepsilon_0\varepsilon_f w\left(p + x_0 + \frac{2k}{x_0}\right)^{-1}. \tag{11}$$

Now we can determine x_0 using the condition that the free energy of the planar capacitor (10) must be at the minimum [9], $dW/dx_0 = 0$, in order to render the solution stable with respect to the field line shape. In a zero approximation in the capacitor charge, this yields

$$x_0 = \sqrt{2k}. \tag{12}$$

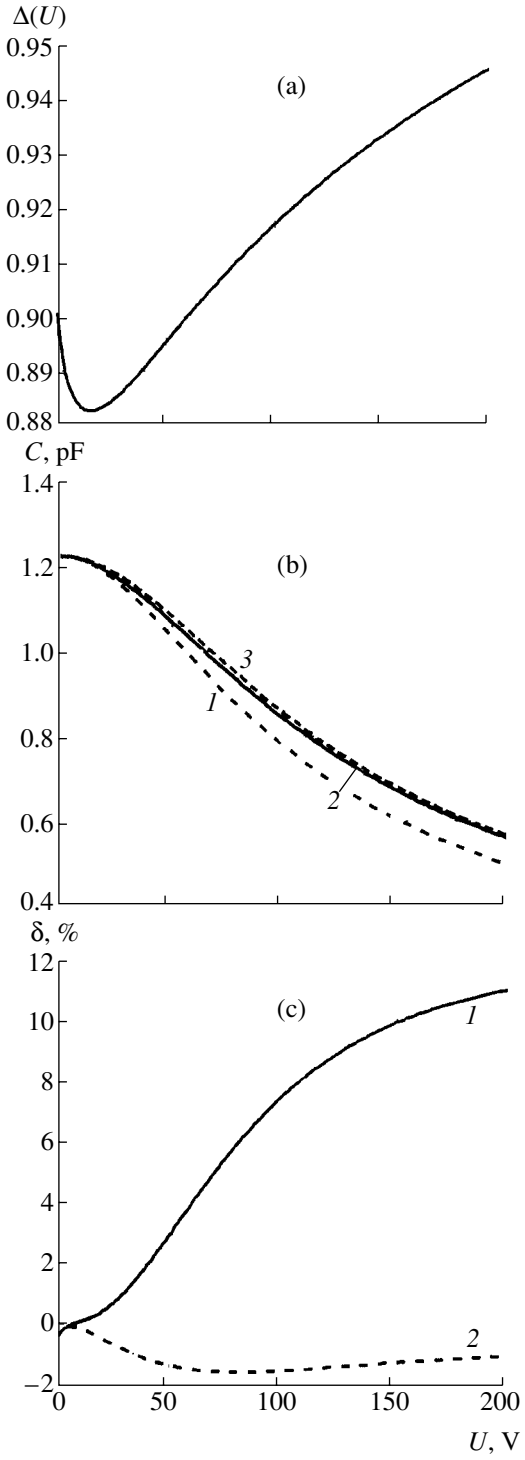

Fig. 3. Plots of (a) the $\Delta(U)$ function which determines elongation of the field line due to nonlinearity of the ferroelectric material; (b) capacitance–voltage characteristics of a planar capacitor calculated by (*1*) the traditional method [formulas (3) and (2)], (*2*) the method developed in this study [formulas (17) and (16)], and (*3*) the modified method [formulas (17) and (19)]; and (c) relative error of the capacitance calculations using expression (17) and (*1*) Eqs. (3) and (2) and (*2*) Eqs. (3) and (19). The model capacitor dimensions used in the calculation were $s = 5$ μm, $w = 0.6$ mm, $h_f = 1$ μm. The ferroelectric film parameters are listed in the table.

Substituting this expression into formula (11), we obtain

$$C_f = \varepsilon_0\varepsilon_f w\left(\frac{s}{h_f} + 2\sqrt{2k}\right)^{-1}. \quad (13)$$

A comparison of this expression to formula (3) derived within the framework of the APM approach gives the following expression for the parameter k:

$$k = \frac{1}{2}\left(\frac{2}{\pi}\ln 2\right)^2. \quad (14)$$

Now let us proceed to the nonlinear case, whereby $q \geq 1$. Differentiating Eqs. (8) with respect to the parameter x and using the condition of minimum free energy of the planar capacitor, we obtain a biquadratic equation for the unknown value of x corresponding to this minimum in the nonlinear approximation:

$$x^4 - \frac{4}{3}kx^2 - 2kq^2 = 0.$$

Rejecting the solutions deprived of physical sense, we arrive at an expression for x_1 as a function of the capacitor charge in the first approximation:

$$x_1(q) = \sqrt{\frac{2}{3}k + \sqrt{\left(\frac{2}{3}k\right)^2 + 2kq^2}}. \quad (15)$$

Using this expression, we can rewrite formula (7) for the potential difference in the following form:

$$U(q) = \frac{1}{A\varepsilon_0\varepsilon_f w}\left[\left(p + x_1(q) + \frac{2k}{x_1(q)}\right)q + \left(p + x_1(q) + \frac{2k}{x_1^3(q)}\right)q^3\right]. \quad (16)$$

Using this expression, the dynamic capacitance of a planar capacitor can be determined from the relation

$$\frac{1}{C_{dyn}(Q)} = \frac{dU}{dQ}. \quad (17)$$

Results and discussion. Thus, by minimizing the free energy of a planar capacitor and using the Ginzburg–Devonshir equation, it is possible to take into account the nonlinearity of the ferroelectric material used in this capacitor. According to formula (7), an average length L of the field line can be represented as (see Fig. 1)

$$L = s + h_f\Delta(U), \quad (18)$$

where $\Delta(U) = x_1(q) + 2k/x_1(q)$ is a function of the voltage which determines elongation of the field line due to nonlinearity of the ferroelectric material. Here, the voltage U is described by expression (16) as a function of the capacitor charge q.

Figure 3a presents a plot of the $\Delta(U)$ function. As can be seen, this function tends to unity. For most

Typical parameters of a $Ba_{0.5}Sr_{0.5}TiO_3$ ferroelectric film calculated using the proposed model [3, 4]

ε_f (0)	ε_f (200 V)	ξ_S	T_F, K	T_c, K	D_N, C/m^2
1390	210	1	175	238	4.71

capacitor geometries, the average $\Delta(U)$ value is on the order of 0.9, so that we can put in the calculation (not losing precision) that $\Delta(U) = 1$. According to our estimates, the field strength in the capacitor is described by the formula

$$E = \frac{U}{s + h_f}. \quad (19)$$

Obviously, the shape of the average electric field line (Fig. 1) was selected rather arbitrarily. However, the free energy minimum determined as described above justifies the statement that the obtained solution is stable with respect to small deformations of the average field line. Therefore, the field line shape adopted is close to the true one and, hence, the above solution to the problem of description of a nonlinear planar capacitor with a ferroelectric film is reliable.

Figure 3b shows three curves describing the dependence of the capacitance of a planar capacitor (Fig. 1) on the applied voltage. One capacitance–voltage characteristic (curve *2*) was calculated by formula (17) derived using the method developed above, in which the nonlinearity of the ferroelectric film was described using the Ginzburg–Devonshir equation and the condition of minimum free energy of the capacitor, with the applied voltage calculated using formula (16) for a given charge q. Another dependence (curve *1*) was calculated using a traditional approach according to which the capacitance was determined by formula (3), derived within the framework of the APM method, and the field strength was related to the applied voltage by formula (2). And the third plot (curve *3*) was calculated using a modified approach, whereby the capacitance was still determined by formula (3) according to the APM method, while the field strength was converted into the applied voltage using formula (19).

The discrepancy between the results of calculations using formulas (17) and (3) was within 10–12% in the case of relation (2) and decreased to 2% in the case of relation (19) (Fig. 3c). Expression (19) has proved to be correct for most planar capacitor geometries encountered in practice (s = 5–30 μm, h_f = 0.5–1 μm, w = 0.1–2 mm).

Thus, the relative error of taking into account the nonlinearity of a ferroelectric material can be reduced to 2% when the capacitance of a planar ferroelectric film capacitor is calculated using the APM method and assuming that the electric field strength and applied voltage are related by formula (19), which is equivalent to the electric field lines being longer by a value on the order of h_f. Therefore, by using formula (19) in calculations of the capacitance–voltage characteristics of a planar ferroelectric film capacitor according to the APM approach, it is possible to take into account the nonlinear properties of the ferroelectric material with greater precision as compared to the existing methods.

REFERENCES

1. C. Krowne, M. Daniel, S. Kirchoefer, *et al.*, IEEE Trans. Microwave Theory Tech. **MTT-50** (2), 537 (2002).
2. O. Vendik, I. Vendik, N. Setter, *et al.*, Microwave Wireless Comp. Lett. **11** (10), 407 (2001).
3. O. G. Vendik and S. P. Zubko, J. Appl. Phys. **82** (9), 4475 (1997).
4. O. G. Vendik and S. P. Zubko, J. Appl. Phys. **88** (9), 5343 (2000).
5. A. N. Deleniv, Zh. Tekh. Fiz. **69** (4), 8 (1999) [Tech. Phys. **44**, 356 (1999)].
6. O. G. Vendik, S. P. Zubko, and M. A. Nikol'skiĭ, Zh. Tekh. Fiz. **69** (4), 1 (1999) [Tech. Phys. **44**, 349 (1999)].
7. V. L. Ginzburg, Usp. Fiz. Nauk **38** (4), 490 (1949).
8. A. F. Devonshir, Philos. Mag. **40**, 1040 (1949) [Part 1]; Philos. Mag. **42**, 1065 (1951) [Part II].
9. L. D. Landau and E. M. Lifshitz, *Electrodynamics of Continuous Media* (Nauka, Moscow, 1957; Pergamon Press, Oxford, 1960).

Translated by P. Pozdeev

Technical Physics Letters, Vol. 29, No. 3, 2003, pp. 188–190. Translated from Pis'ma v Zhurnal Tekhnicheskoĭ Fiziki, Vol. 29, No. 5, 2003, pp. 30–35.

Hydrodynamic Aspects of the Channel Formation by a CO_2 Laser Beam Penetrating Deep into a Liquid

V. S. Golubev and F. Kh. Mirzoev*

Institute for Problems of Laser and Information Technologies, Russian Academy of Sciences, Shatura, Russia

** e-mail: mirzo@lazer.nictl.msk.su*

Received September 9, 2002

Abstract—It is shown that, taking into account the hydrodynamic phenomena accompanying the development and maintenance of a deep laser-induced vapor-gas channel in a liquid, it is possible to estimate the order of magnitude of the channel depth and growth rate, as well as the characteristic frequencies of the channel wall instabilities and acoustic perturbations. The estimates agree with the experimental data. © *2003 MAIK "Nauka/Interperiodica".*

Investigation of the process of formation and stability of a deep vapor-gas channel produced by a focused laser beam penetrating into a liquid medium is of considerable importance from the standpoint of both basic physics and practical applications of lasers [1, 2]. During laser processing (e.g., cutting) of materials, the process efficiency and the product quality can be increased by coating the material with a layer of liquid (water, oil, etc.), which improves the local heat removal conditions. Investigations of the underwater laser welding are of considerable interest for building ships and sea structures (oil and gas pipelines, offshore platforms, floating aerodromes, etc.).

In recent years, considerable progress has been achieved in the application of high-intensity laser beams for the processing of heterogeneous materials (e.g., composites) [3] and for the surgery of sanguiferous organs, in particular, for the laser transmyocardial revascularization (LTMR) treatment [4]. During the LTMR process, a long laser pulse must make a channel in a cardiac muscle and reach the blood-filled left ventricular cavity, while not penetrating deep into this cavity. Investigation of the process of laser channel formation in the blood is important for developing methods to prevent bubble and solid particle formation in the blood and to provide for the on-line diagnosis aimed at the identification of biological tissues perforated by the laser beam. Such diagnostic facilities are being developed based on the phenomena of acoustic emission [5] and the Doppler scattering of laser radiation from the fragments of biological tissues ejected from the channel with a vapor flow [6].

Experimental observations of the vapor-gas channel formation in liquids (mostly in water) penetrated by focused beams of CO_2 lasers operated at an output power from 50 W to 5 kW were reported in [4–8]. It was shown that the laser channel depth in water increases with the laser power to reach 1–5 cm at 1–5 kW. In a viscous liquid (e.g., glycerol), the channel depth is several times greater [7, 8] and the channel walls exhibit a significantly higher stability as compared to the case of water. The growth and maintenance of a vapor-gas channel in water are accompanied by the development of various instabilities manifested by "corrugation" of the channel walls [2, 4], the formation and collapse of microvoids (10–10^2 μm), and acoustic wave emission into the surrounding medium and atmosphere. The spectrum of acoustic frequencies ranges up to 1.5 kHz [5] or even extends to 10–15 kHz, at an acoustic pressure amplitude of up to 0.1 MPa [4]. The channel growth rate in the initial stage, after switching on a laser beam with an intensity of 10^5 W/cm^2, amounted to ~5 m/s and decreased down to ≤1 m/s after a time period of ~10^{-2} s [4]. Cybulski and Mucha [8] measured the velocity field of a convective closed (vortex) water flow in the vicinity of a laser-induced vapor-gas channel. The size of the flow field was on the same order as the vapor-gas channel depth, and the convection velocity reached up to 10 cm/s, which corresponded to a turbulent character of the flow.

The purpose of this study was to develop a consistent qualitative model of vapor-gas channel formation in a liquid with allowance for the turbulent hydrodynamic flows arising in the bulk and, accordingly, for the turbulent convective thermal conductivity in the liquid (determining the energy balance in the vapor-gas channel, the quasistationary channel depth, and the channel propagation velocity in the growth stage after switching on the laser).

The well-known relation for determining the vapor-gas channel depth h as a function of the laser beam power P, which takes into account the molecular (laminar) thermal conductivity in the heat removal from the laser-induced channel, leads to very high values of h. For example, the h/P ratio in water exceeds 10^3 cm/kW,

which is three orders of magnitude higher than the experimental vales [4, 7, 8].

We obtained qualitative estimates for the h value, the mean flow velocity, and the turbulent convection in a low-viscosity liquid (i.e., in water), which correspond to the case of intense heat removal from the vapor-gas channel (Fig. 1). The balance equations for the energy, momentum, and mass were based on the Kolmogorov model for a homogeneous isotropic turbulence [9]. The maximum (external) size of the turbulence was assumed to be equal to the channel depth h, while the minimum (internal) size Λ_i is on the order of $\Lambda_i \approx h(Re/Ri)^{-3/4}$, where $Re = v_m h/\nu$, $Ri = 2 \times 10^2$ is the critical Reynolds number with respect to the internal size, v_m is the mean liquid flow velocity in the outer region, and ν is the liquid viscosity. The convection is caused either by the thermal expansion of liquid leading to its buoyancy (Archimedean convection) or by the thermocapillary force (Marangoni effect). In the case of vapor-gas channel formation in water, the Archimedean convection according to our estimates must prevail at a power of $P > 10^2$ W. The turbulent thermal diffusivity was assumed (in accordance with the concept of homogeneous isotropic Kolmogorov turbulence [9]) to be on the order of $\varepsilon v_m h$, where ε is the intensity of the turbulence (~10^{-3}–10^{-2} [10]). The velocity of convention is determined by the balance of forces, including the driving force (Archimedean buoyancy or the thermocapillary drag of the surface layer) and the retarding force (turbulent viscosity). The kinematic viscosity was also assumed to be $\varepsilon v_m h$ (for a liquid with the Prandtl number of the order of Pr ~ 1).

The equation of the energy balance for the vapor-gas channel was used in the standard form [1], but with the turbulent diffusion coefficient $\chi_\tau \cong \chi Ri \cong 0.5$ cm^2/s. This choice is justified by the fact that $\Lambda_i < r_0$ (mean vapor-gas channel radius). The final formula describing vapor-gas channel depth as a function of the Laser power is as follows:

$$h = \frac{P}{2\pi\chi Ri\rho C(T_B - T_0)},$$

where T_0 is the initial temperature, T_B is the boiling temperature, ρ is the density, and C is the heat capacity of the liquid. For water: $\rho C(T_B - T_0) \cong 3 \times 10^2$ J/cm^3 and $\chi = 3 \times 10^{-3}$ cm^2/s, which yields an estimate of $h/P \cong 1$ cm/kW in satisfactory agreement with experimental observations [8] (Fig. 2).

We have also estimated the velocity v_z of the vapor-gas channel growth after switching on the laser beam in the initial stage ($h > r_0$). The estimate was obtained assuming a convective turbulent thermal flux from the bottom of the vapor-gas channel streamlined with a liquid flow arising as a result of the liquid particles being pushed apart by the vapor-gas channel incorporating at a velocity of v_z. In the case of a vapor-gas channel growing in water, we obtained an estimate of $v_z \approx 10^{-2}\bar{q}$, where $\bar{q}$ is the laser beam intensity on the axis, reduced to a specific energy per liquid volume at $T = T_B$: $\bar{q} = \bar{q}/\rho C T_B$. Jansen *et al.* [4] experimentally measured the vapor-gas channel velocity at $\bar{q} \cong 10^5$ cm/s to obtain $v_z \cong 6 \times 10^2$ cm/s (in the initial stage of the channel growth). According to our formula, $v_z \cong 10^3$ cm^3/s.

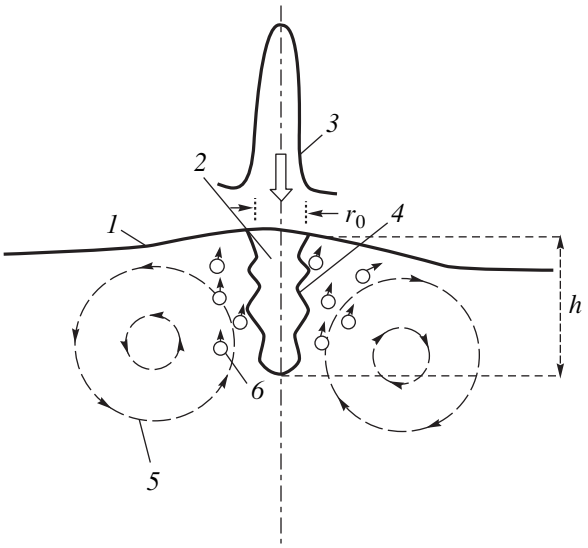

Fig. 1. A schematic diagram illustrating the geometry of a quasistationary vapor-gas channel formed and maintained by a focused laser pulse: (*1*) liquid surface; (*2*) vapor-gas channel; (*3*) laser beam intensity profile; (*4*) corrugation; (*5*) vortex convection liquid flow; (*6*) bubbles. See the text for explanations.

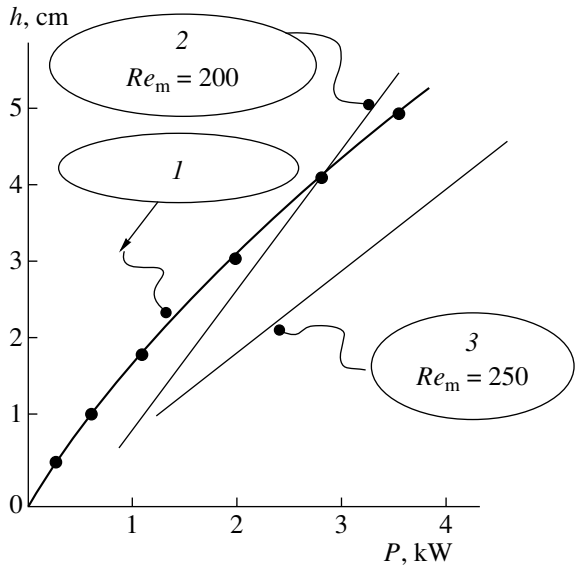

Fig. 2. Plots of the vapor-gas channel depth h in water versus the laser beam power P: (*1*) experiment; (*2*) model $Re_m = 200$; (*3*) model $Re_m = 250$.

The strong instability of the vapor-gas channel wall in a low-viscosity liquid is caused by periodically repeated capillary collapse, whereby the cylindrical liquid walls become corrugated with a spatial period of $\sim r_0$ along the vapor-gas channel axis, and a corrugation development time of $\tau_g \approx (\sigma/\rho r_0^3)^{-1/2}$, where σ is the surface tension (in water, $\tau_g \cong 0.3 r_0^{3/2} \sim (2\text{–}5) \times 10^{-3}$ s). The periodic necks, formed in the vapor-gas channel as a result of the corrugation (capillary) collapse and having a longitudinal size $\Delta z \approx r_0$ (along the channel axis), are again penetrated by the laser beam over a time period of $\tau_q \approx \Delta z/v_z \cong (0.3\text{–}3) \times 10^{-4}$ s. The "breakdown" generates vapor pressure pulses with a repetition frequency of $\Omega \sim \tau_g^{-1} \sim 10^2\text{–}10^3$ s^{-1} and a duration of $\sim\tau_q$. Ejected from the vapor-gas channel into atmosphere, these vapor pressure pulses are capable of generating acoustic perturbations with a frequency spectrum extended from 10^2–10^3 to 3×10^3–3×10^4 s^{-1}. An analogous spectral pattern in the acoustic frequency range was experimentally observed in [5, 8].

Thus, by taking into account the hydrodynamic phenomena (turbulent, thermocapillary, and buoyancy convection; capillary collapse of the corrugated channel walls periodically penetrated by the laser beam) accompanying the development and maintenance of a laser-induced vapor-gas channel in a liquid, it is possible to estimate the order of magnitude of the channel depth and growth rate, as well as the characteristic frequencies of the channel wall instabilities and acoustic perturbations. The estimates agree with the experimental data on the laser-induced channel formation in water.

Acknowledgments. This study was supported by the Russian Foundation for Basic Research, project no. 02-02-16001.

REFERENCES

1. A. A. Vedenev and G. G. Gladush, *Physical Principles of the Laser Processing of Materials* (Énergoatomizdat, Moscow, 1985).
2. V. S. Golubev, Preprint No. 83 (Institute for Problems of Laser and Information Technologies, Moscow, 1999).
3. I. N. Shiganov, Doctoral Dissertation (Moscow State Technical University, Moscow, 1999).
4. E. D. Jansen, M. Frenz, K. Kadipasaoglu, *et al.*, Optoelectron. Rep., No. 8, 9 (1996).
5. A. P. Kubyshkin, V. V. Vasiltsov, V. Ya. Panchenko, and Ye. V. Zelenev, Proc. SPIE **4644**, 201 (2001).
6. V. M. Gordienko, V. Ya. Panchenko, V. A. Ul'yanov, and A. N. Konovalov, Kvantovaya Élektron. (Moscow) **23** (10), 869 (1996).
7. A. A. Antonov, G. I. Kozlov, V. A. Kuznetsov, and M. A. Masyukov, Kvantovaya Élektron. (Moscow) **4** (8), 1747 (1977).
8. A. Cybulski and Z. Mucha, Weld. Int. **11**, 212 (1992).
9. L. D. Landau and E. M. Lifshitz, *Course of Theoretical Physics*, Vol. 6: *Fluid Mechanics* (Nauka, Moscow, 1986; Pergamon, New York, 1987).
10. S. S. Kutateladze, *A Handbook of Heat Transfer* (Gosénergoizdat, Moscow, 1958).

Translated by P. Pozdeev

Technical Physics Letters, Vol. 29, No. 3, 2003, pp. 191–193. Translated from Pis'ma v Zhurnal Tekhnicheskoĭ Fiziki, Vol. 29, No. 5, 2003, pp. 36–42.

Temperature Dynamics in a Multicharge Ion Plasma Generated by CO_2 Laser Pulses

A. E. Stepanov, G. S. Volkov, V. I. Zaĭtsev, K. N. Makarov, Yu. A. Satov, and V. K. Rerikh

Troitsk Institute of Innovation and Thermonuclear Investigations (TRINITI), Troitsk, Russia

e-mail: stepanov@triniti.ru

Received October 15, 2002

Abstract—Time evolution of the X-ray spectrum of a lead ion plasma generated by CO_2 laser pulses with an energy of 100 J and a duration of 15 ns was measured using an X-ray polychromator with six channels covering the quantum energy range from 180 to 1850 eV. The plasma temperature was determined by comparing the results of measurements with the calculated X-ray emission spectra. The electron temperature measured well agrees with the calculated data. © *2003 MAIK "Nauka/Interperiodica".*

Multicharge ion beams find increasing use both in experimental research in fields such as nuclear physics and controlled thermonuclear synthesis and in technological applications [1–3]. One possible method for generating such beams employs lasers, whereby the ion source plasma is produced by a high-power laser beam acting upon a target. The ion composition in the laser-generated plasma is a function of the plasma temperature, density, and lifetime. In the case of a pulsed laser action, the plasma parameters exhibit a rather complicated evolution influencing the ion beam parameters.

This letter presents the results of an investigation of the temperature dynamics in a multicharge lead ion plasma generated by CO_2 laser pulses with a duration of 15 ns and an energy of 100 J [4]. An analogous problem of plasma diagnostics is encountered in investigations in the field of controlled inertial-confinement synthesis.

The experimental arrangement is schematically depicted in Fig. 1. The laser beam irradiating a lead target produced a dissipated power density of $P \simeq 3 \times 10^{13}$ W/cm^2. The spatiotemporal characteristics of emission from the laser-generated plasma were measured with an X-ray polychromator [6] implementing a Θ–2Θ scheme and X-ray mirrors as the energy-dispersive elements. The channel energy E_{ch} was controlled by changing the mirror tilt angle Θ. The six-channel polychromator covered the quantum energy range from 180 to 1850 eV. The laser was operated in two regimes, producing either smooth or modulated pulses. The laser pulses of a modulated (spike) shape were obtained through the corresponding tuning of a master generator.

The energies of the "rigid" channel tuning were selected under the condition that $E_{ch} > 1$ eV, so as to eliminate line emission as much as possible from the spectrum measured. According to the results of model calculations using GIDRA program [8], numerous emission lines appear in the spectrum at lower energies. The calculation was performed within the framework of a one-dimensional model of a lead target, with laser parameters typical of the setup employed ($P_0 = 3 \times 10^{13}$ W/cm^2). The calculation model involved a simplified scheme (scaled hydrogenlike model) of the energy levels of lead ions and elementary processes determining the level population kinetics. Obviously, this model is very simple as compared to a real structure of levels. Unfortunately, a more realistic atomic model can hardly be included into gasdynamic calculations. We believe that even simplified modeling provides a certain justification of the selection of energies for tuning the polychromator channels.

In the ideal case, the E_{ch} values of all polychromator channels must correspond to a continuum "tail" of the X-ray spectrum. In our case, the tuning energy was limited from above by $E_{ch} \simeq 1850$ eV. Four channels were

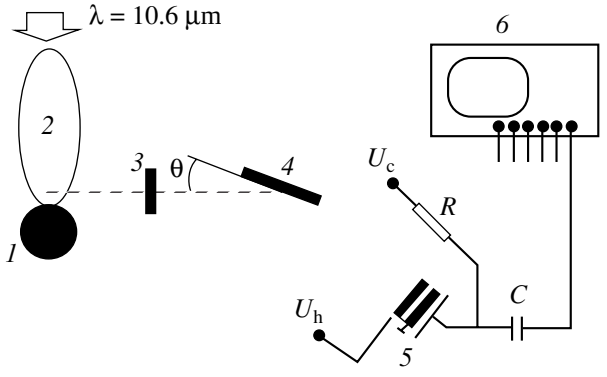

Fig. 1. Schematic diagram of the experimental arrangement with an X-ray polychromator: (*1*) lead target; (*2*) plasma torch; (*3*) X-ray filter; (*4*) multilayer mirror; (*5*) microchannel plate–collector; (*6*) oscillograph.

1063-7850/03/2903-0191$24.00 © 2003 MAIK "Nauka/Interperiodica"

Characteristics of the X-ray polychromator channels

Channel	Number	E_{ch}, eV	Mirror reflection coefficient	Energy band width, eV	Foil filter (thickness)
Soft		183	0.375	11.3	Ag (0.3 μm)
		525	0.106	9.2	Cu (0.3 μm)
Rigid	1	1080	0.324	19.5	Be (25 μm)
	2	1250	0.356	21.3	Be (30 μm)
	3	1486	0.447	25.3	Be (30 μm)
	4	1865	0.224	29.3	Be (30 μm)

employed in the energy range $E_{ch} > 1000$ eV. Two "soft" channels, tuned to $E_{ch} = 183$ and 525 eV, allowed the time variation of the X-ray intensity in the soft and rigid spectral regions to be compared. The parameters of all energy channels of the X-ray polychromator are listed in the table.

The results of preliminary experiments showed that the radiative energy losses from plasma are mostly due to the quanta with energies in the range from 100 to 500 eV. The source of continuous radiation in the range above 1 keV is the high-temperature plasma of a low-density corona. The low spectral density of the plasma emission in this spectral range did not allow us to use semiconductor diode detectors. Therefore, the radiation was detected using microchannel plates (MCPs) of the chevron type [6]. An advantage of these detectors is insensitivity to radiation of the CO_2 laser. The radiation was preselected using Be foils with a thickness of 25–30 μm. The low intensity of emission with a quantum energy above 1 keV did not allow us to use the traditional aluminum-coated Dacron (2.4 μm + 0.2 μm Al) or aluminum (4–7 μm) filters, since the UV radiation transmitted within narrow spectral intervals hindered discrimination of the useful signal (for $\hbar\omega > 1$ keV) even with the aid of multilayer X-ray mirrors. The absolute calibration of the MCP detectors was performed using either the AlK_α line ($E = 1486$ eV) excited by a pulsed electron beam [5] or the intrinsic laser plasma emission in the 1486 eV channel.

The required MCP sensitivity was achieved at a voltage of 1250–1400 V applied to the chevron assembly. The results of the calibration showed that a linear detection range amounted to approximately 400 mV for a radiation pulse width of 50 ns (for an MCP working area diameter of 4 mm). This allowed signals up to 800 mV to be detected in experiments with the laser excitation source operated at a pulse duration below 25 ns. The signals were recorded using a four-channel digital registrator (LeCroy) with a temporal discreteness of 2 ns. The experiments were performed using a polychromator design based on that described in [7]. The instrument allowed the measurements to be conducted in up to six channels at a detector–source distance above 50 cm and was equipped with a simple system of adjustment with respect to the source with the aid of a laser sight device. The accuracy of setting the angle of radiation incidence onto the multilayer X-ray mirror was about 4′, which is sufficient in most applications.

The method of restoring the electron temperature is based on the use of calculated X-ray intensities for the quantum energies corresponding to the polychromator channel adjustments. Use of the relative intensities eliminates the need for absolute calibration of the numerical model, which would be extremely difficult in view of the complicated plasma flow geometry and undetermined model kinetics. The X-ray intensity ratios in the region of continuum ($\hbar\omega > 1$ keV) are virtually independent of the electron density. In calculating the plasma emission spectrum, the relative populations of the ground state of lead ions (Pb^{18+}–Pb^{32+}) corresponded to the results of measurements of the energy and charge spectra of ions at a distance of 3 m from the target [1, 9].

In the course of the data processing, it was established that using the ratio of the signal intensities in channels 4 and 1 provides for a better reproducibility of the electron temperature variation as compared to the other combinations of channels. Figure 2a shows a typical time variation of the electron temperature determined from the ratio of the signal intensities in the rigid channels 4 and 1 (see table) measured with a smooth laser pulse. As can be seen, the electron temperature exhibits a rather smooth variation. The peak value amounts to 800–1000 eV, which is consistent with the calculated data [1, 9]. The situation changes when the laser pulse has a characteristic spike appearance (Fig. 2b). In this case, the temperature variation with time also exhibits a sharply pronounced peak structure, the peaks of the electron temperature and the laser radiation intensity being time-correlated.

Thus, the proposed method, which combines the emission spectrum measurements with a multichannel X-ray polychromator and data processing based on the results of model calculations, allows the time variation of the electron temperature to be studied for a lead

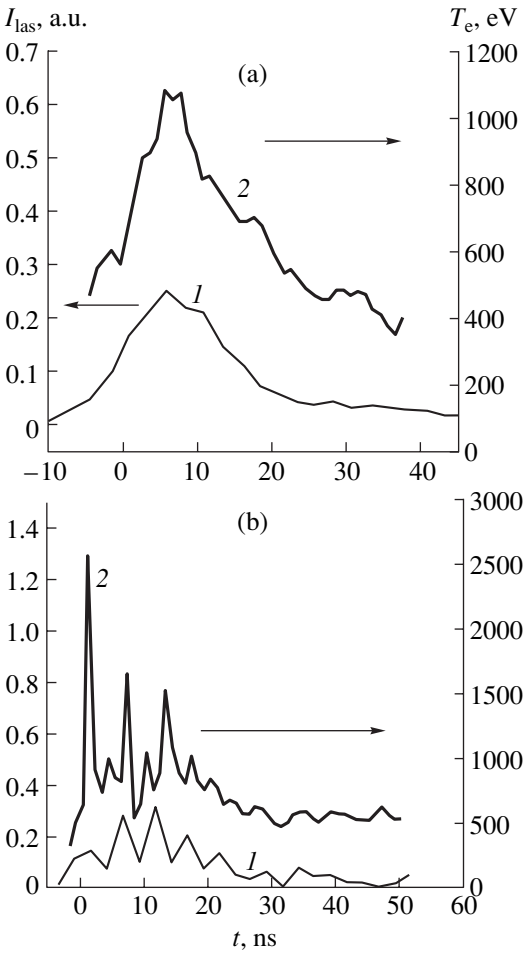

Fig. 2. Time variation of (*1*) the laser radiation intensity I_{las} and (*2*) electron temperature T_e of the plasma generated by (a) smooth and (b) modulated (spike) laser pulses.

plasma generated by a CO_2 laser operated at a moderate power. Further development of this method will consist in the X-ray quantum energy range being extended above 2000 eV and in using a more realistic kinetic model, which must provide for the obtaining of more reliable calculated emission spectra.

Acknowledgments. This study was supported by the INTAS Foundation (grant no. 2090-97) and the Russian Foundation for Basic Research (project no. 02-02-16832).

REFERENCES

1. V. Yu. Baranov, K. N. Makarov, V. C. Roerich, *et al.*, Laser Part. Beams **14**, 347 (1996).
2. P. Fournier, G. Gregoire, H. Haseroth, *et al.*, Rev. Sci. Instrum. **71** (2), 924 (2000).
3. N. V. Pleshivtsev and A. I. Bazhin, *Physics of the Ion Beam Action upon Materials* (Vuzovskaya Kniga, Moscow, 1998).
4. K. N. Makarov, D. D. Malyuta, S. G. Nishchuk, *et al.*, Kvantovaya Élektron. (Moscow) **28** (1), 23 (2001).
5. S. V. Bobashev, G. S. Volkov, A. V. Golubev, *et al.*, Pis'ma Zh. Tekh. Fiz. **14** (7), 634 (1988) [Sov. Tech. Phys. Lett. **14**, 283 (1988)].
6. A. D. Akhsakhalyan, S. V. Bobashev, G. S. Volkov, *et al.*, Fiz. Plazmy **18** (4), 509 (1992) [Sov. J. Plasma Phys. **18**, 264 (1992)].
7. Attelan-Langlet, B. Etlicher, V. I. Zaitsev, *et al., Proceedings of the 12th Int. Conf. on High-Power Particle Beams, Haifa, Israel, 1998*, Vol. 1, pp. 49–52.
8. V. C. Roerich and A. E. Stepanov, Preprint TRINITI-0003-A (TsNIIAtomInform, Troitsk, 1994).
9. K. N. Makarov, Yu. A. Satov, A. P. Strel'tsov, *et al.*, Zh. Éksp. Teor. Fiz. **106**, 1649 (1994) [JETP **79**, 891 (1994)].

Translated by P. Pozdeev

Technical Physics Letters, Vol. 29, No. 3, 2003, pp. 194–196. Translated from Pis'ma v Zhurnal Tekhnicheskoĭ Fiziki, Vol. 29, No. 5, 2003, pp. 43–48.

Singular Points in the Electromagnetic Field–Waveguide System

I. V. Dzedolik

Tauride National University, Simferopol, Ukraine

e-mail: dzedolik@crimea.edu

Received September 30, 2002

Abstract—Phase trajectories of a nonlinear system of the electromagnetic field–waveguide type are studied in the vicinity of singular points. Solutions for the field components near these points are obtained. It is shown that an optical vortex appears at a singular point, the Poynting vector of which exhibits precession around this point.

The dynamics of a light field propagating in dielectric waveguides (optical fibers with various refractive index profiles) in the linear mode has been studied in sufficient detail (see [1] and references therein). A nonlinear regime of radiation propagation (see [2] and references therein) is usually studied by analysis of the dynamics of either a plane wave packet envelope (depending on the longitudinal coordinate and time) or the amplitude (which is a function of the coordinates and time), with neglect of the vector character of the field [3–5]. In this paper, the dynamics of an electromagnetic field has been studied taking into account the vector character of this field in step-index optical fibers.

Let us consider monochromatic electromagnetic radiation propagating in a step-index optical fiber. The fiber core is represented by an isotropic dielectric cylinder with a circular cross section, while the sheath is an isotropic unbounded medium with a refractive index smaller than that of the core. We will take into account the nonlinear response of the medium (doped quartz) from which the core is made, while the field in the sheath is assumed to be linear. The field vectors **E**, **D**, and **B** obey the system of Maxwell's equations in a dielectric medium,

$$\nabla\times\mathbf{B} = \frac{1}{c}\frac{\partial\mathbf{D}}{\partial t},\quad \nabla\mathbf{D} = 0,\quad \nabla\times\mathbf{E} = -\frac{1}{c}\frac{\partial\mathbf{B}}{\partial t},\quad \nabla\mathbf{B} = 0 \qquad (1)$$

with a material equation $\mathbf{D} = \mathbf{E} + 4\pi\mathbf{P}$, where $\mathbf{P} = \chi_1\mathbf{E} + \chi_3|\mathbf{E}|^2\mathbf{E}$ is the polarization vector of the medium, $\nabla = \mathbf{1}_x\partial/\partial x + \mathbf{1}_y\partial/\partial y + \mathbf{1}_z\partial/\partial z$ is the nabla operator, and $\mathbf{1}_{x,y,z}$ are the unity basis set vectors. Assuming the field to be a harmonic function of the time, ~exp($i\omega t$], we derive from Eq. (1) the Helmholtz equation for the electric vector:

$$\nabla^2\mathbf{E} + \varepsilon_1 k^2\mathbf{E} + 4\pi\chi_3 k^2|\mathbf{E}|^2\mathbf{E} = 0, \qquad (2)$$

where $\varepsilon_1 = 1 + 4\pi\chi_1$ and $k = \omega/c$. The magnetic field vector can be expressed as

$$\mathbf{B} = i\frac{c}{\omega}\nabla\times\mathbf{E}. \qquad (3)$$

Taking into account the transactional invariance of Eq. (2) along the z axis (coinciding with the longitudinal axis of the fiber), the field can be presented as the sum of modes:

$$\mathbf{E} = \mathbf{e}(r)\exp(i\kappa l\varphi - i\beta z)\quad (\kappa = \pm1,\ l = 0, 1, 2, \ldots). \qquad (4)$$

Substituting expression (4) into Eq. (2), we obtain a system of equations in cylindrical coordinates for a linear basis set $\mathbf{e}(e_x, e_y, e_z)$:

$$\left(\frac{d^2}{dR^2} + \frac{1}{R}\frac{d}{dR}\right)e_j + \left(m^2 - \frac{l^2}{R^2}\right)e_j + \alpha\left(\sum_{j=x,y,z} e_j^2\right)e_j = 0, \qquad (5)$$

where $m^2 = r_0^2(k^2\varepsilon_1 - \beta^2)$, $\alpha = 4\pi\chi_3 r_0^2 k^2$, $R = r/r_0 \in [0, 1]$, r_0 is the core radius, and $j = x, y, z$. The mode propagation constants β can be determined by equating the solutions for the tangential field components at the core–sheath interface [1].

The system of equations (5) can be represented in the form of the equation of motion of a material point under the action of a central force [6]. This is achieved through substituting $e_j = \psi_j(R)/\sqrt{R}$. Then, Eqs. (5) yield the required equations of motion in the Newton form,

$$\ddot{\psi}_x = -\frac{\partial U}{\partial\psi_x},\quad \ddot{\psi}_y = -\frac{\partial U}{\partial\psi_y},\quad \ddot{\psi}_z = -\frac{\partial U}{\partial\psi_z}, \qquad (6)$$

where

$$U = \frac{1}{2}\left[m_l^2 - \frac{l^2 - 1/4}{R^2}\right]\left(\sum_{j=x,y,z}\psi_j^2\right) + \frac{\alpha}{4R}\left(\sum_{j=x,y,z}\psi_j^2\right)^2$$

plays the role of a "potential" and the point denotes differentiation with respect to R. The system Hamiltonian is

$$H = \frac{1}{2}\sum_{j=x,y,z}\dot{\psi}_j^2 + \frac{1}{2}\left[m_l^2 - \frac{l^2-1/4}{R^2}\right]\left(\sum_{j=x,y,z}\psi_j^2\right) + \frac{\alpha}{4R}\left(\sum_{j=x,y,z}\psi_j^2\right)^2. \quad (7)$$

Introducing generalized coordinates of the system $q_j \equiv \psi_j$ and the generalized momenta $p_j \equiv \dot{\psi}_j$, we find the singular points of the system by equating the right-hand part of the Hamilton equations to zero [7]:

$$\dot{q}_j = \frac{\partial H}{\partial p_j} \equiv Q_j(q, p) = 0, \quad \dot{p}_j = -\frac{\partial H}{\partial q_j} \equiv P_j(q, p) = 0. \quad (8)$$

The first of these equations with $Q_j = p_j = 0$ yields the singular points of $p_{j0} = 0$. The second equation, with allowance for

$$P_j = \left(m_l^2 - \frac{l^2-1/4}{R^2}\right)q_j + \frac{\alpha}{R}\left(\sum_{j=x,y,z}q_j^2\right)q_j = 0,$$

yields the singular point situated at the zero ($q_{j0} = 0$) and on the surface of the sphere

$$\sum_{j=x,y,z} q_{j0}^2 = [(l^2 - 1/4)/(R - m_l^2 R)]/\alpha.$$

Singularities, where the real and imaginary parts of the field simultaneously turn zero, give rise to the optical vortices [8, 9]:

$$\mathrm{Re}E_l(x, y, z) = 0, \quad \mathrm{Im}E_l(x, y, z) = 0,$$
$$\mathrm{Re}B_l(x, y, z) = 0, \quad \mathrm{Im}B_l(x, y, z) = 0,$$

where l is the azimuthal index. These equations describe two surfaces, the intersection lines of which are the nodal lines. On a nodal line, the phase of the field is undetermined: $\tan\phi = \mathrm{Im}E_l/\mathrm{Re}E_l = \mathrm{Im}B_l/\mathrm{Re}B_l = 0/0$. A singularity of this type is the point of branching of the lth order, or a dislocation of the wave front with a topological charge of l. The azimuthal index l characterizes the topological charge of the optical vortex, which is equal to the number of 2π jumps of the field phase as a result of the transition from one to another sheet of the phase surface upon traversing the branching point.

Let us linearize the Hamiltonian system in the vicinity of the singular points

$$\bar{q}_j = q_j - q_{j0} \text{ and } \bar{p}_j = p_j - p_{j0}:$$
$$\dot{\bar{q}}_j = a_{1j}\bar{q}_j + a_{2j}\bar{p}_j, \quad \dot{\bar{p}}_j = a_{3j}\bar{q}_j + a_{4j}\bar{p}_j,$$

where $a_{1j} = \partial Q_j/\partial q_j$, $a_{2j} = \partial Q_j/\partial p_j$, $a_{3j} = \partial P_j/\partial q_j$, and $a_{4j} = \partial P_j/\partial p_j$ are the coefficients of expansion in the vicinity of the special point (q_{j0}, p_{j0}). We arrive at a linear system of equations that is topologically equivalent to the nonlinear system (6):

$$\dot{\bar{q}}_j = \bar{p}_j, \quad \dot{\bar{p}}_j = -U_0\bar{q}_j, \quad (9)$$

where

$$U_0 = m_l^2 + \alpha\left(2q_{j0}^2 + \sum_{j=x,y,z}q_{j0}^2\right)\frac{1}{R} - (l^2 - 1/4)\frac{1}{R^2}.$$

Using the equation $\frac{d\bar{p}_j}{d\bar{q}_j} = -U_0\frac{\bar{q}_j}{\bar{p}_j}$, we can find the linear phase trajectories of system (9) in the vicinity of the jth singularity $\bar{p}_j = \sqrt{-U_0}\bar{q}_j$, assuming that the potential $U_0(R)$ is a function of R as of the parameter. The slope of the phase trajectory depends on the topological charge and the radial coordinate R and decreases as $R \longrightarrow 1$.

The system (9) can be presented in the form of linear equations

$$\ddot{\bar{q}}_j = -U_0\bar{q}_j. \quad (10)$$

A solution to Eq. (10) at a singular point $q_{j0} = 0$ ($q_{j'0} \neq 0$, $q_{j''0} \neq 0$) for a potential $U_{00} = m_l^2 + \alpha(q_{j'0}^2 + q_{j''0}^2)\frac{1}{R} - (l^2 - 1/4)\frac{1}{R^2}$ is obtained in the form of a superposition of the Whittaker function:

$$\bar{q} = C_1 M(-i\tilde{\alpha}, \kappa l, i2\sqrt{m_l^2}R) + C_2 W(-i\tilde{\alpha}, \kappa l, i2\sqrt{m_l^2}R), \quad (11)$$

where $\tilde{\alpha} = \frac{\alpha}{2\sqrt{\tilde{\varepsilon}}}(q_{j'0}^2 + q_{j''0}^2)$ and, at a singular point on the sphere $q_{j'0} \neq 0$, $U_0 = -2U_{00}$, the solution is

$$\bar{q} = C_1 M(-\sqrt{2}\tilde{\alpha}, \sqrt{3/4 - 2l^2}, 2\sqrt{2m_l^2}R) + C_2 W(-\sqrt{2}\tilde{\alpha}, \sqrt{3/4 - 2l^2}, 2\sqrt{2m_l^2}R). \quad (12)$$

The constant coefficients are determined from the boundary condition $\bar{q}(R = 0)$, $\bar{p}(R = 0)$, $\bar{q}(R = 1)$, $\bar{p}(R = 1)$.

In the vicinity of a singular point, the electric field component is

$$E_j = R^{-1/2}\bar{q}_j \exp[i(\omega t + \kappa l\varphi - \beta z)], \quad (13)$$

and the magnetic field component is determined from

expression (3):

$$\mathbf{B}_j = \frac{i}{kr_0}(\nabla_R \times \mathbf{E})_j. \quad (14)$$

The Poynting vector $\mathbf{S} = \frac{c}{16\pi}(\mathbf{E} \times \mathbf{B}^* + \mathbf{E}^* \times \mathbf{B})$ averaged over time has the components

$$S_x = \frac{c}{8\pi k}\left\{\frac{\kappa l}{r}[(e_y^2 + e_z^2)\sin\varphi + e_x e_y \cos\varphi] - \beta e_x e_z\right\},$$

$$S_y = -\frac{c}{8\pi k}\left\{\frac{\kappa l}{r}[(e_x^2 + e_z^2)\cos\varphi + e_x e_y \sin\varphi] - \beta e_y e_z\right\},$$

$$S_z = \frac{c}{8\pi k}\left[\frac{\kappa l}{r} e_z(e_y \cos\varphi - e_x \sin\varphi) + \beta(e_x^2 + e_y^2)\right].$$

As can be readily seen for a nonlinear electric field propagating along the fiber, the Poynting vector for the modes with $l \neq 0$ exhibits precession around the singular points, the direction of precession being determined by the sign of the topological charge κl.

REFERENCES

1. A. W. Snyder and J. D. Love, *Optical Waveguide Theory* (Chapman and Hall, London, 1983; Radio i Svyaz', Moscow, 1987).
2. S. A. Akhmanov, V. A. Vysloukh, and A. S. Chirkin, *Optics of Femtosecond Laser Pulses* (Nauka, Moscow, 1988).
3. D. Rosas, C. T. Law, and G. A. Swartzlander, J. Opt. Soc. Am. B **14**, 3054 (1997).
4. Y. S. Kivshar, A. Nepomnyashchy, V. Tikhonenko, *et al.*, Opt. Lett. **25** (2), 123 (2000).
5. I. O. Zolotovskiĭ and D. I. Sementsov, Pis'ma Zh. Tekh. Fiz. **27** (14), 1 (2001) [Tech. Phys. Lett. **27**, 572 (2001)].
6. L. D. Landau and E. M. Lifshitz, *Course of Theoretical Physics*, Vol. 1: *Mechanics* (Nauka, Moscow, 1988; Pergamon Press, New York, 1988).
7. G. M. Zaslavsky and R. Z. Sagdeev, *Nonlinear Physics: from the Pendulum to Turbulence and Chaos* (Nauka, Moscow, 1988; Harwood, Chur, 1988).
8. I. V. Basistiy, M. S. Soskin, and M. V. Vasnetsov, Opt. Commun. **119**, 604 (1995).
9. A. V. Volyar and T. A. Fadeeva, Pis'ma Zh. Tekh. Fiz. **22** (17), 69 (1996) [Tech. Phys. Lett. **22**, 719 (1996)].

Translated by P. Pozdeev

Technical Physics Letters, Vol. 29, No. 3, 2003, pp. 197–199. Translated from Pis'ma v Zhurnal Tekhnicheskoĭ Fiziki, Vol. 29, No. 5, 2003, pp. 49–53.

A Dimensionless Criterion of Dispersion for Crystalline Solids

Yu. V. Levinsky

Moscow State Academy of Fine Chemical Technology, Moscow, Russia

e-mail: levinsky@unesco.mitht.rssi.ru

Received October 2, 2002

Abstract—A dimensionless criterion of dispersion for crystalline solids is proposed based on a comparison of the excess free energy in the compact and disperse state: $D_L = 12\sigma/Gb^2pL$, where σ is the surface energy, G is the shear modulus, b is the Burgers vector, p is the dislocation density, and L is the particle size. According to this, the critical size of particles corresponding to $D_L = 1$ is approximately the same ($L_1 = 500$ nm) for all metals. Classification of disperse crystalline solids with respect to the parameter D_L is more justified thermodynamically than characterization by the particle size. © *2003 MAIK "Nauka/Interperiodica".*

The increasing interest in studying crystalline solids in a highly disperse state is related to the prospects for creating new materials possessing unique properties [1–3]. Unfortunately, there is no commonly accepted terminology in this field. In particular, the same powders can be referred to as ultradisperse, finely disperse, submicron powders, nanopowders, etc. [2–6]. The boundaries of dispersion regions are rather arbitrarily selected, frequently based on simple technological considerations [3]. To my knowledge, no one physically, chemically, or thermodynamically justified criterion that could be applied to a sufficiently wide group of disperse materials has been suggested so far to separate the regions of dispersion for systems of particles with dimensions below 1 μm.

This paper proposes such a criterion for crystalline metal powders. The approach used to determine qualitative changes in the material properties is based on the comparison of changes in the Gibbs free energy related to the free surface energy (ΔG_S) and the energy of defects in the crystal lattice volume (ΔG_V). The main component of the excess Gibbs free energy in compact metals is the elastic energy of the crystal lattice defects, while in disperse particles, a change in the surface energy also gives an important contribution. It is natural to assume that a significant difference in behavior between disperse particles and compact metals, manifested in various chemical and physical processes, must be caused by the condition that $\Delta G_S > \Delta G_V$.

The values of ΔG_S and ΔG_V are given by the well-known formulas

$$\Delta G_S = \sigma S = \frac{6V\sigma}{L}; \quad \Delta G_V = \frac{1}{2}Gb^2\rho V, \qquad (1)$$

where σ is the specific surface energy, S is the specific surface of the powder per mole of the metal, V is the molar volume, L is the particle size, G is the shear modulus, b is the Burgers vector, and ρ is the dislocation density. The ratio of these values is a dimensionless quantity D_L, which can be called the criterion of dispersion:

$$D_L = \frac{\Delta G_S}{\Delta G_V} = \frac{12\sigma}{Gb^2\rho L}. \qquad (2)$$

The critical value of this ratio, $D_L = 1$, determines the threshold above which ($D_L > 1$) the differences in behavior of disperse and compact metals must be taken into account. Below this threshold ($D_L < 1$), this difference can be ignored. In this approach, there is no need to arbitrarily divide systems with respect to the degree of dispersion. The proposed classification is based on the numerical scale of D_L values, whereby we consider powders with, for example, $D_L \geq 10$, $10 < D_L < 50$, etc. According to this approach, the properties of particles of the same degree of dispersion are compared based on the D_L values, which is thermodynamically justified, rather that proceeding from the absolute particle size.

Expression (2) implies that the critical size L_1 of particles meeting the condition $D_L = 1$ is

$$L_1 = \frac{12\sigma}{Gb^2\rho}. \qquad (3)$$

The typical values of parameters entering in Eqs. (1)–(3) for most common metals are listed in the table. Note that, while the values of the shear modulus of metals can differ by a factor of more than 20 and the surface energies vary by a factor of about five, the corresponding values of L_1 change only by a factor of two. Taking into account the significant scatter in the values of shear modulus and surface energy obtained by differ-

The properties of various metals and the values of ΔG_S, ΔG_V, and L_1 [7, 8]

Metal	Shear modulus G, 10^{-4} MPa	Burgers vector, nm	Surface energy σ, MJ/m^2	Molar volume V, cm^3/mol	ΔG_V, J/mol (ρ = 10^{12} cm^{-2})	ΔG_S, J/mol (L = 500 nm)	L_1, nm (ρ = 10^{22} cm^{-2})
Cu	4.85	0.256	1115	7.11	120	95	420
Ag	3.00	0.289	945	10.27	128	116	712
Au	2.78	0.288	1230	10.20	118	150	640
Mg	1.75	0.321	728	14.0	252	122	484
Ca	0.76	0.394	386	26.20	117	121	392
Al	2.70	0.286	1040	10.00	110	168	564
Ti	3.96	0.295	1444	10.63	183	184	514
Zr	3.60	0.323	1498	13.97	268	251	478
Hf	5.10	0.321	1553	13.47	353	251	354
V	4.66	0.263	1878	8.36	135	188	698
Nb	3.75	0.286	2225	10.76	165	287	870
Ta	6.85	0.286	2388	10.90	305	312	506
Cr	7.40	0.250	1591	7.23	167	138	412
Mo	12.8	0.272	2240	9.39	444	252	282
W	16.0	0.274	2455	9.54	573	281	244
Fe	8.30	0.248	1480	7.09	181	126	346
Co	8.15	0.251	1445	6.70	172	116	340
Ni	7.45	0.249	1440	6.60	152	114	374

ent methods and reported by various researchers, it is possible to accept that L_1 is approximately the same for all metals and amounts to L_1 = 500 nm.

Thus, it is proposed to introduce a thermodynamic criterion determining the boundary of dispersion below which the difference in behavior between disperse particles and compact metals has to be taken into account and to use the critical particle size L_1 = 500 nm as common for all metals. It is interesting to note that 500 nm is the resolution threshold of the optical microscope.

Probably, the above approach to the criterion of dispersion can be expanded so as to include particles of other crystalline solids (oxides, carbides, nitrides, borides, etc.) and even amorphous solids provided that the maximum possible difference between the excess surface and volume energy is correctly determined. Naturally, the proposed approach to defining the criterion of dispersion and the critical particle size is neither discussionless nor exhaustive. Nevertheless, to my knowledge, these are the only justified quantities the values of which are calculated from independent physical constants.

It would be of interest to estimate the excess free energy of powders composed of particles with critical dimensions, assess the rate of increase in this energy with decreasing particle size, and compare these values with typical free energy changes in various chemical processes. Data presented in the sixth and seventh columns of the table show the excess free energy of compact metals strained to a maximum level and the excess free surface energy of the corresponding metal powders with a particle size of 500 nm. For the same metal, these parameters differ by a factor of no more than two (in accordance with the definition) and are rather small in absolute values. In particular, these values are significantly lower than the free energy of formation of most oxides, carbides, nitrides, borides, and other compounds (reaching up to tens or hundreds of kilojoules per mole). Nevertheless, the former parameters can play a significant role in some other chemical processes. Previously [9], we demonstrated that a change in the degree of carbon dispersion can significantly (by tens of percent) modify the composition of equilibrium solid solutions of carbides and nitrides.

The excess free surface energy increases in proportion to the inverse particle size. The values of ΔG_S in powders with a particle size of 50 nm (D_L = 10) are ten times as large as the corresponding values in the seventh column of the table and, hence, such powders possess an excess free energy comparable with that necessary for the formation of compounds.

Thus, the values of $L_1 = 500$ nm and $D_L = 1$ for metal powders not only serve as formal signs of dispersion but are real boundaries whose crossing implies the need to take into account a change in their thermodynamic properties.

REFERENCES

1. I. D. Morokhov, L. I. Trusov, and S. P. Chizhik, *Ultradisperse Metal Media* (Atomizdat, Moscow, 1977).
2. A. I. Gusev, *Nanocrystalline Materials: Methods of Synthesis and Properties* (Izdat. Ural. Otd. Ross. Akad. Nauk, Ekaterinburg, 1998).
3. R. A. Andrievskiĭ, Perspekt. Mater., No. 6, 5 (2001).
4. R. A. Andrievskiĭ, Usp. Khim. **63** (5), 431 (1994).
5. G. A. Libenson, V. Yu. Lopatin, and G. V. Komarnitskiĭ, *Processes of Powder Metallurgy*, Vol. 1: *Metal Powder Synthesis* (Moscow Inst. of Metals and Alloys, Moscow, 2001).
6. L. I. Klyachko, V. A. Fal'kovskiĭ, and A. M. Khokhlov, *Hard Alloys of Tungsten Carbides with Finely Disperse Structure* (Ruda i Metally, Moscow, 1999).
7. J. Friedel, *Dislocations* (Pergamon Press, Oxford, 1964; Mir, Moscow, 1967).
8. *Properties of Elements: A Handbook*, Ed. by G. V. Samsonov (Metallurgiya, Moscow, 1976).
9. Yu. V. Levinskiĭ, A. P. Petrov, and Saul S. Namango, Izv. Vyssh. Uchebn. Zaved., Tsvet. Met., No. 1, 44 (2002).

Translated by P. Pozdeev

Technical Physics Letters, Vol. 29, No. 3, 2003, pp. 200–202. Translated from Pis'ma v Zhurnal Tekhnicheskoĭ Fiziki, Vol. 29, No. 5, 2003, pp. 54–60.

Tunneling Magnetoresistance in a $Eu_{0.7}Pb_{0.3}MnO_3$ (Single Crystal)–Fe (Film) Structure

N. V. Volkov, G. S. Patrin, G. A. Petrakovskii, K. A. Sablina, S. G. Ovchinnikov, and S. N. Varnakov

Kirensky Institute of Physics, Siberian Division, Russian Academy of Sciences, Krasnoyarsk, Russia
Krasnoyarsk State University, Krasnoyarsk, Russia
e-mail: volk@iph.krasn.ru
Received October 3, 2002

Abstract—We have studied the magnetoresistive properties of a structure comprising single crystal manganite $Eu_{0.7}Pb_{0.3}MnO_3$ covered with an epitaxial iron film. At temperatures below T_C of the manganite crystal, the structure exhibits positive magnetoresistance. The behavior of the resistance as a function of the magnetic field is characteristic of a tunneling junction with ferromagnetic electrodes separated by a thin insulating film. The observed effect is related to the formation of a transition layer at the manganite–Fe interface, which is depleted of oxygen and possesses dielectric properties. The sensitivity of the resistance with respect to the magnetic field is determined both by the negative magnetoresistance of the manganite crystal and by the tunneling contribution to the conductivity, whereby the tunneling current depends on the mutual orientation of magnetic moments of the electrodes ($Eu_{0.7}Pb_{0.3}MnO_3$ crystal and Fe film). © *2003 MAIK "Nauka/Interperiodica".*

Investigation into spin-dependent transport via heterostructures containing magnetically active layers is among currently important and highly promising directions in the physics of magnetic phenomena. These hopes are related to the large application potential of such structures [1]. Indeed, such structures, retaining all advantages of the traditional semiconductor (nonmagnetic) low-dimensional systems, acquire an additional channel of control via magnetic field [2]. This possibility greatly expands the functional properties of microelectronic devices. One of the related problems encountered in this way is the search for new materials providing for a high spin polarization of electrons emitted into a magnetic structure. A promising solution is offered by ferromagnetic semiconductors based on magnesium oxides with a perovskite structure, known as manganites. These compounds are characterized by a high degree of spin polarization of the intrinsic carriers, reaching nearly 100% [3].

Below, we report on the results of investigations of the magnetoresistive properties of a structure comprising single crystal manganite covered with an epitaxial iron film ([M/Fe]). The single crystals of $Eu_{0.7}Pb_{0.3}MnO_3$ manganite were grown by spontaneous crystallization from a solution melt. The samples exhibited a transition to the ferromagnetic state with a metal conductivity at T_C = 210 K. The substrates cut from single crystal ingots had the shape of 3 × 2 × 0.1 mm plates, in which the large plane coincided with one of the principal crystal planes. An iron film with a thickness of 250 Å was deposited by molecular beam epitaxy on a commercial setup of the Angara type. Copper films with thicknesses up to ~500 Å deposited in the same technological cycle onto the outer iron film surface and onto the bottom substrate surface were used as electrodes during electric measurements on the [M/Fe] structures. The experimental geometry is outlined in the inset to Fig. 1.

Figure 1a shows a plot of the resistance $R(H)$ and magnetoresistance $(MR)\Delta R/R_0 = (R(H) - R(0))/R(0)$ as functions of the applied magnetic field for the [M/Fe] structures studied at T = 80 K. For comparison, Fig. 1b presents an analogous curve for the substrate (single crystal manganite). As can be seen, the $R(H)$ curve for the [M/Fe] sample exhibits a characteristic maximum representing the region of positive MR. As is well known, manganites proper exhibit a negative MR effect, which is clearly observed for the single crystal of $Eu_{0.7}Pb_{0.3}MnO_3$. A comparative analysis showed that, in magnetic fields above H ~ 11 kOe, the change in the sample resistance is determined entirely by the MR properties of the substrate. Since the resistance of the [M/Fe] structure is about three times that of the substrate, it is natural to suggest that the features of $R(H)$ of the structure are related to the formation of a transition layer between the iron film and the manganite substrate.

A peak corresponding to the positive MR region on the $R(H)$ curve begins to appear in weak magnetic fields at $T < T_C$. As the temperature decreases, the maximum $R_m = R(H_m)$ shifts toward greater magnetic fields (H_m is the field strength corresponding to the maximum value of $R(H)$) and the magnitude of the MR effect ($\Delta R_m = R_m - R_0$) increases. On the whole, the character of the

1063-7850/03/2903-0200$24.00

temperature variation of ΔR_m and H_m is correlated with the behavior of magnetization of the manganite crystal. It is important to note that the region corresponding to positive MR values appears only in the interval of temperatures at which the manganite crystal possesses a spontaneous magnetic moment.

Another important feature is that the magnitude of the MR effect depends on the bias voltage V applied to a sample during the resistance measurements. This behavior is characteristic of the tunneling transitions between electrodes of a ferromagnetic material separated by a thin dielectric layer ([FM_I/I/FM_{II}] structures). The presence of the R_m peak is related to the spin valve effect [3], the tunneling current being dependent on the magnetic moments of electrodes. The contact resistance is minimal when these moments ($\mathbf{M}_I$ and $\mathbf{M}_{II}$) are parallel to each other, and the resistance is maximal when the moments are antiparallel. In our case, the role of the magnetically active electrodes is performed by the iron film and manganite crystal (for $T < T_C$). Additional evidence for the proposed mechanism of the tunneling MR in the structure studied is provided by the current–voltage characteristic (Fig. 2) possessing a shape typical of the tunneling junctions [4]. In contrast, the current–voltage characteristic of the substrate (single crystal manganite) is linear.

Let us consider the possible mechanism of the formation of a transition layer between a manganite crystal and an epitaxial iron film. As is well known, manganites are characterized by a weak binding of oxygen to the lattice and a relatively easy diffusion of this component. On the other hand, manganites are extremely sensitive to deviations from the crystal stoichiometry in oxygen [5]. For some compositions, a decrease in the oxygen content resulted in the sample (exhibiting ferromagnetic/conducting properties in the stoichiometric state) acquiring dielectric properties with an antiferromagnetic type of ordering [6]. Thus, it seems that the stoichiometry with respect to oxygen is a decisive factor determining the properties of near- surface layers in manganites, including the transition layers between the crystal substrate and a film.

In our case, the situation can be as follows. The interface between the crystal and the film features mutual diffusion that results in the formation of a thin layer depleted of oxygen as compared to the stoichiometry. This layer, possessing dielectric properties, plays the role of a potential barrier for electrons. Using the classical expression of Simmons [4] for the tunneling current via a potential barrier, we calculated a current–voltage characteristic approximating the curves experimentally measured for the [M/Fe] structures. From this we estimated the height U_0 and width d of the aforementioned potential barrier: $U_0 \approx 29.5$ meV and $d \approx 20$ Å. Obviously, these estimates are quite rough and can be considered as a lower boundary for the real values of U_0 and d, since the tunneling mechanism of conductivity is probably not dominating at high temperatures ($T > 80$ K) and the over-barrier transport of charge carriers (thermoelectron emission) has to be taken into consideration as well. In addition, the interfacial region is likely to be inhomogeneous [7] and may contain microscopic highly conducting inclusions percolating through the barrier.

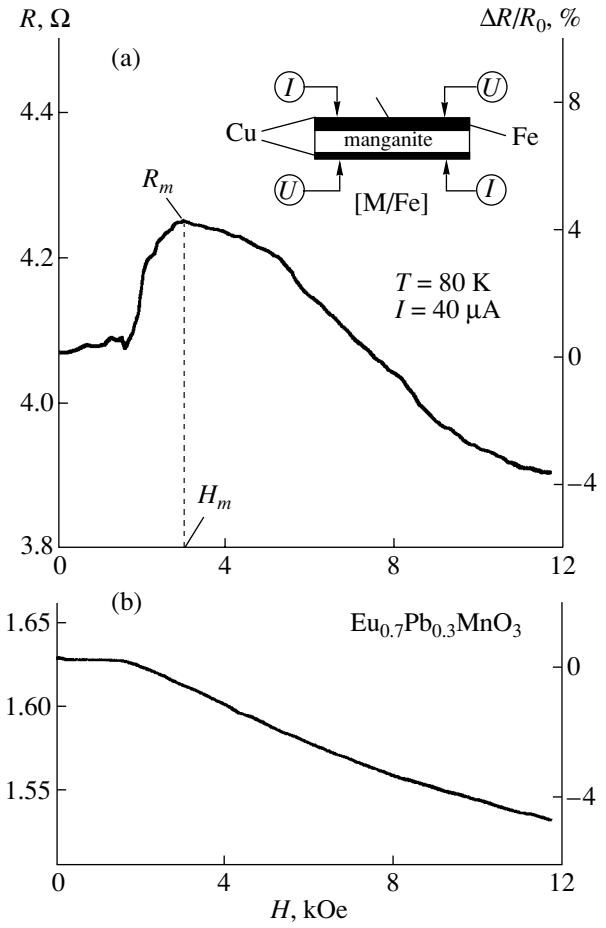

Fig. 1. Plots of the resistance $R(H)$ and magnetoresistance $\Delta R/R_0 = (R(H) - R(0))R(0)$ versus the applied magnetic field at $T = 80$ K for (a) the [M/Fe] structure studied and (b) the substrate ($Eu_{0.7}Pb_{0.3}MnO_3$ single crystal). The inset shows a schematic diagram of the experimental arrangement.

The spin valve effects are traditionally observed and characterized using the structures in which ferromagnetic films are separated by dielectric spacers, so that the electrodes are magnetically uncoupled. A difference in the behavior of magnetic moments $\mathbf{M}_I$ and $\mathbf{M}_{II}$ as the functions of H and, hence, a change in the tunneling current via the junction can be realized by selecting the materials for FM_I and FM_{II} possessing different coercive fields (H_{CI} and H_{CII}, respectively). In this case, the $R(H)$ curve exhibits a considerable hysteresis. No such hysteresis was observed in the [M/Fe] structures studied in our experiments. Another distinctive feature is that the magnetic field strength (H_m) corresponding to the maximum resistance R_m has a large value (H_m =

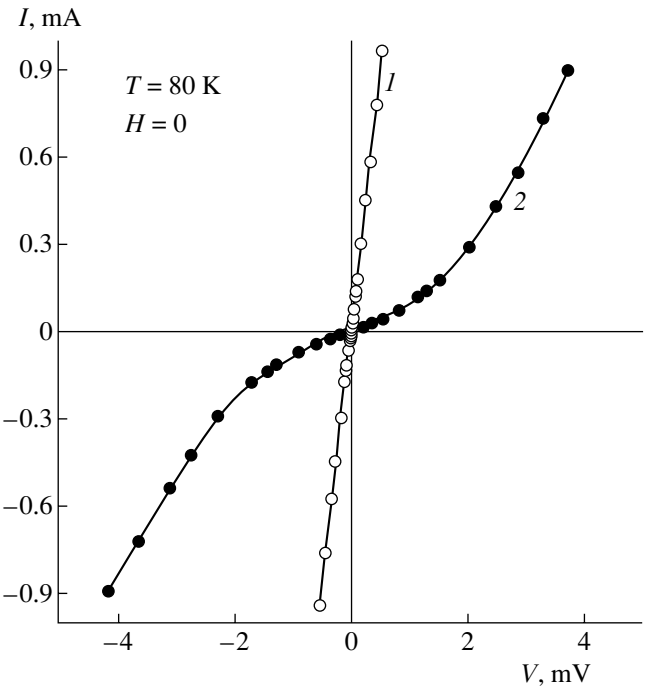

Fig. 2. Current–voltage characteristics of (*1*) a $Eu_{0.7}Pb_{0.3}MnO_3$ single crystal and (*2*) a [M/Fe] structure at $T = 80$ K.

3.3 kOe), which is significantly greater than the analogous H_C values for $Eu_{0.7}Pb_{0.3}MnO_3$ crystals and iron films taken separately.

This behavior can be rationalized by assuming that the dielectric transition layer possesses magnetic properties and mediates an exchange interaction between the manganite crystal and the iron film, this interaction possessing an antiferromagnetic character (as was indicated above). The equilibrium angle θ between the magnetic moments $\mathbf{M}_{\mathrm{I}}$ and $\mathbf{M}_{\mathrm{II}}$ is determined by the condition of the minimum free energy density:

$$F(\theta) = F_{EX} + E_Z + E_D + E_A,$$

where E_{EX} is the energy of the exchange interaction between electrodes, E_Z is the Zeeman energy in the applied field, E_D is the energy of a demagnetization field, and E_A is the energy of the magnetic anisotropy. A possible scenario for the tunneling contribution to $R(H)$ is as follows. For $H = 0$, both the manganite and the iron film occur in a multidomain state with all relative orientations of $\mathbf{M}_{\mathrm{I}}$ and $\mathbf{M}_{\mathrm{II}}$ in the plane being equiprobable. As the field strength H increases, the magnetization proceeds and a saturation magnetization of the crystal and film is attained at $H \approx H_m$. The antiferromagnetic exchange via the near-surface layer results in an approximately antiparallel orientation of $\mathbf{M}_{\mathrm{I}}$ and $\mathbf{M}_{\mathrm{II}}$ and the structure is characterized by a maximum value of $R(H)$. As the field H increases further, competition (mostly between E_{EX} and E_Z contributions to $F(\theta)$) takes place, the equilibrium angle θ decreases, and $R(H)$ drops. For $H \sim 11$ kOe, the moments $\mathbf{M}_{\mathrm{I}}$ and $\mathbf{M}_{\mathrm{II}}$ become parallel; at still higher fields, the MR of the structure is dominated by the contribution of the substrate, which is not related to the tunneling mechanism.

The proposed scenario qualitatively explains the observed behavior of MR in the [M/Fe] structure studied. The situation will be elucidated in greater detail by investigations of the behavior of the magnetizations of the manganite crystal and the deposited iron film.

Acknowledgments. This study was supported by the Russian Foundation for Basic Research (project no. 02-02-172224) and by the joint program Yenisei-2002 (project no. 02-02-97702).

REFERENCES

1. P. Grunberg, Phys. Today **54**, 31 (2001).
2. A. S. Borukhovich, N. A. Viglin, and V. V. Osipov, Fiz. Tverd. Tela (St. Petersburg) **44** (5), 898 (2002) [Phys. Solid State **44**, 938 (2002)].
3. R. Meservey and P. W. Tedrow, Phys. Rep. **239**, 174 (1994).
4. J. G. Simmons, J. Appl. Phys. **34**, 1793 (1963).
5. H. L. Ju and H. Sohn, J. Magn. Magn. Mater. **167**, 200 (1997).
6. S. Tamura, Phys. Lett. A **73A**, 401 (1980).
7. V. M. Svistunov, Yu. V. Medvedev, V. Yu. Tarenkov, *et al.,* Zh. Éksp. Teor. Fiz. **118**, 629 (2000) [JETP **91**, 547 (2000)].

Translated by P. Pozdeev

Technical Physics Letters, Vol. 29, No. 3, 2003, pp. 203–206. Translated from Pis'ma v Zhurnal Tekhnicheskoĭ Fiziki, Vol. 29, No. 5, 2003, pp. 61–70.

Radiation-Thermal Effects in Single Crystal Corundum

I. Kh. Abdukadyrova

Institute of Nuclear Physics, Academy of Sciences of the Republic of Uzbekistan, Tashkent, Uzbekistan
e-mail: said@suninp.tashkent.su

Received October 3, 2002

Abstract—Radiation-thermal effects were studied in corundum single crystals exposed to an ionizing radiation. The laws of variation of the electrical properties of a target material under the action of these factors were established. In particular, it is established that the dose dependence of the electric conductivity of irradiated samples is described by a curve with extremum. The radiation-induced phenomena observed are explained within the framework of existing models. The temperature dependence of the dielectric loss tangent of irradiated samples changes in a complicated manner (in particular, a maximum appears in this curve). There are two temperature regions in which the loss tangent exhibits special features. The activation energies have been determined and a hypothesis about the nature of the observed dielectric absorption is formulated. © *2003 MAIK "Nauka/Interperiodica".*

Introduction. Corundum is a unique optical and insulation material that is extremely hard and possesses high thermal, chemical, and radiation stability. In recent years, this aluminum oxide polytype has been considered among the most promising insulating materials for thermonuclear reactors. In addition, corundum is a component in many high-alumina substances widely used as structural materials in nuclear technologies (nuclear reactors and power plants). Therefore, investigation of the radiation effects in corundum crystals and related insulating materials, determination of the nature of these phenomena, and elucidation of their mechanisms are very important problems [1–4]. This is confirmed by recent publications [5, 6] expanding the range of applications of corundum-based dielectric materials.

Some investigations were devoted to studying the effects of radiation on the electrical properties of corundum [2, 7, 8]. In particular, Aseev [2] demonstrated that bombardment with neutrons increased the electric conductivity of corundum samples. Huntley [7] studied the influence of the absorbed gamma radiation dose rate on the conductivity of alumina single crystals and sintered powder samples and showed the role of impurities in this phenomenon. Dau and Davis [8] determined the change in the conductivity of polycrystalline corundum irradiated in a reactor and showed the dependence of this change on the reactor power. It should be noted that most investigations were conducted with sintered polycrystalline samples, in which a single parameter (e.g., conductivity) was monitored immediately in the course of irradiation. The nature of processes taking place in corundum under irradiation is still under discussion.

In this context, it was of interest to perform a systematic study of the effect of increasing the dose of radiation of the same type on some electrical properties of identical samples of single crystal corundum. It was also important to measure all parameters after termination of the exposure, since the mechanisms of the steady-state radiation effect are still incompletely clear.

Methods of investigation and sample preparation. The experiments were performed with single crystal corundum of a high-purity grade (characterized by a content of uncontrolled impurities within 0.001–0.0001 wt %), which were cut parallel and perpendicular to the optical axis of an ingot grown by the Verneuil technique. Since the values of the main characteristics in the crystals of both orientations were close, the data presented below refer to the samples of the latter type (perpendicular orientation). The samples had the shape of discs with a diameter of 22 mm and a thickness of 1.7 mm, and the electrodes were connected via vacuum-deposited nickel contacts. The samples were exposed to an ionizing radiation from a ^{60}Co source. The interval of absorbed doses was varied from 100 Gy to 1 MGy, at an absorbed dose rate in the source channel amounting to 12–13 Gy/s.

The samples were characterized with respect to their electrical properties, including electric conductivity σ, dielectric loss tangent $\tan\delta$, and permittivity ε. The measurements were performed in both dc and ac modes using an ac bridge and the IPD-1 and EKB-11 instruments in the range of temperatures from 25 to 400°C.

Results and discussion. Figure 1 shows plots of the temperature dependence of the dc conductivity for a corundum single crystal measured before and after gamma irradiation to a dose of D = 10 kGy. As can be seen, the shapes of both curves are qualitatively similar, but the conductivity of the irradiated crystal is lower than that of the unirradiated one in the entire temperature range. The observed radiation-induced decrease in the conductivity of single crystal corundum is at vari-

1063-7850/03/2903-0203$24.00

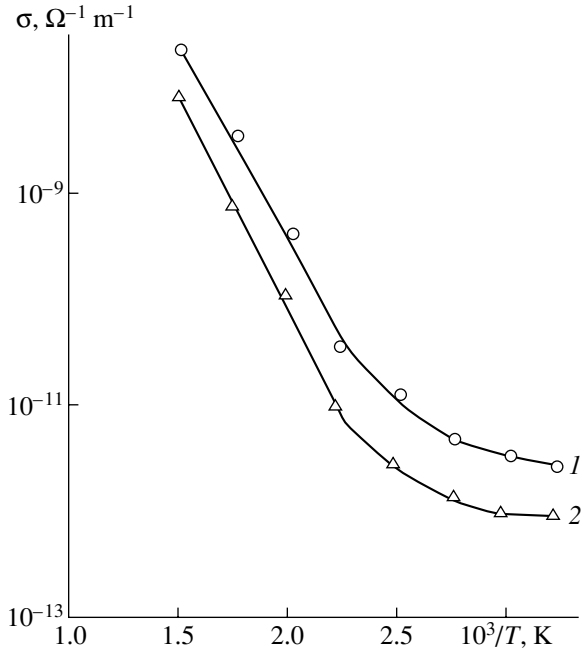

Fig. 1. Temperature dependence of the conductivity of (*1*) unirradiated and (*2*) gamma-irradiated corundum crystal.

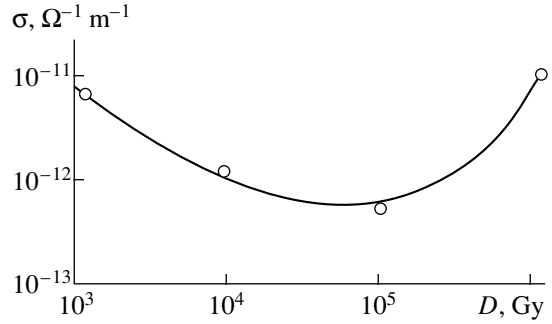

Fig. 2. Dose dependence of the conductivity of gamma-irradiated single crystal corundum.

ance with the behavior reported in [2, 8], where this value increased in both sintered (polycrystalline) and single crystal samples irradiated in a reactor. The conductivity of irradiated samples changed from 8×10^{-13} to 7.7×10^{-9} Ω^{-1} m^{-1} with increasing temperature. A certain acceleration of the growth rate was observed at T = 150°C, where the temperature dependence exhibited a break. The position of this point was not affected by irradiation. This behavior indicates that there are two components in the conductivity and that this character is retained after irradiation.

Table 1. Conductivity activation energies E for various temperatures (T) and irradiation doses (D)

Dose, kGy	T_1, °C	E_1, eV	Dose, kGy	T_2, °C	E_2, eV
0	<150	0.29	0	>150	0.68
10	<150	0.20	10	>150	0.78

It was demonstrated [8] that the behavior of $\sigma(T, P)$ in irradiated single crystal corundum could be described by a relation established for ceramics:

$$\sigma(T, P) = A\exp(-B/T) + aPT^{3/2}, \qquad (1)$$

where A, B, and a are empirical coefficients depending on the material, radiation type, and temperature, and P is the absorbed dose rate of gamma radiation. The coefficients in formula (1) calculated for single crystal corundum showed satisfactory agreement with the values for a corundum-based ceramics of the UF-46 type. This result confirms the assumption that the gamma component of the reactor radiation acting upon the crystalline phase of ceramics produces a dominating contribution to changes in this electric parameter [10].

The conductivity activation energies E for unirradiated and gamma-irradiated samples of corundum, calculated from the experimental temperature dependences of σ measured in the two temperature intervals, are listed in Table 1. As can be seen from these data, the exposure only leads to insignificant fluctuations in the E value, which confirms the above statement that the character of conductivity is retained upon irradiation of the crystal. Some change in the activation energy observed for the high-temperature region is probably explained by an additional conductivity component related to the motion of weakly bound ions (e.g., oxygen ions) over vacancies in the lattice (in agreement with the Deans conductivity mechanism for ionic crystals). In addition, this modified activation energy has proved to be close to analogous value determined for UF-46 ceramics, which confirms a contribution due to the crystalline phase in these materials.

In order to refine the aforementioned effect of the radiation-induced decrease in the electric conductivity of corundum, the dose dependence of σ was measured in the course of subsequent irradiation to greater doses. The resulting curve of $\sigma(D)$ measured at T = 100°C is presented in Fig. 2. It was found that a decrease in the conductivity continues up to a dose of 0.1 MGy, after which the trend changes to the opposite. Thus, it was established for the first time that the dose dependence of the electric parameter exhibits an extremal behavior, passing through a minimum in the region of 0.1 MGy and then virtually returning to the initial level at large doses (D > 1 MGy). This behavior reveals radiation annealing of an induced structural defect in single crystal corundum.

It is important to explain the observed radiation-induced change in the electric conductivity of the crystalline insulator studied. Defect centers of the V-type in the gamma-irradiated corundum crystals were reported in [1, 3]. According to the Seitz model, these centers are capable of forming groups of defects, leading to a

decrease in the conductivity. As is known, gamma irradiation leads to an increase in the radiation-induced conductivity according to the formula [8]

$$\sigma = en\mu, \quad (2)$$

where e is the elementary charge, n is the charge carrier density, and μ is their mobility. According to formula (2) and the aforementioned model, the irradiation leads to a decrease in n and, hence, in the conductivity of exposed samples.

Table 2 presents the results of measurements of another electric parameter—the dielectric loss tangent at 300 Hz—for the samples of corundum before irradiation and after the exposure to a dose of 10 kGy at various temperatures. According to these experimental data, the $\tan\delta(T)$ function in both unirradiated and gamma-irradiated crystals changes nonlinearly and exhibits an anomaly in the low-temperature region. In the former case, losses below 200°C decrease and the function has a break at this temperature, whereby $\tan\delta$ exhibits a jump and keeps increasing up to the limiting temperature. Irradiation of the sample to a dose of 10 kGy complicated the behavior in the low-temperature region, whereby an intermediate stage above 150°C appears with a peak at 250°C. In addition, a comparative analysis of the temperature dependence of losses in the two samples showed that the $\tan\delta(T)$ function of the irradiated crystal lies above that of the initial crystal, while at higher temperatures the pattern is reversed.

Thus, the temperature dependence of the dielectric loss tangent of corundum varies in a complicated manner, showing different behavior in two specific temperature intervals, the low- and high-temperature ones. Apparently, the mechanism of losses in the two regions is also different.

The dielectric permittivity of corundum crystals was calculated by the formula [11]

$$\varepsilon = d/(\varepsilon_0 S)C_\delta, \quad (3)$$

where C_δ is the capacitance, S is the electrode area, d is the insulator layer thickness, and ε_0 is the permittivity of vacuum. The results of calculations by formula (3) are listed in Table 2 for the irradiated and unirradiated samples measured at 300 Hz. As can be seen, the permittivity of the initial material increases with the temperature, the most rapid growth taking place at $T >$ 150°C. Note that the permittivity in the temperature range studied increases upon irradiation. This can be related to an increase in the defectness of the insulator structure and to a contribution of the temperature-dependent polarization processes to the permittivity value.

A detailed comparative analysis of the $\tan\delta(T)$ and $\varepsilon(T)$ functions obtained for the gamma-irradiated corundum crystals showed that both curves differ from those of the initial samples in the entire temperature range, with special features in the region of 150–300°C showing manifestations of additional dielectric absorption. It was of interest to elucidate the reasons for this anomalous behavior.

Table 2. Temperature variation of the dielectric loss tangent and permittivity of corundum

T, °C	$\tan\delta$ (unirradiated)	$\tan\delta$ (irradiated)	ε (unirradiated)	ε (irradiated)
50	0.0027	0.0085	11.75	12.06
100	0.0020	0.0032	11.78	12.15
150	0.0015	0.0021	11.83	12.18
200	0.0010	0.0030	11.83	12.25
250	0.0100	0.0065	11.83	12.31
300	0.0250	0.0045	12.09	12.40
350	0.0380	0.0085	12.38	12.50
400	0.0730	0.0210	12.65	12.64

It was reported [1, 3, 9] that ionizing radiation is capable of influencing the optical and electron paramagnetic resonance (EPR) spectra of corundum and of producing and annealing the F- and V-centers. This fact, together with (i) the results of experiments on the thermal annealing (discoloration) of the radiation-induced coloration centers (at 205, 230, 257, and 400 nm), (ii) a correlation with the temperature region (150–250°C) featuring a maximum discoloration rate in the main stage of the isochronous annealing of irradiated crystals and a maximum in the temperature dependence of the angle of dielectric losses, and (iii) the absence of a shift in the position of this peak with the frequency, allow us to suggest that one factor accounting for the extra dielectric absorption is the appearance of an additional electron current component in the above temperature interval and the other factor is the polarization phenomena. In order to elucidate these factors, consider the following.

It is believed that the observed radiation-induced effect, whereby the dielectric absorption appears in the region of elevated temperatures, is related most probably to the dielectric polarization, in particular, to the relaxation polarization. The relaxation time τ of the thermal ion polarization depends on the nature of substance and on the temperature. Assume a single crystal insulator in which all atoms involved in the thermal ion polarization possess the same activation energy and, accordingly, the same relaxation time τ_0 [11]. Then, the exponential temperature dependence of τ for the ion polarization can be written as

$$\tau = \tau_0 \exp(E_p/\kappa T), \quad (4)$$

where κ is the Boltzmann constant, T is the absolute temperature, and E_p is the polarization activation energy.

Using formula (4), we obtain the following expression for the activation energy:

$$E_p = \ln(\tau/\tau_0)kT. \quad (5)$$

Substituting the known values of constants and the parameters of dielectric absorption determined for the samples studied and taking into account the maximum of losses at $\omega\tau_0 = 1$, we obtain the polarization activation energy $E_p = 0.76$ eV. An almost twofold increase in the electric field frequency virtually did not influence this activation energy (which only slightly decreased). Thus, a sharp variation in the parameter determining the alternating field acting upon the insulator particles did not result in a comparable change in their binding.

A comparison of the above energy values shows that the polarization activation energy E_p is close to the charge carrier activation energy determined from the temperature dependence of the electric conductivity (E_2) in the high-temperature region. Assuming that the thermal polarization leads predominantly to the motion of weakly bound ions over the insulator volume, we may conclude that the most probable potential barrier for these weakly bound ions is an average value close to a potential barrier for the ions involved in the charge transfer.

In view of the absence of analogous experimental data for like single crystal oxides subjected to ionizing radiation, let us consider the data reported in [10], where an estimate of the thermal ion activation energy in a disordered insulator was determined (~0.77 eV). As is seen, this value coincides with E_2 and is close to E_p determined in the experiments described above. Thus, to the first approximation, there is a qualitative agreement between theoretical estimates of the parameter studied [10] and the experiment. This fact is evidence for the hypothesis that the main contribution to the observed effect is due to the polarization phenomena.

To summarize, it can be stated that the function $\tan\delta(T)$ for gamma-irradiated single crystal corundum exhibits a complicated behavior with two pronounced specific regions corresponding to the relaxation losses and conductivity.

Conclusions. (i) The laws of radiation-thermal changes in the electrical properties of single crystal corundum under the action of ionizing radiation have been established.

(ii) The conductivity activation energy values have been determined. These values are retained upon irradiation, which is indicative of the absence of significant changes in the mechanism of ion conductivity of the crystal studied.

(iii) The irradiation leads to a decrease in the electric conductivity of the sample studied. Possible reasons have been considered in terms of the Seitz model. An extremal behavior of the dose dependence of the conductivity of corundum has been observed with a minimum at 0.1 MGy, which is indicative of the radiation annealing of an induced defect at $D \cong 1$ MGy.

(iv) The temperature dependence of the dielectric loss tangent in the irradiated crystal exhibits a complicated shape with an additional maximum. This dependence reveals two specific regions corresponding to the conductivity and relaxation losses, with different mechanisms of dielectric losses.

REFERENCES

1. Ya. A. Valbis and M. S. Springis, *Electron and Ion Processes in Ionic Crystals* (Zinatne, Riga, 1980), pp. 3–15.
2. N. A. Aseev, Atomnaya Énerg. **32**, 326 (1972).
3. T. J. Turner and J. H. Crawford, Solid State Commun. **17**, 167 (1975).
4. L. W. Hobbs, F. W. Clinard, S. Y. Zincle, *et al.*, J. Nucl. Mater. **216**, 291 (1994).
5. Yu. N. Barabanenkov, V. V. Ivanov, S. N. Ivanov, *et al.*, Zh. Éksp. Teor. Fiz. **119**, 546 (2001) [JETP **92**, 474 (2001)].
6. I. P. Fesenko, Sverkhtverd. Mater. **2**, 15 (2001).
7. D. Huntley, Can. J. Phys. **46**, 312 (1968).
8. G. J. Dau and V. V. Davis, Nucl. Sci. Eng. **25**, 223 (1966).
9. K. H. Lee and J. H. Crawford, Appl. Phys. Lett. **33**, 273 (1978).
10. N. S. Kostyukov, M. I. Muminom, *et al.*, *Radiation-Induced Electric Conductivity* (Nauka, Moscow, 2001).
11. I. S. Rez and Yu. I. Poplavko, *Dielectrics* (Moscow, 1989).

Translated by P. Pozdeev

Technical Physics Letters, Vol. 29, No. 3, 2003, pp. 207–209. Translated from Pis'ma v Zhurnal Tekhnicheskoĭ Fiziki, Vol. 29, No. 5, 2003, pp. 71–77.

Degradation of Hydrocarbons in the Cavitation Region Activated by Aqueous Electrolyte Solutions in the Presence of Electric Field

A. S. Besov, K. Yu. Koltunov, S. O. Brulev, V. N. Kirilenko, S. I. Kuz'menkov, and E. I. Pal'chikov

Lavrentiev Institute of Hydrodynamics, Siberian Division, Russian Academy of Sciences, Novosibirsk, Russia
Novosibirsk State University, Novosibirsk, Russia
"Interbiznesproekt" Company, Barnaul, Russia
e-mail: besov@hydro.nsc.ru
Received October 8, 2002

Abstract—The results of experiments with *n*-octane and *n*-decane show that effective chemical degradation of hydrocarbons in a process of the thermal cracking type under the action of pulsed heating and high pressure in the cavitation region is possible in the presence of a strong electric field ($E > 10$ kV/cm) and aqueous electrolyte solutions supplied to the cavitation region at a controlled rate. *© 2003 MAIK "Nauka/Interperiodica".*

There are several groups of researchers engaged in the development of effective hydrocarbon degradation (pyrolysis) processes which can be implemented using small-scale technological equipment. One promising direction is related to systems employing the cavitation phenomenon [1–3], in which the cavitation bubbles play the role of reactors with high internal pressures and temperatures. The main condition of thermal cracking (thermolysis) and oxidation by molecular oxygen (autooxidation) of hydrocarbons in the classical technological processes is the increase in the temperature of reactants (up to at least 400–600°C) and in the pressure (to 2–4 MPa) in the entire working volume. However, this condition is not necessary in reactors of the cavitation type, where the conversion can take place inside and in the vicinity of collapsing bubbles containing reactants in the gas phase. Such a bubble operates like a reactor in which the temperature periodically (at a frequency of ~10^4 Hz) increases up to a level significantly exceeding that necessary for the reaction. These conditions are operative for a few fractions of microsecond. However, despite the relatively short interaction time and the small amount of substances reacting in each particular bubble, the total yield of the reaction products can be significant.

There is certain progress in this direction [4, 5]. Kurochkin *et al.* [5] employed a cavitation reactor for the processing of residual oil. Kirilenko *et al.* [6, 7] patented methods for the degradation processing of high-boiling oil fractions and for increasing the octane number of an oil rectificate and gas condensate. Note that the principal means of increasing the octane number and conditioning the fuel consists in adding special components (compounds), in particular, methyl–*tert*-butyl ester and some other oxygen-containing organic compounds [8]. Evidently, an alternative approach can be based on the autooxidation processes leading to a partial yield of the oxygen-containing organic compounds (up to 10–15%) immediately in the course of the raw hydrocarbon material processing. This can be achieved by adding molecular oxygen (air) into the cavitation region. As is known, analogous reactions of liquid- and gas-phase oxidation of hydrocarbons in a classical high-temperature regime are employed in some commercial processes [9].

The limiting stage in the thermolysis of saturated hydrocarbons (alkanes) is the rupture of C–C or C–H bonds with the formation of free radicals:

$$R - R' \longrightarrow R^{\bullet} + R'^{\bullet}.$$

If the degree of conversion is sufficiently high (0.1–1%), the reaction can exhibit acceleration, proceeding by the chain mechanism. The probability of degradation is significantly (2–5 times) higher for long hydrocarbon chains than for short ones, which provides for the preferential conversion of heavy fractions of both oil and condensate. The average energy required for the breakage of one C–C bond is 3.6 eV (346 kJ/mol) [10], which is equivalent to the average energy of a photon emitted from a blackbody with a temperature of 36000°C. Obviously, reaching such temperatures inside the cavitation bubbles, even if it were possible, would require special conditions and adjustment of the cavitation regime. By no means can all cavitation systems operate under such conditions. This is probably one of the factors explaining the slow progress in the commercial implementation of cavitation technologies. On the other hand, a simple cell with a potential differ-

1063-7850/03/2903-0207$24.00 © 2003 MAIK "Nauka/Interperiodica"

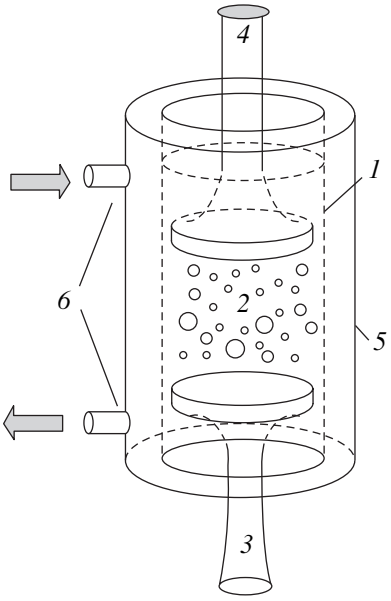

Schematic diagram of the experimental cell. See the text for explanations.

ence above 3.6 V can readily provide an electron with an energy sufficient for the C–C bond breakage. The only question is how to drive this energy to the bond breakage. Therefore, the problem reduces to searching for an effective means of generating free radicals in the gas phase followed by their transfer to (or via) a liquid phase. It was suggested that the problem can be solved by combining the action of two factors: cavitation and electric field.

Attempts at using the electric field for activating the process of hydrocarbon degradation under conditions of ultrasonic cavitation were previously described in [11]. It was demonstrated that, when a dc voltage between electrodes confining the cavitation region exceeds a certain threshold level (on the order of 10 kV/cm), the frequency of acoustoluminescence pulses grows. A sufficiently long (a few hours) action of ultrasonic and electric fields led to significant chemical changes in the liquid media studied. In particular, alkanes (*n*-octane and *n*-decane) acquired a yellowish tint and exhibited certain qualitative reactions characteristic of unsaturated hydrocarbons (e.g., discoloration of an aqueous $KMnO_4$ solution). Such reactions were observed even under conditions of a rather insignificant (below 0.1%) degree of degradation of the initial hydrocarbons. These results, while being of interest from a basic standpoint, led to no effective technical solutions.

In this study, we repeated the experiments with the combined action of cavitation and electric field on hydrocarbons such as *n*-octane and *n*-decane. The experimental arrangement is schematically depicted in the figure. In contrast to the scheme employed in [11], radiator *3* acted upon a hydrocarbon contained in a glass cylinder *1* of a somewhat greater diameter. The cavitation zone *2* is localized between radiator *3* and high-voltage electrode *4*, which is identical to electrode *3* (diameter, 15 mm; working frequency, 22 kHz). The electric field strength between electrodes *3* and *4* was controlled (from 10 to 20 kV/cm) by changing the interelectrode distance. The maximum dc voltage of the high-voltage converter was 25 kV. The reaction zone was cooled by water flowing between cell *1* and external glass cylinder *5* (with inlet and outlet fingers *6*).

Prolonged (several hours) processing led to the effects described in [11], but the concentration of decomposition products did not exceed a few hundredth of per cent and the current between the high-voltage electrodes was almost zero, which was indicative of the low energy efficiency of the process. The voltage polarity was insignificant.

In the search for optimum regimes, it was established that adding several drops of tap water resulted in the formation of a stable volume discharge in the cavitation zone, which could stably operate for several minutes, and in the passage of a current between electrodes (determined by the interelectrode distance and reaching 1 mA). Adding distilled water only led to the initiation of separate breakdowns, rather than to a stable discharge. Evidently, the main role in the discharge initiation was played by the impurities of electrolytes present in water. It was established that neither the type nor the concentration (exceeding a certain threshold) were significant for the discharge process. Therefore, it was expedient to use dilute solutions of readily available compounds such as NaCl. The discharge stability and the cavitation cloud size could be controlled by the level of supplied power. The process was also strongly dependent on the efficiency of cooling the reactor cell: excess heating of the reactor led to boiling of the medium and breakdown of the stable discharge.

It was found that the above action upon *n*-octane and *n*-decane at atmospheric pressure and an initial temperature of 20°C led to the formation of 1.5–2% of unsaturated hydrocarbons (mostly ethylene and 1-alkenes) and aromatic compounds (mostly benzene) over a time period of 10 min. The efficiency can be readily estimated from the ratio of supplied acoustic ($P_A \le 30$ W) and electric ($P_E \le 20$ W) power to the energy spent for breaking C–C bonds (determined by the mass of hydrocarbons subjected to cracking). For example, the initial mass of *n*-octane (C_8H_{18}) was 20 g; the mass of alkane subjected to thermal cracking was 0.4 g (2% of the initial amount) or 3.5×10^{-3} mol (2.1×10^{21} *n*-octane molecules). Assuming that only one C–C bond is broken in each molecule, we determine the total energy spent for the bond breakage $E_D = 7.6 \times 10^{21}$ eV (1216 J). The total energy consumption for 10 min was $E_S = 30000$ J and, hence, the energy efficiency is $\eta = E_D/E_S \approx 4\%$. Obviously, this is by no means a limiting value, and the process efficiency can be further increased.

The observed degradation rate significantly exceeded the values reported in [11]. The process

required neither preliminary saturation of the initial hydrocarbon with xenon (better) or air (worse) nor constant supply of these gases (which was a necessary condition in [11]).

Thus, we have found an effective means of driving the electric energy to the breakage of covalent bonds in hydrocarbons by processing hydrocarbons in a cavitation zone in the presence of electric field. Evidently, an electric discharge generated inside a cavitation bubble leads to the formation of free radicals (or radical ions), which are transferred to the liquid phase upon collapse of the bubble and either participate in the degradation reactions or initiate chain reactions. On the whole, the process yields several degradation product, low-molecular-mass compounds (including aromatics). Neither the cavitation, nor the presence of electric field, nor even their combination are effective without activation of the process by adding an aqueous electrolyte solution, which is necessary to make the degradation process sufficiently effective.

Acknowledgments. This study was initiated and supported by "Interbiznesproekt" Company (Barnaul, Russia).

REFERENCES

1. L. I. Pishchenko and N. G. Klimnik, USSR Inventor's Certificate No. 1748336 A2, cl. B01F 5/00 (1990).
2. A. F. Kladov, US Patent No. 3385287, cl. 126–247 (1969); USSR Patent No. 1329629, cl. F24J 3/00 (1982); SU Patent No. 1656980 A1.
3. Yu. S. Patapov, USSR Inventor's Certificate No. 458591, cl. F25B 29/00 (1972); RU Patent No. 2045715C1, cl. 6F25B 29/00.
4. A. F. Kladov, CCCH RU Patent No. 2078116C1, cl. 6C10G 15/00, 15/08 (1997).
5. A. K. Kurochkin, R. N. Gimaev, R. B. Valitov, *et al.*, USSR Inventor's Certificate No. 1377281 A1, cl. C10G 7/06 (1984).
6. V. N. Kirilenko, S. O. Brulev, and V. V. Ivanov, Patent Appl. No. 2000100 235/04 (Russia).
7. V. N. Kirilenko, S. O. Brulev, A. S. Besov, and K. Yu. Koltunov, RF Patent No. 2186825 (2002).
8. A. V. Kravtsov and É. D. Ivanchina, *Computer Prognosis and Optimization of Fuel Production. Physicochemical Principles and Technology* (STT, Tomsk, 2000).
9. V. F. Nazimok, V. I. Ovchinnikov, and V. M. Potekhin, *Liquid-Phase Oxidation of Alkylaromatic Hydrocarbons* (Khimiya, Moscow, 1987).
10. K. Hauskroft and E. Constebl, *General Chemistry* (Mir, Moscow, 2002).
11. I. I. Golubnichiĭ, V. D. Goncharov, and Kh. V. Protopopov, Khim. Vys. Énerg. **3** (6), 515 (1969).

Translated by P. Pozdeev

Technical Physics Letters, Vol. 29, No. 3, 2003, pp. 210–213. Translated from Pis'ma v Zhurnal Tekhnicheskoĭ Fiziki, Vol. 29, No. 5, 2003, pp. 78–86.

Relaxation of Optical Excitations in Crystals of the Y_2O_3–Al_2O_3 System with Radiation Defects

M. A. Mussaeva, A. A. Gafarov, and E. M. Ibragimova

Institute of Nuclear Physics, Academy of Sciences of the Republic of Uzbekistan, Tashkent, Uzbekistan
e-mail: muhtar@suninp.tashkent.su

Received September 9, 2002

Abstract—The photoluminescence and short-time persistence (afterglow) kinetics in pure and doped Y_2O_3–Al_2O_3 crystals excited with UV laser pulses (12 ns, 337 nm) were studied using samples irradiated with gamma quanta from a ^{60}Co source to a dose from 10^4 to 10^7 Gy. The relaxation time of the samples studied increases, with decreasing symmetry of the crystal lattice, in the following order: garnet—orthoaluminate—ruby—yttria. The afterglow duration and intensity significantly decrease in gamma-irradiated crystals, which is explained by the predominant recombination of close electron–hole pairs. Garnet–neodymium crystals are characterized by high radiation stability and fast relaxation kinetics. © *2003 MAIK "Nauka/Interperiodica".*

Introduction. Crystals of the Y_2O_3–Al_2O_3 system with impurities of transition metal ions and rare earth elements are widely used in high-power laser elements, scintillators, and phosphors. Prolonged operation of UV-pumped lasers leads to the formation of structural defects (color centers) related to some ambivalent impurities of transition metals, which detrimentally influence the kinetics and quantum yield of photoluminescence (PL) and decrease the lasing parameters. Recently, Antipov *et al.* [1] theoretically studied the dynamics of changes in the refractive index of a Nd:YAG laser crystal using Nd^{3+} ion excitation. These changes are related to the kinetics of relaxation of the electron excitations, including the formation of unstable structural defects. On the other hand, the results of spectroscopic investigations [2] showed that $YAlO_3$ crystals containing an ambivalent impurity of Mn, which are also capable of forming color centers under UV excitation [3], can be successfully employed in optical data recording and storage systems.

The decay of electron excitations with the defect formation, together with the slow persistent component of scintillators and phosphors, are the main factors hindering their use [4, 5]. Therefore, there is a need to study the PL and short-time persistence (afterglow, AG) components in irradiated crystals of the system under consideration, in addition to the available detailed spectroscopic data [3–9]. In addition to the luminescence from Nd^{3+} in a crystal of $Y_3Al_5O_{12}$:Nd, there is emission at 317 nm for 0.5 μs, related to the decay of an autolocalized O_2^{3-} exciton at $T < 150$ K, and emission from impurities at 300 K with a 10 μs delay [6, 7]. In the presence of neutron- and/or gamma-induced defects, there appeared a broadband emission in the region of 300–400 nm with a weak component at 500 nm [3]. A pulsed electron beam excited cathodoluminescence in the same spectral region with a relaxation time below 1 μs, which is indicative of the exciton character [8, 9]. However, it is still unclear how and why the time of relaxation of the optical excitations changes in the course of accumulation of the radiation-induced structural defects.

In this context, we have studied the PL kinetics of laser crystals of the Y_2O_3–Al_2O_3 system with a variable degree of defectness determined by preliminary irradiation.

Experimental. We measured the time variation of the PL and AG intensity (in millivolts) for the pulsed UV excitation of α-Al_2O_3, Y_2O_3, $Y_3Al_5O_{12}$, and $YAlO_3$ crystals, both pure and doped with Cr and Nd, before and after exposure to gamma-radiation from a ^{60}Co source to a dose from 10^4 to 10^7 Gy at a temperature varying from 300 to 350 K as a result of the radiation heating. The luminescence was excited by a pulsed nitrogen laser operating at 337 nm, with a pulse duration of 12 μs and a repetition frequency of 25 Hz. This selection was explained by the laser radiation wavelength falling within the range of excitation of the optically active Cr and Nd impurities and the range of optical absorption of the radiation-induced defect centers (F^+, O^-) (i.e., in the vicinity of impurity excitons that can participate in the energy transfer [3, 6–9]). This is not accompanied by the electron–hole pair production, since the quantum energy is smaller than the interband transition energy (bandgap E_g). The optical emission was detected with the aid of a fast-response (5 μs) FEU-30 photomultiplier and a C7-8 digital oscillograph.

Experimental results. Figure 1a shows the typical optical response of an α-Al_2O_3 crystal (leukosapphire

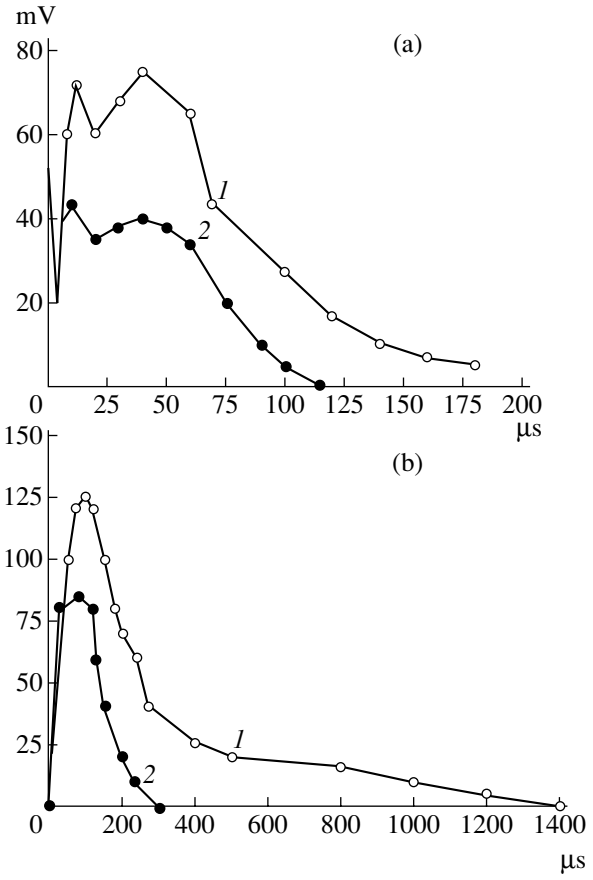

Fig. 1. PL kinetics for the laser excitation at 337 nm (300 K): (*1*) before irradiation; (*2*) after gamma irradiation; (a) α-Al_2O_3–Cr^{3+} (dose, 10^6 Gy); (b) α-Al_2O_3 crystal with a rough surface (dose, 10^4 Gy).

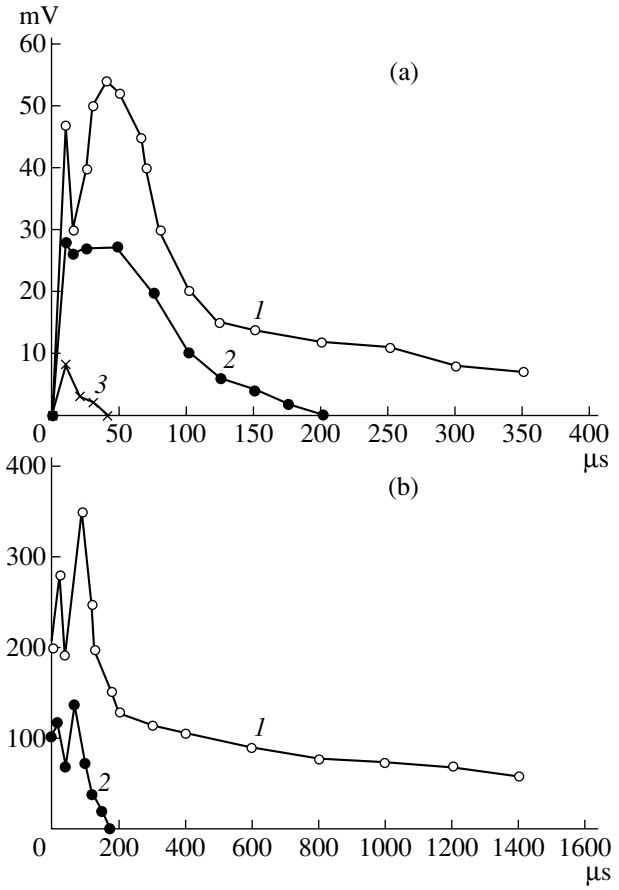

Fig. 2. PL kinetics for the laser excitation at 337 nm (300 K): (*1*) before irradiation; (*2*) after gamma irradiation; (*3*) after neutron irradiation (10^{18} cm^{-2}); (a) Y_2O_3 (gamma radiation dose, 10^7 Gy); (b) Y_2O_3–Nd^{3+} (dose, 10^5 Gy).

with a small content of Cr) excited with an UV pulse. The signal contains an intense fast component (3 μs) and a weak slow component (0.2–0.7 ms), which depends on the presence of Cr or other impurities. Irradiation with gamma quanta to a dose of 10^4–10^5 Gy shortens the slow component by half, whereby the signal intensity (integral photoresponse) significantly increases. The irradiated crystal does not re-radiate the absorbed UV pulses and produces PL due to the excitation of radiation-induced emission centers. Large doses (10^6–10^7 Gy) reduce the response intensity by half and shorten the AG duration to 50 μs.

Figure 1b shows the photoresponse of a sample of α-Al_2O_3 with a rough defective surface. This sample was studied in order to reveal the contribution from the surface defects (dangling bonds) on which the electron excitations localize and decay [4]. As can be seen, the PL kinetics have a significant slow component with a maximum at 100 μs and a decay to 1.4 ms. After gamma irradiation even to a moderate dose (10^4 Gy), the decay time significantly shortens (to 300 μs), although the AG maximum decreased only by one-third. Therefore, the radiation-induced emission centers possess a shorter lifetime due to the recombination of carriers released from close electron and hole traps.

Figure 2a presents the PL kinetics of a pure Y_2O_3 crystal before and after gamma and neutron irradiation. Similar to the case of Al_2O_3, the response of Y_2O_3 also has a fast component (2 μs, not resolved in the figure), slower components (10 and 50 μs), and a residual decay (to ~1 ms). As can be seen, gamma irradiation to a high dose (10^7 Gy) decreases the AG peak amplitude by half and reduces its duration to 200 μs. After prolonged neutron irradiation, the AG signal is weak (Fig. 2a).

Figure 2b shows the PL kinetics of the Y_2O_3–Nd^{3+} crystal before and after gamma irradiation. In addition to the component at 50 μs (similar to that in the pure crystal, cf. Fig. 2a), there is an intense PL peak with a 150 μs delay and a long AG component (on the order of a few milliseconds). After the gamma irradiation to 10^5 Gy, the photoresponse significantly decreases and shortens to 180 μs.

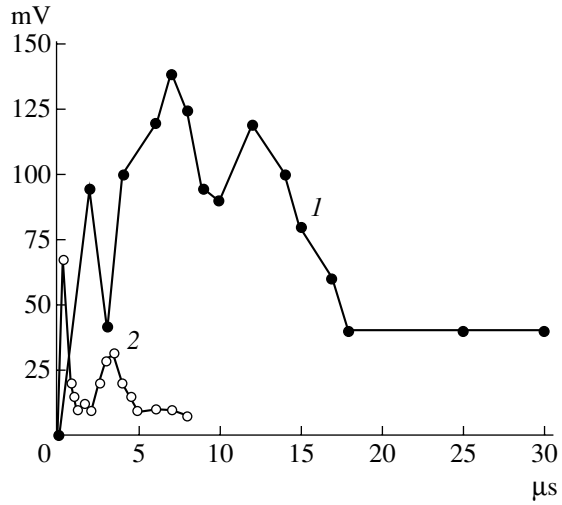

Fig. 3. PL kinetics in $3Y_2O_3{:}5Al_2O_3{-}Nd^{3+}$ (garnet) for the laser excitation at 337 nm (300 K): (*1*) before irradiation; (*2*) after gamma irradiation to a dose of 10^6 Gy.

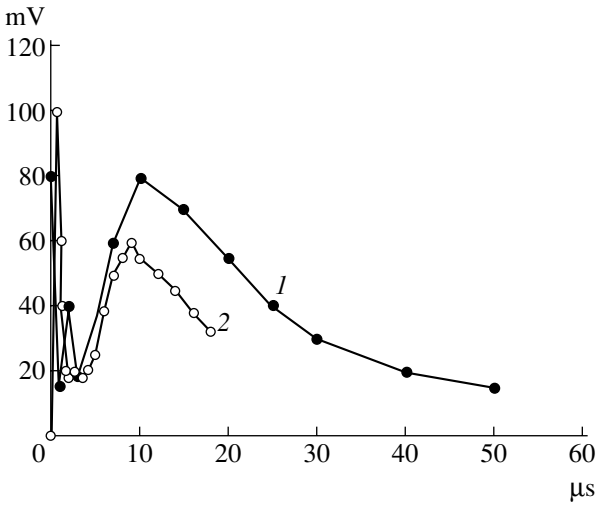

Fig. 4. PL kinetics in $Y_2O_3{:}Al_2O_3{-}Nd^{3+}$ (orthoaluminate) for the laser excitation at 337 nm (300 K): (*1*) before irradiation; (*2*) after gamma irradiation to a dose of 10^6 Gy.

A pure crystal of $Y_3Al_5O_{12}$ (garnet) exhibits 38-ns relaxation after excitation with a UV pulse, irrespective of the dose of preliminary irradiation. A laser element made of $Y_3Al_5O_{12}$:Nd emits the absorbed energy of a pumping pulse within 5 μs and exhibits a short AG component (Fig. 3). After gamma irradiation to a dose of 10^6 Gy, the PL intensity grows (see the AG peaks delayed by 2, 5, 7, and 12 μs) and exhibits complete relaxation within 0.1 ms. A slow weak AG component delayed by 20 μs reflects participation of the Nd^{3+} ions (transferring excitation energy from one to another) in the luminescence. These results partly agree with the data recently reported in [1], where a weak inertialess component was accompanied by enhancement of the peak delayed by 3 μs caused by population (or depopulation) of a high-lying level $^2(F2)_{5/2}$ on the 4*f* shell of Nd^{3+} ions possessing high polarizability in the visible and near IR range.

The behavior of PL and AG signals in $YAlO_3$:Nd (orthoaluminate) before and after gamma irradiation is depicted in Fig. 4. A fast PL component is delayed by 0.7 μs and followed by a peak at 10 μs. After the exposure to a dose of 10^6 Gy, the first peak was decreased and delayed by 3 μs; the second peak at 10 μs somewhat increased in amplitude and in duration (100 μs). In addition, there is an intense photoannealing of the radiation-induced color centers, which confirms the data concerning the photosensitivity of orthoaluminates [2, 3]. Note that neither leukosapphire nor pure garnet exhibit coloration under such irradiation and are considered as radiation-stable materials [3, 7–9]. The longer AG kinetics in orthoaluminate as compared to those in garnet is probably related to a stronger crystal field at the octahedral lattice site as compared to the dodecahedral environment [3, 6].

As can be seen from the figures, the relaxation kinetics in the laser crystal system under consideration increases in the following order: garnet—orthoaluminate—ruby—yttria with decreasing crystal lattice symmetry. As demonstrated previously [3, 6–9], thermal annealing of the optically active centers induced by the gamma irradiation at 300–350 K in leukosapphire, garnet, and orthoaluminate takes place at 400 K.

Discussion. Thus, a general feature of the crystals of three types studied is the presence of a fast (40 ns) exciton component in response to a UV excitation pulse. This component is probably related to a free exciton in the oxygen sublattice O* in the AlO_4 tetrahedron. Excitons near the intrinsic or impurity defects decay via the radiative relaxation channel within a few microseconds. The impurities of Cr and Nd are responsible for a slow emission component, since the radiative transitions proceed from long-lived excited electron states near the impurity ions. The observed decrease in the duration of PL in crystals of the Y_2O_3–Al_2O_3 system after gamma irradiation is related to a fast exchange interaction between close pairs of radiation-induced intrinsic defects and impurity centers, the excited states of which possess virtually equal energies. The radiation-induced structural defect decreases the first fast component (40 ns) in the optical response related to the radiative relaxation (decay) of the free excitons O* (which, being scattered on the radiation defects decay nonradiatively into electron and hole). The energy obtained from excitons increases the following response component (within a few microseconds) caused by the radiative recombination of excitons on the close pair defects (O^- and F^+) in the oxygen sublattice. In the presence of impurities, either O^- or F^+ localize at these centers depending on their ion radii. The transfer of optical excitations and the radiative relaxation (including optical transitions in the inner shells of rare earth (Nd^{3+}) ions or transition metals (Cr^+)) pro-

ceeds at a much lower rate (up to within milliseconds). Thus, the localization can be avoided by introducing impurities luminescent in the region of the bands of the radiation-induced absorption and leading to the "radiation annealing of color centers" (F^+, O^-) capable of participating in the energy transfer process (as in the case of $Y_3Al_5O_{12}$:Nd and $YAlO_3$:Nd). This provides for the radiation stability of materials.

Conclusion. The above results allow us to recommend leukosapphire, garnet, and orthoaluminate with neodymium impurity for long-term operation under the conditions of ionizing radiation to a total dose of 10^6 Gy. The observed decrease in the AG duration after the gamma irradiation of Y_2O_3–Al_2O_3 is caused by the interaction of close pairs of radiation-induced defects.

REFERENCES

1. O. L. Antipov, A. S. Kuzhelev, D. V. Chausov, *et al.*, J. Opt. Soc. Am. B **16**, 1072 (1999).
2. M. A. Noginov, N. Noginova, M. Curley, *et al.*, J. Opt. Soc. Am. B **15**, 1463 (1998).
3. Sh. A. Vakhidov, B. Esemuratov, É. M. Ibragimova, and A. F. Rakov, in *Radiation Phenomena in Optical Materials* (Fan, Tashkent, 1978).
4. Ch. B. Lushchik and A. Ch. Lushchik, *Decay of Electron Excitations with the Formation of Defects in Solids* (Nauka, Moscow, 1989).
5. A. Lempicki, A. J. Wojtowicz, and E. Berman, Nucl. Instrum. Methods Phys. Res. A **333**, 304 (1993).
6. D. J. Robbins, B. Cockane, B. Lent, *et al.*, Phys. Rev. B **19**, 1254 (1979).
7. Sh. A. Vakhidov, E. M. Ibragimova, I. Nuritdinov, *et al.*, Phys. Status Solidi B **106**, 31 (1981).
8. Sh. A. Vakhidov and A. F. Rakov, Phys. Status Solidi A **80** (2), K175 (1983).
9. A. F. Rakov, Phys. Status Solidi A **96**, K169 (1986).

Translated by P. Pozdeev

Technical Physics Letters, Vol. 29, No. 3, 2003, pp. 214–217. Translated from Pis'ma v Zhurnal Tekhnicheskoĭ Fiziki, Vol. 29, No. 5, 2003, pp. 87–94.

Modeling Impurity Transfer to Tokamak Plasma

E. G. Kaveeva, A. H. Bekheit, S. P. Voskoboynikov, V. A. Rozhansky, D. Coster, X. Bonnin, and R. Schneider

St. Petersburg State Polytechnical University, St. Petersburg, Russia
Max Planck Institute for Plasma Physics, D-85748 Garching, Germany
Max Planck Institute for Plasma Physics, D-17491 Greifsvald, Germany

Received September 17, 2002

Abstract—Mechanisms of the impurity transfer inside a tokamak separatrix have been studied. It is shown that poloidal rotation significantly influences the poloidal distribution of impurities. An analysis of the neoclassical component of the radial impurity flux showed that this fraction is described by an expression that is more complicated than the standard neoclassical variant. © *2003 MAIK "Nauka/Interperiodica".*

Description of the transfer of impurities in tokamaks is among the most important problems encountered on the way to a controlled thermonuclear reactor. The impurities are sputtered from material surfaces exposed to a hot plasma, reach a separatrix (the last closed magnetic surface), and penetrate into the central part of the plasma filament, thus giving rise to the radiative energy losses. The radial transfer of impurities inside the plasma filament has been extensively studied. At the same time, the impurity fluxes (determining the impurity concentration inside the setup) near the separatrix are essentially two-dimensional (2D). In recent years, there appeared the possibility of studying the process of impurity transfer using the 2D numerical code B2SOLPS5.0 [1], which includes all phenomena related to self-consistent electric fields. For example, such a modeling elucidated mechanisms responsible for the impurity transfer from material surfaces to separatrix [2].

This paper addresses the mechanisms of impurity transfer inside the tokamak separatrix. The results of numerical modeling performed using the code B2SOLPS5.0 for the ASDEX Upgrade (AUG) tokamak are compared to the results of analytical calculation of the impurity transfer inside the plasma filament. It is established that the poloidal rotation significantly influences the poloidal impurity distribution [3, 4], which is at variance with the notions of the standard neoclassical theory [5, 6]. We have analyzed the neoclassical component of the radial flux of impurities and shown that the neoclassical part of the radial flux is described by a more complicated expression than that obtained within the framework of the standard neoclassical approach. The corresponding flux is intermediate between those calculated in [3] and [5]. As can be seen from the calculation, the average concentration of impurities near the separatrix in the *L* regime is determined by the ionization of the neutral impurity atoms above the *X* point, the poloidal plasma rotation, and the radial anomalous diffusion. The neoclassical radial impurity flux is small compared to the anomalous diffusion flux. At the same time, should the anomalous flux be suppressed (e.g., inside the transport barrier), the neoclassical radial flux can play an important role in the formation of a radial profile of the impurity concentration.

The characteristic parameters of modeling correspond to the *L* regime of AUG: plasma current I = 1 MA; toroidal magnetic field B = 2 T; concentration and temperature of the main (deuterium) plasma ions in the region a–r = 1 cm on the outer contour is $n_i = 2 \times 10^{19} - 2.7 \times 10^{19}$ m^{-3} and T_i = 40–80 eV, respectively. The magnetic field is oriented along the normal (toroidal ion drift directed toward the *X* point). The model impurity is carbon. The source of the impurity is characterized by the sputtering yield γ = 1–3%. We have performed several calculations with the electric and diamagnetic drift components switched on and off in order to elucidate the role of these factors in the impurity distribution.

With these parameters, a significant fraction of neutral carbon atoms penetrates up to the level of the *X* point. Outside the separatrix, the impurity is ionized to C^{1+}–C^{3+} and effectively entrained with the main ions toward the diverter plates. The effect of a thermal force directed away from the plates is manifested by a small difference in velocities between the impurity and the main ion component. The impurity concentration distribution is determined by the source (through ionization of the lower charged states and C^{4+} recombination) and by the velocity of the main ions [2].

Inside the separatrix, the main ionization states are C^{4+}–C^{5+}. The source of C^{4+} ions is situated in the vicinity of the *X* point (on a lower part of the magnetic surface). In the absence of drift, a maximum impurity concentration takes place at the same site. The width of this maximum is determined by the radial and longitudinal diffusion and by the source (neutral carbon) distribution. After switching on the drift, the impurity becomes

1063-7850/03/2903-0214$24.00

more homogeneously distributed with respect to the poloidal angle. In some cases, a new concentration maximum appears in the upper part of the magnetic surface or inside the internal sample (Figs. 1, 2).

The impurity transfer in the vicinity of the separatrix can be analytically calculated provided that

$$\max\left(\frac{D_{I\|}b_\theta^2}{r^2}, \frac{T_i}{eBr}\frac{1}{L_i}(1+k_T\eta_i)\right) \gg \frac{D_{I\perp}}{L_I^2}, \quad (1)$$

where $D_{I\|} = \dfrac{T_i}{CZ^2\sqrt{2}m_i\nu_i}$ is the coefficient of longitudinal diffusion for the impurities possessing charge Z relative to the main ions; $D_{I\perp}$ is the coefficient of anomalous radial diffusion of impurities; r and R are the small and large radii of the tokamak, respectively; $L_{I,i}$ are the characteristic radial scales of the concentration of impurities and the main ions, $b_\theta = B_\theta/B$ is the ratio of the poloidal and toroidal magnetic fields; $\eta_i = d\ln(T_i)/d\ln(n_i)$. The other notations are as follows: ν_i is the collisional frequency of the main ions; k_T is the coefficient in a neoclassical expression for the radial electric field [4] (in the Pfirsch–Schluter regime, $k_T = 2.7$); $E^{(NEO)} = \dfrac{T_i}{e}\left(\dfrac{d\ln n_i}{dr} + k_T\dfrac{d\ln T_i}{dr}\right) - b_\theta\langle V_\| B\rangle$; C is the coefficient in the friction force acting upon all impurity ions; $R_{I\|} = CZ^2\sqrt{2}\,n_I m_i\nu_i(V_{i\|} - V_{I\|})$; $\tilde{\alpha} = \dfrac{(Z^2-Z)\alpha - 1 + ZT_e/(T_e+T_i)}{Z^2C}$; α is the coefficient in the thermal force $R_{I\|}^T = \alpha(Z^2-Z)b_\theta n_I\dfrac{\partial T_i}{r\partial\theta}$. Subscripts I and i refer to the impurity and the main ion component. The main and the impurity ions are assumed to possess the same temperature. For the sake of simplicity, we will consider the approximation of a round tokamak with a large aspect ratio. In addition, we assume that the impurity source S_I does not significantly influence the poloidal concentration distribution:

$$\frac{T_i}{eBR}\frac{1}{L_i}(1+k_T\eta_i) \gg \frac{D_{I\perp}}{L_I^2}. \quad (2)$$

Condition (1) indicates that the impurity concentration exhibits leveling over the magnetic surface due to the longitudinal diffusion or poloidal rotation. The average concentration is determined predominantly by the anomalous radial diffusion and can be determined from the equation

$$-\frac{\partial}{\partial r}\left(2\pi eD_{I\perp}\frac{\partial\langle n_I T_i\rangle}{\partial r}\right) = \int_0^{2\pi} r\left(1+\frac{r}{R}\cos\theta\right)S_I d\theta. \quad (3)$$

A perturbation of the impurity concentration depending on the poloidal angle is small. The character of the solution depends on the parameter

$$A = CZ^2\sqrt{2}\frac{1}{b_\theta^2}\frac{\nu_i}{\omega_{ci}}r\left|\frac{\partial\ln(n_i)}{\partial r} + k_T\frac{\partial\ln(T_i)}{\partial r}\right| \approx CZ^2\sqrt{2}\frac{r}{L_i}\frac{1}{b_\theta^2}\frac{\nu_i}{\omega_{ci}}(1+k_T\eta_i). \quad (4)$$

Here and below, the radial derivatives imply that the values of n_i, n_I, and T_i are averaged over the magnetic surface. By solving the longitudinal force balance equation and the continuity equation for the impurity ions, we obtain an expression for the poloidal concentration distribution:

$$n_I = \langle n_I\rangle\left[1 + \frac{r}{R}\frac{2A}{\sqrt{1+A^2}}\frac{1+(1-0.45\tilde{\alpha})\eta_i}{1+k_T\eta_i}\sin(\theta-\phi)\right], \quad (5)$$

where $\phi = \arctan(A)$ and the angle θ is measured counterclockwise from the outer contour.

According to the neoclassical theory, the average radial impurity flux through the magnetic surface can be determined by averaging the toroidal component of the force balance:

$$0 \approx n_I V_{Ir}B_x + CZ^2\sqrt{2}n_I m_i\nu_i(V_{i\|} - V_{I\|}) + R_{I\|}^T. \quad (6)$$

Here, we neglect the inertial term and ignore the difference between the longitudinal and poloidal components of the friction and thermal forces. By averaging Eq. (6) with a weight of R/B_x, we obtain the average flux of impurity:

$$\langle n_I V_{Ir}\rangle = -\frac{\oint\frac{2\pi R}{B_x}(CZ^2\sqrt{2}n_I m_i\nu_i(V_{i\|} - V_{I\|}) + R_\|^T)rd\theta}{\oint 2\pi Rrd\theta}. \quad (7)$$

The thermal force is determined by the temperature gradient of the main ions related to the Pfirsch–Schluter thermal fluxes:

$$\frac{\partial T_i}{\partial\theta} = 0.64\frac{\nu_i}{\omega_{ci}b_\theta^2}\frac{\partial T_i}{\partial r}\left(1 - \frac{B^2}{\langle B^2\rangle}\right). \quad (8)$$

The difference in velocities between the impurity and the main ions depends on the impurity perturbation

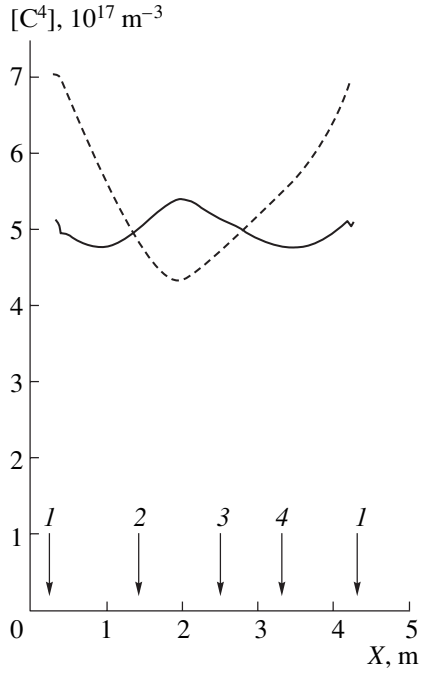

Fig. 1. Poloidal distribution of C^{4+} impurity in ASDEX-Upgrade tokamak calculated for $n_i = 2 \times 10^{19}$ m^{-3} and T_i = 80 eV in the region of $a–r$ = 1 cm on the outer contour. Solid and dashed curves correspond to the calculation with and without drift, respectively (poloidal coordinate is directed clockwise; length in meters corresponds approximately to $r\theta$ for a round tokamak): (*1*) *X*-point; (*2*) inner contour; (*3*) top; (*4*) outer contour.

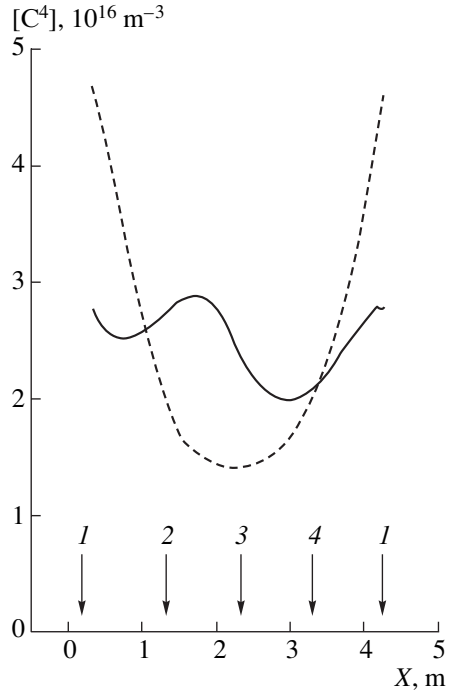

Fig. 2. Poloidal distribution of C^{4+} impurity in ASDEX-Upgrade tokamak calculated for $n_i = 2 \times 10^{19}$ m^{-3} and T_i = 40 eV in the region of $a–r$ = 1 cm on the outer contour. Solid and dashed curves correspond to the calculation with and without drift, respectively (poloidal coordinate is directed clockwise; length in meters corresponds approximately to $r\theta$ for a round tokamak). Positions *1–4* as in Fig. 1.

concentration and, hence, on the parameter A. The expression for the impurity flux is as follows:

$$\langle n_I V_{Ir} \rangle = \left(\frac{\partial \ln(n_i)}{\partial r} - \frac{1}{Z} \frac{\partial \ln(n_I)}{\partial r} \right.$$
$$\left. + \left(1 - 0.45\tilde{\alpha} - \frac{n_I}{Z n_i}\right) \frac{\partial \ln(T_i)}{\partial r} \right) q^2 \frac{\nu_i}{\omega_{ci}} C 2\sqrt{2} Z$$
$$\times \frac{1}{1 + A^2} \frac{n_I T_i}{eB} + \left(\frac{1}{A^2} + \frac{\eta_i (k_T - 1 + 0.45\tilde{\alpha})}{1 + k_T \eta_i} \right) \quad (9)$$
$$\times q^2 \frac{\nu_i}{\omega_{ci}} 1.28 \frac{T_e}{T_e + T_i} \frac{A^2}{1 + A^2} \frac{n_I T_i}{eB} \frac{\partial \ln(T_i)}{\partial r}.$$

Within the framework of the standard neoclassical description [5, 6], the difference in velocities is calculated assuming that the concentration perturbation on the magnetic surface is much smaller than the inverse aspect ratio. In our case, this corresponds to $A \ll 1$. The impurity concentration perturbation is distributed as $\sin\theta$, with a maximum occurring in the upper part of the system. The difference in velocities between the impurity and the main ions is described by a formula [5, 6] in which the impurity diffusion can provide for a large contribution. In expression (9), the first term dominates, being Z times as large as the second term.

In the case of $A \gg 1$, the longitudinal diffusion of impurity is relatively small and can be ignored. The concentration perturbation exhibits a maximum on the inner or outer contour. This perturbation has to be taken into account in calculating the difference of velocities. The first term in expression (9) becomes small, and the impurity transfer is determined by the second term. This limiting case was studied in [3, 4].

In the intermediate case of $A \approx 1$, the concentration maximum is observed in an intermediate position. In expression (9), the first and second terms are comparable in magnitude.

If the inequality (1) fails to be valid, the concentration profile exhibits peaks at the source and rapidly falls down with increasing distance. The average concentration depends on the characteristic poloidal diffusion lengths $L_D \approx L_I \sqrt{D_{I\parallel} b_\theta^2 / D_{I\perp}}$, poloidal drift $L_d \approx T_i(1 + k_T \eta_i) L_I^2 / D_{I\perp} e B L_i$, and the impurity source L_s. If the maximum of these values is smaller than the poloidal

length of the magnetic surface, the concentration can be estimated as

$$n_I \sim \frac{\langle S \rangle L_s L_I^2}{D_{I\perp} \max\{L_s, L_d, L_D\}}. \quad (10)$$

In our model, condition (1) was well satisfied for $T_i = 80$ eV. Even in the absence of a drift, the concentration of C^{4+} is not significantly perturbed (Fig. 1). An intermediate position of the maximum in the presence of drift corresponds to the case of $A \approx 1$, while the additional concentration maximum near the X point is determined by the ionization source.

For the calculations with $T_i = 40$ eV, the characteristic lengths are $L_D \approx 1$ m, $L_s \approx 1.2$ m, and $L_d \approx 2$–5 m, while the magnetic surface length is 4 m. Therefore, in the absence of drift, the concentration is inhomogeneous, while the inclusion of drift leads to a significant leveling (Fig. 2).

It should be noted that, in the presence of an anomalous transfer, the neoclassical effects play no significant role. Indeed, in the modeling of the L regime of the ASDEX-Upgrade tokamak, the neoclassical radial flux of impurity has proved to be smaller than the anomalous flux by one order of magnitude. At the same time, the influence of the neoclassical mechanisms on the impurity accumulation in the H regime can be quite significant.

Acknowledgments. This study was supported by the INTAS Foundation (grant no. 457), the Russian Foundation for Basic Research (project no. 00-02-16670), and the Russian Foundation for Basic Research of Young Scientists (project no. 02-02-06054).

REFERENCES

1. V. Rozhansky, S. Voskoboynikov, E. Kaveeva, *et al.*, Nucl. Fusion **41**, 387 (2001).
2. V. Rozhansky, E. Kaveeva, S. Voskoboynikov, *et al.*, J. Nucl. Mater. (2002) (in press).
3. V. A. Rozhansky and L. D. Tsendin, Fiz. Plazmy **5**, 771 (1979).
4. V. Rozhansky and M. Tendler, in *Reviews of Plasma Physics*, Ed. by B. B. Kadomtsev (Consultants Bureau, New York, 1996), Vol. 19, p. 147.
5. P. H. Rutherford, Phys. Fluids **17**, 1787 (1974).
6. S. P. Hirshman and D. J. Sigmar, Nucl. Fusion **21**, 1079 (1981).

Translated by P. Pozdeev

Technical Physics Letters, Vol. 29, No. 3, 2003, pp. 218–220. Translated from Pis'ma v Zhurnal Tekhnicheskoĭ Fiziki, Vol. 29, No. 6, 2003, pp. 1–6.

Interaction of Dispersed Water with Flame

Yu. V. Alekhanov, M. V. Bliznetsov, Yu. A. Vlasov, V. I. Dudin, A. E. Levushov, A. I. Logvinov, S. A. Lomtev, and E. E. Meshkov

Institute of Experimental Physics, Russian Federal Nuclear Center, Sarov, Russia

Sarov Physicotechnical Institute, Sarov, Russia

e-mail: root@gdd.vniief.ru

Received August 28, 2002

Abstract—The electric explosion of a wire in a thin-walled cylindrical glass ampule filled with water results in the formation of a disperse water (DW) cloud having a ring shape, which expands rapidly in the radial direction and slowly in the axial direction. Interaction of the DW with a flame produces fire quenching in the interaction zone. Experimental results are used for estimating the requirements and consumptions for creating DW clouds capable of quenching large-scale fires. © *2003 MAIK "Nauka/Interperiodica".*

In recent years, there has been extensive development in the technology of extinguishing fires (including large-scale ones) using sprayed or dispersed water (DW) clouds consisting of drops with dimensions on the order of 100 μm and below [1–4]. In this context, it was of interest to elucidate the physical processes underlying the flame quenching effect according to this technology.

A DW cloud was created by electric explosion [5, 6] of a wire in a thin-walled (0.5 mm) cylindrical glass ampule with an outer diameter of 16 mm, filled with water (V = 1.6 cm^3) and closed at the edges with 0.5-mm-thick foil plates. The nichrome wire (0.05 mm in diameter) arranged on the ampule axis exploded under the action of a current pulse from an 0.25 μF capacitor bank charged to 15 kV.

Figure 1 presents photochronograms (made with a camera of the SFR type) illustrating the DW cloud expansion upon explosion of the ampule. The DW expansion was monitored both along the axis (Fig. 1a) and in the perpendicular direction (Fig. 1b). As can be seen from the images, the DW cloud has the shape of a ring. In all cases, the ring expanded rapidly in the radial direction and slowly in the axial direction. The expanding ring surface features strong perturbations that grow with time and eventually (at $t \approx 2$ ms) lead to the decay of the ring into separate fragments. This can be related to the development of the Rayleigh–Taylor instability [7].

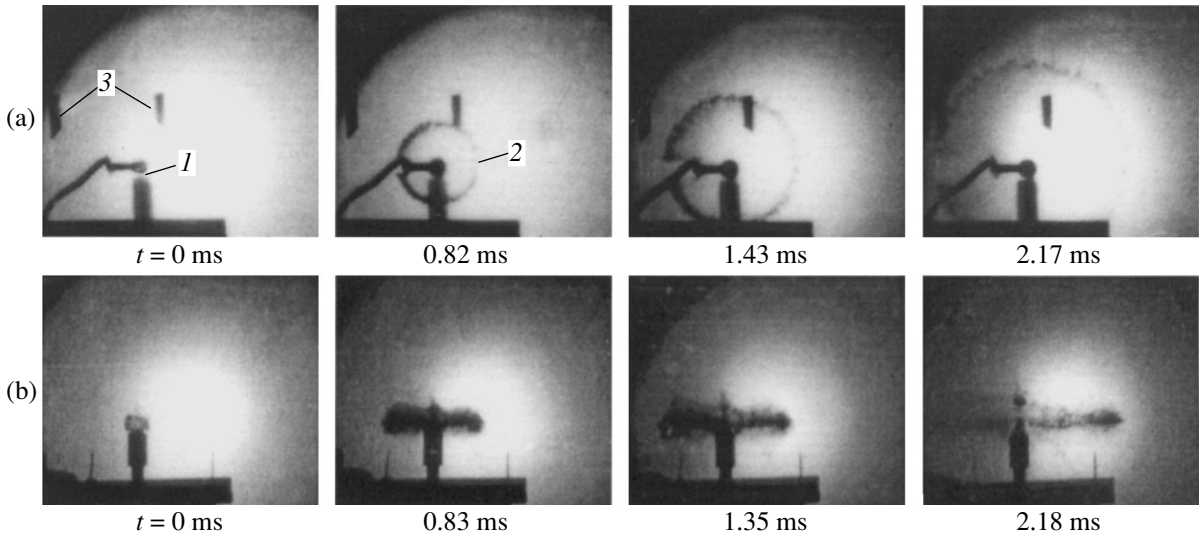

Fig. 1. Photochronograms showing expansion of a dispersed water cloud upon electric explosion in a cylindrical ampule with water: (*1*) ampule; (*2*) dispersed water front; (*3*) marker elements. The camera was viewing (a) along the ampule and (b) in the perpendicular direction. The time t is measured from the instant of explosion.

1063-7850/03/2903-0218$24.00 © 2003 MAIK "Nauka/Interperiodica"

According to the *R–t* diagram, the initial DW ring expansion velocity is $v_0 = 64$ m/s. Since water expands as a thin ring, the velocities of all elements in the ring are virtually the same, and we can estimate the kinetic energy of the expanding cloud as $E \approx m v_0^2/2$, which yields $E \approx 3.3$ J. Accordingly, the energy density can be evaluated as $e = E/m \approx v_0^2/2$, which yields $e \approx 2$ J/g. Using prints on paper situated at various distances from an ampule filled with ink, it was established that the liquid is dispersed into drops with dimensions below 250 μm.

Figure 2 shows a sequence of shots made with a video camera (operated at 25 pic/s), illustrating the interaction of an expanding DW cloud with a flame. The ampule with water was situated at a distance of R = 21 cm from a metal screen having the shape of a half-cylinder. Mounted on the inner surface of the screen was a strip of cardboard bearing a piece of filter paper ($\sim 42 \times 5$ cm). The paper was impregnated with acetone (~ 1 cm^3) and set on fire. In a few seconds, the ampule exploded, and the DW interaction with the flame was monitored.

When the expanding DW cloud reaches the flame, the water drops exhibit intensive heating and evaporation, thus absorbing heat from the flame. In the region of interaction, the reaction of combustion completely ceases as a result of the temperature drop. In the upper part of the flame, not accessible to the DW cloud, the flame is retained until complete burning of acetone vapor.

Evidently, the efficacy of the flame quenching by a DW aerosol is determined by the water access to the region where the burning of evaporated acetone vapor is initiated. Rapid cooling of this region leads to a sharp drop in the reaction rate, retards acetone evaporation, and breaks the connection with the heated flame regions. As a result, the following fire-extinguishing mechanisms are operative:

(i) dilution of the reacting components with water vapor;

(ii) cooling of the burning substance as a result of water evaporation;

(iii) isolation of reacting substances (diluted with water vapor, a cooled mixture of the reaction products, air, and acetone vapor serves as a barrier between flame and acetone-impregnated paper, which hinders further evaporation of acetone and ignition of the vapor).

We have performed a series of experiments in this arrangement, and, every time, the burning process was virtually instantaneously terminated.

Based on the results of these experiments, it is possible to make some rough estimates for the conditions ensuring flame quenching. The experimental pattern shows that the width of the flame quenching zone is approximately twice as large as the paper strip width

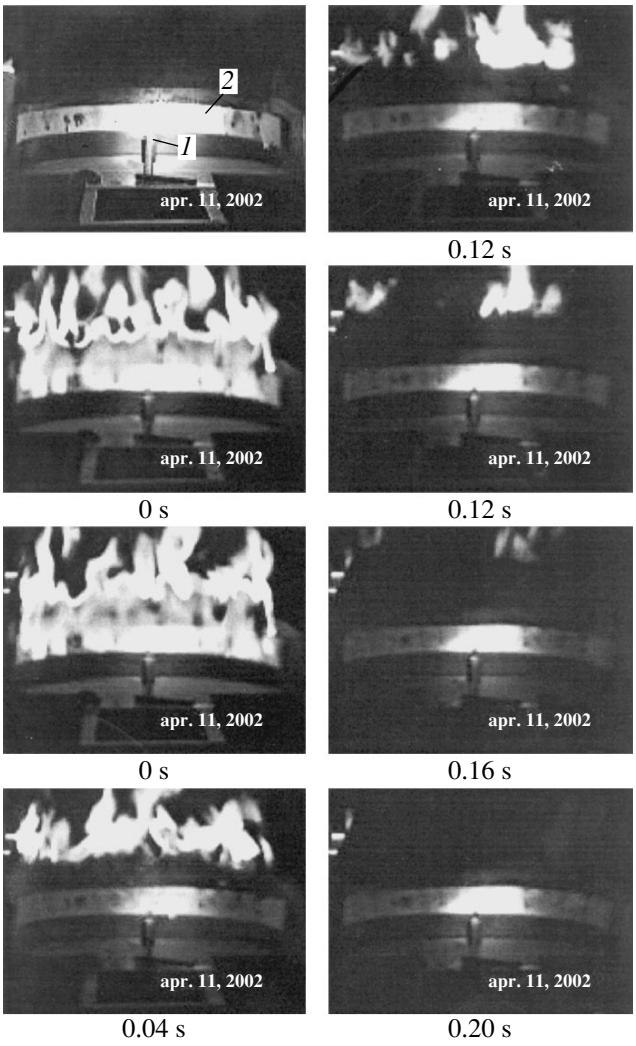

Fig. 2. Sequential shots illustrating quenching of the flame at a paper strip (impregnated with acetone) under the action of an expanding DW cloud. DW strikes the lower part of the flame, in which the ignition and initial burning stage of acetone vapor takes place. Cooling of this region (as a result of water evaporation) and dilution of the reaction components with water vapor results in instant quenching of the flame. The upper part of the flame (not accessible for DW) keeps burning to completion (t = 0.08–0.2 s).

(i.e., reaches about 10 cm). Accordingly, the area of the visible flame quenching zone amounts to $10 \times 42 \approx 420$ cm^2. The length of this zone is about one-third of the total circle with a radius of ≈21 cm. Therefore, this area accommodates ≈1.6 cm^3/3 ≅ 0.53 cm^3 of water, which corresponds to a 0.53 cm^3/420 cm^2 ≅ 0.0013 cm thick water layer (or ~0.001 g of water) per unit surface area. The flame thickness (in the direction normal to the burning paper) was on the order of ≈1 cm. Therefore, the volume of water in the flame quenching zone is $\approx 10^{-3}$ of the flame volume and, hence, the density of water evaporated in the flame is on the order of

10^3 g/cm^3, which corresponds to the density of air and gaseous reaction products in the flame.

Thus, the results of our model experiments and the obtained estimates imply, despite their rough character, a simple physical meaning: the flame quenching in the region of fire requires injecting an amount of DW approximately equal to the mass of gaseous reaction products in the flame zone.

Using these estimates, we can evaluate the level of expenditures necessary for extinguishing a large-scale fire. For example, the flame volume in a fire over an area of 100×100 m^2 and a height of ~10 m is $\approx 10^5$ m^3. According to our experimental data, quenching the flame would require producing ~10^5 m^3 of a DW aerosol, which consumes ~10^2 m^3 of liquid water. The production of such an amount of DW requires an energy of about $(1–2) \times 10^2$ MJ, which is equivalent to 25–60 kg of explosive (TNT equivalent).

Apparently, a DW cloud of such dimensions should be generated by synchronously initiating charges placed in containers (readily broken without fragments) with water, uniformly distributed over the flame volume. Note that the dispersion of water can be accompanied by a sharp drop in the explosive load [8].

Finally, it should be noted that the above estimates are quite rough (not taking into account scaling factors), possess a preliminary character, and can be refined in subsequent investigations.

Acknowledgments. This study was performed within the framework of Scientific Innovation Collaboration Program (project no. 2.06.26) supported by the Ministry of Education and the Ministry of Atomic Energy of the Russian Federation.

REFERENCES

1. Ya. S. Povzik, *Fire Extinguishing Tactics* (Spetstekhnika, Moscow, 1999), p. 39.
2. A. Ya. Korol'chenko, Pozharovzryvobezopasnost, No. 2, 3 (2001).
3. V. D. Zakhmatov and A. S. Kozhemyakin, Pozharovzryvobezopasnost, No. 5, 69 (1999).
4. Yu. V. Zuev, A. V. Karpyshev, and I. A. Lepeshinskiĭ, RF Patent No. 2107554; Byul. Izobret., No. 9, 1998.
5. V. K. Kedrinskiĭ, *Hydrodynamics of Explosion: Experiment and Models* (Sib. Otd. Ross. Akad. Nauk, Novosibirsk, 2000).
6. S. V. Stebnovskiĭ and N. V. Chernobaev, Prikl. Mekh. Tekh. Fiz., No. 1, 57 (1986).
7. M. V. Bliznetsov, I. G. Zhidov, E. E. Meshkov, *et al.*, Pis'ma Zh. Tekh. Fiz. **28** (2), 90 (2002) [Tech. Phys. Lett. **28**, 108 (2002)].
8. *FONTAN: A Setup for Localization and Suppression of Explosive Energy* (NPO Spetsmaterialy, St. Petersburg, 2002).

Translated by P. Pozdeev

Technical Physics Letters, Vol. 29, No. 3, 2003, pp. 221–223. Translated from Pis'ma v Zhurnal Tekhnicheskoĭ Fiziki, Vol. 29, No. 6, 2003, pp. 7–13.

Silicon Carbide Materials Obtained from Rice Husk

G. T. Adylov, Sh. A. Faiziev, M. S. Paizullakhanov, S. Mukhsimov, and É. Nodirmatov

Institute for Materials Science, "Solar Physics" Research and Production Corporation, Academy of Sciences of the Republic of Uzbekistan, Tashkent, Uzbekistan

Revised manuscript received October 8, 2002

Abstract—Thermal processing of a rice husk sol in air at $T \geq 750$°C leads to the phase transformation of amorphous silicon dioxide (SiO_2) into crystobalite (type B samples). Thermal treatment of the same sol at $T \approx 1400$°C in a closed graphite crucible leads to the formation of a mixture comprising hexagonal SiC phases and graphite (type A samples). Unannealed type A samples showed high refractory properties, being stable up to 1650°C. Using kaolin binder in silicon carbide articles leads to a decrease in the material refractoriness. © *2003 MAIK "Nauka/Interperiodica".*

Introduction. Silicon carbide (carborundum) is a well-known material possessing a very broad spectrum of useful electrical, chemical (corrosion-resistant), and mechanical properties. Owing to this combination, silicon carbide based materials are still widely used in modern technology.

According to the existing technology based on the Acheson method [1], silicon carbide is synthesized using solid state reactions at high temperatures (1400–2000°C). Commercial carborundum—a crystalline product with a color variable from light green to black—is obtained in electrical resistance furnaces from pure quartz sand and oil coke. Undesired impurities of Al_2O_3 and Fe_2O_3 are removed in the form of $AlCl_3$ and $FeCl_3$. This is facilitated by adding sodium chloride and sawdust to the charge, rendering it more loose. The synthesis is performed using fine disperse initial materials prepared by prolonged milling.

As can be seen from the above, the solid state synthesis of silicon carbide is an energy-, material-, and time-consuming process, which leads to a high cost of the target product. A high-purity material can be also obtained from gaseous components, but this technology is even more expensive.

The quality of refractories and ceramics depends to a considerable extent on the degree of dispersion of the initial powdered material. Therefore, the problem of searching for new promising sources of raw materials for the obtaining of fine disperse silicon carbide powders is currently important. Our analysis of the patent and research literature showed that such a new promising raw material for the synthesis of silicon carbide is rice husk, which contains (besides organic component) up to 20% of silicon dioxide [2–4]. It is always emphasized that a powder material prepared from rice husk is characterized by high purity and fine dispersity. This circumstance gives high hopes for the development of silicon carbide technology using rice husk. Below, we report the results of investigations related to silicon carbide synthesis from this raw material.

Materials and methods. In order to remove the clay and rock impurities, the initial rice husk was washed in a flow of water. Then the material was heat-treated at 400°C in a laboratory furnace of the SNOL type.

Blank samples having the form of cylinders with a diameter of 20 mm and a height of 50 mm were fabricated by dry pressing at 30 MPa in a setup of the ST-100 type. The binder was a PVA glue taken in an amount of 1 mass %. The samples were treated either in cylindrical graphite crucibles with closed volume (samples of type A) or in corundum boats (samples of type B). The crucibles with samples were placed into a Kryptol furnace and heated at a rate of 50 K/min. The samples were annealed for 2 h at a temperature of 500 and 1400°C and then allowed to cool at an arbitrary rate.

The synthesized materials were used to prepare model articles by semidry molding without binder (for type B samples) or with a binder (≤5 mass % of kaolin, for type A samples). Some of these articles were annealed at 1550°C with subsequent cooling at an arbitrary rate.

The refractory properties of the model pressings were studied in a Kryptol furnace, where the samples could be heated up to 2000°C with the temperatures monitored by an optical pyrometer with an error of ±15 K. By refractoriness we imply the ability of ceramics to withstand high temperatures without fusion. According to the State Standard (GOST 4069-69), the refractory properties are checked as follows. The material to be tested is given the shape of a truncated triangular pyramid (pyroscope) with a height of 30 mm and the bottom and top edge lengths of 8 and 2 mm, respec-

1063-7850/03/2903-0221$24.00

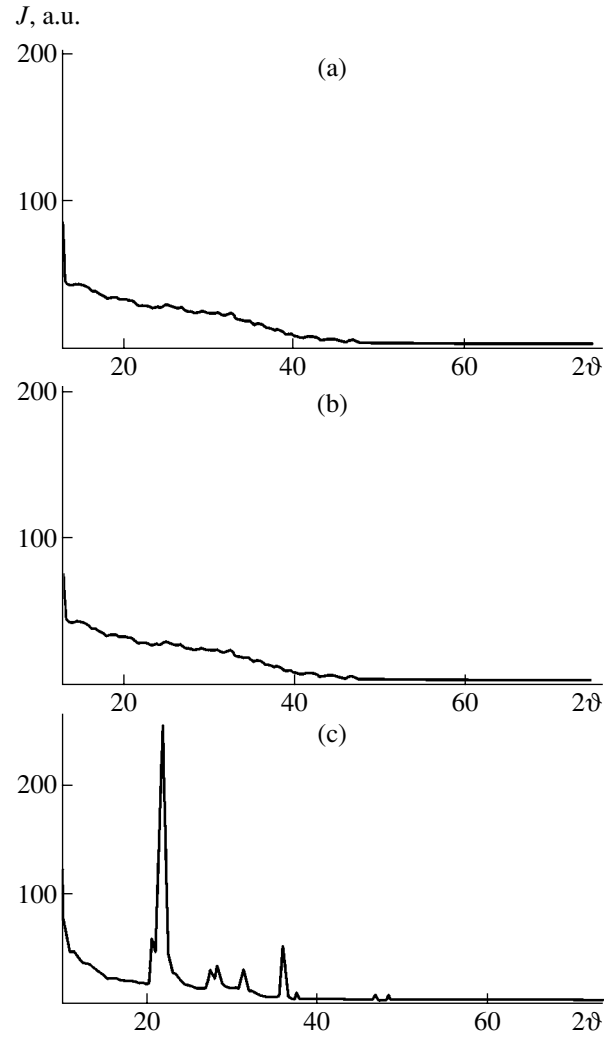

Fig. 1. The X-ray diffraction patterns of rice husk sol treated in a corundum crucible at (a) 400°C, (b) 700°C, and (c) 1400°C.

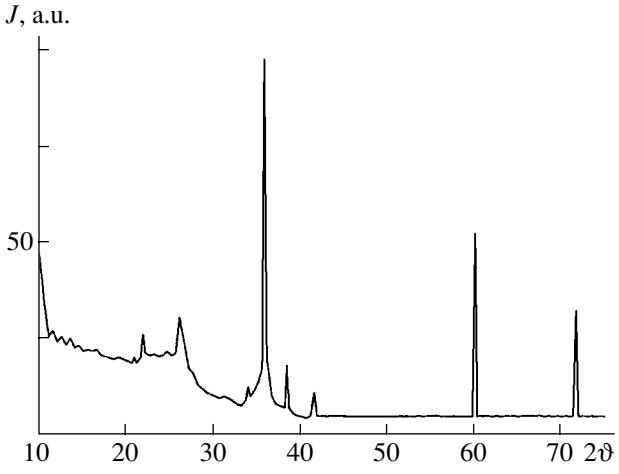

Fig. 2. The X-ray diffraction pattern of a rice husk sol sample treated in a closed graphite crucible at 1400°C.

tively. Refractoriness is characterized by the temperature at which the pyroscope softens so that the pyroscope top touches the base plane.

Since ceramic materials are usually multicomponent and the ready articles frequently contain a glassy phase (besides the main crystalline phases), the temperature of refractoriness characterizes a certain stage in the kinetics of pyroscope softening. This value does not coincide with the melting temperature, which is a physical variable. It is only in single-phase ceramics of special purity (e.g., oxide ceramics) that the refractoriness and the melting temperature coincide.

The phase composition and structural parameters of samples were determined using a DRON-3 using Ni-filtered Cu$K\alpha$ radiation.

Results and discussion. Figure 1a presents an X-ray diffractogram of the rice husk sol heat-treated at 400°C. The diffraction pattern displays only the background scattering without pronounced peaks, which is evidence of the amorphous state of the substance. Figures 1b and 1c show the X-ray diffraction patterns from the samples of type B annealed at 700 and 1400°C, respectively. As is seen, the low-temperature annealing produces no significant changes in the state of the material: the diffraction pattern in Fig. 1b virtually coincides with that in Fig. 1a.

In sharp contrast, the X-ray diffraction pattern from the type B sample annealed at 1400°C (Fig. 1c) is indicative of the crystalline state of the object, showing clear diffraction reflections. The angular positions, interplanar distances, and relative intensities of these diffraction peaks are listed in Table 1. An analysis of these data showed that the diffraction characteristics correspond to a cubic α-SiO_2 crystobalite phase structure with a lattice parameter of a = 7.12 Å.

Thus, the rice husk contains silicon dioxide in an amorphous state that is stable at temperatures up to 700°C. A thermal treatment of this phase in air at 1400°C leads to the phase transformation, whereby the amorphous silicon dioxide crystallizes with the formation of a cubic α-SiO_2 crystobalite phase. Note that this conclusion does not contradict the data of Lee and Cutler [2], according to which the crystallization onset temperature is 750°C.

Figure 2 presents an X-ray diffraction pattern of a sample of the A type. This diffractogram exhibits several peaks with different intensities, the angular positions, interplanar distances, and relative intensities of which are listed in Table 2. An analysis of these data showed that the diffraction characteristics correspond to the presence of two phases: (i) hexagonal silicon carbide α-SiC with the lattice parameters a = 3.37 Å and c = 6.54 Å and (ii) hexagonal graphite C.

Therefore, by heat-treating a rice husk sol under certain conditions, it is possible to synthesize silicon car-

Table 1. The angular positions, interplanar distances, and relative intensities of X-ray diffraction peaks for type B samples annealed at 1400°C

No.	2θ, deg	*d*, Å	J/J_0, %	No.	2θ, deg	*d*, Å	J/J_0, %
1	20.70	4.29	8	6	36.16	2.48	20
2	21.85	4.05	100	7	36.45	2.76	4
3	27.50	3.24	6	8	37.75	2.38	4
4	28.40	3.14	7	9	47.00	1.93	4
5	31.40	2.84	7	10	48.50	1.87	4

Table 2. The angular positions, interplanar distances, and relative intensities of X-ray diffraction peaks for type A samples annealed at 1400°C

No.	2θ, deg	*d*, Å	J/J_0, %	No.	2θ, deg	*d*, Å	J/J_0, %
1	21.74	4.09	7	5	37.40	2.39	22
2	26.00	3.42	14	6	41.40	2.18	27
3	33.70	2.65	26	7	60.00	1.54	48
4	35.60	2.52	100	8	71.64	1.31	46

bide, a material necessary for the production of refractory and abrasive materials and articles.

Table 3 presents the results of testing model ceramic articles for the refractory properties. As can be seen, the maximum refractoriness temperature is observed for a type A sample in the unannealed state. An analysis of the type A sample upon annealing at 1550°C showed that the material contains silicon carbide (SiC), silicon dioxide (SiO_2) in a crystobalite form, and mullite ($3Al_2O_3 \cdot 2SiO_2$). The crystobalite phase can appear as a result of partial oxidation of the silicon carbide phase ($SiC + O_2 \longrightarrow SiO_2 + CO_2$). The presence of a mullite phase is explained by its formation from kaolinite: $3(Al_2O_3 \cdot 2SiO_2 \cdot 2H_2O) \longrightarrow (3Al_2O_3 \cdot 2SiO_2) + 6H_2O$. The ratio of peak intensities corresponding to various phases is $SiC : (3Al_2O_3 \cdot 2SiO_2) : SiO_2 = 1 : 1 : 3$.

The observed deterioration of the refractory properties of the samples upon annealing seems to be due to the presence of crystobalite and mullite phases. The interphase boundary of complicated shape and character plays a specific role in the formation of refractory and abrasive properties of a massive ceramic article. The choice of kaolin as a binder is not well justified. In subsequent investigations, it would be expedient to employ either pure silicon [5] or silicon nitride [6].

Table 3. Refractoriness of ceramic samples prepared from rice husk sol

No.	Sample type	Refractoriness temperature, °C
1	A, unannealed	1650
2	A, annealed	1580
3	B, unannealed	1640
4	B, annealed	1640

Conclusion. By treating rice husk sol under certain conditions, it is possible to synthesize silicon carbide, a valuable material for obtaining refractory and abrasive materials and articles. The use of kaolin as a binder in silicon carbide based ceramics leads to deterioration of their refractory properties.

REFERENCES

1. G. G. Gnesin, *Silicon Carbide Based Materials* (Metallurgiya, Moscow, 1977).
2. J. G. Lee and I. B. Cutler, Am. Ceram. Soc. Bull. **54**, 195 (1975).
3. N. K. Sharma, W. S. Williams, and A. Zancvi, Am. Ceram. Soc. **67**, 715 (1984).
4. S. M. Lakiza and Yu. P. Dyban', Poroshk. Metall. (Kiev), No. 2, 43 (1982).
5. Yu. N. Vil'k and A. P. Garshin, Ogneupory Tekh. Keram., No. 7, 11 (1996).
6. G. D. Semchenko, Ogneupory Tekh. Keram., No. 9, 14 (1996).

Translated by P. Pozdeev

Technical Physics Letters, Vol. 29, No. 3, 2003, pp. 224–225. Translated from Pis'ma v Zhurnal Tekhnicheskoĭ Fiziki, Vol. 29, No. 6, 2003, pp. 14–18.

Autooscillations under Self-Heating Conditions in a Semiconductor

A. V. Melkikh and A. A. Povzner

Ural State Technical University, Yekaterinburg, Russia

e-mail: mav@dpt.ustu.ru

Received September 27, 2002

Abstract—The conditions for autooscillations in a semiconductor possessing an *S*-shaped current–voltage characteristic are considered. The period and amplitude of autooscillations are expressed as functions of the semiconductor bandgap width and the ratios of the characteristic times of the charge and inductance accumulation to that of the heat exchange with the ambient medium. © *2003 MAIK "Nauka/Interperiodica".*

There are narrow-bandgap semiconductors in which the conductivity may change in a jumplike manner as a result of self-heating. The current–voltage (*I–V*) characteristics of such semiconductors acquires an *S*-like shape [1, 2]. Previously [3, 4], we determined critical parameters of the *I–V* characteristics of this type, including the case of a semiconductor–metal junction. Under certain conditions, a system with an S-shaped current–voltage characteristic will possess no stationary solution for the potential difference across the sample, which implies autooscillations. Such processes have been repeatedly studied, including those in semiconductors (e.g., autooscillations in the van der Paul generator).

Unfortunately, the parameters of autooscillations in semiconductors with S-shaped *I–V* characteristics were not determined. Below, we derive expressions for the period, amplitude, and shape of such oscillations as functions of the system parameters (control current, sample geometry, bandgap width, etc.).

The conductivity of a semiconductor can be expressed as

$$\sigma = \sigma_0 \exp\left(-\frac{E_{g0}}{2kT}\right), \tag{1}$$

where E_{g0} is the semiconductor bandgap width. Consider a semiconductor sample having the shape of a round wire of radius *R*. Below, we assume that the heat evolved in the sample is spent for its heating.

Let us consider a nonstationary problem and write the equations of charge and heat balance in a cylindrical semiconductor. For a preset initial current I_{in}, the equation of charge balance in the sample is

$$C\frac{dU}{dt} = I_{\text{in}} - I. \tag{2}$$

The heat balance equation is

$$cm\frac{dT}{dt} = IU - \alpha 2\pi R(T - T_0), \tag{3}$$

where *c* is the specific heat capacity, *m* is the mass, and α is the coefficient of heat transfer. We will assume that the thermal resistance is mostly concentrated at the surface and the temperature is virtually the same through the sample. This situation corresponds to a characteristic current filament radius coinciding with the wire radius [4]. Using relation (1), an expression for the current–voltage characteristic of the sample studied can be written as

$$I = \sigma_0 U \exp\left(-\frac{E_{g0}}{2kT}\right). \tag{4}$$

Owing to the feedback, the current–voltage characteristic is nonlinear. In the presence of inductance, Eq. (4) can be written as

$$I = \sigma_0\left(U - L\frac{dL}{dt}\right)\exp\left(-\frac{E_{g0}}{2kT}\right) \tag{5}$$

or

$$L\frac{dL}{dt} = U - \frac{I}{\sigma_0}\exp\left(\frac{E_{g0}}{2kT}\right). \tag{6}$$

Introducing dimensionless variables

$$\frac{T}{T_0} \equiv T', \quad \frac{E_{g0}}{2kT_0} \equiv E'_{g0}, \quad dt' \equiv \frac{\alpha 2\pi R}{cm}dt,$$
$$I \equiv I'\sqrt{\alpha 2\pi R T_0 \sigma_0}, \quad U \equiv U'\sqrt{\frac{\alpha 2\pi R T_0}{\sigma_0}}, \tag{7}$$

we can rewrite Eqs. (2)–(4) as

$$\frac{dT'}{dt'} = I'U' - (T' - 1), \tag{8}$$

1063-7850/03/2903-0224$24.00

$$\frac{\alpha 2\pi R\sigma_0 L}{cm}\frac{dI'}{dt'} = U' - I'\exp\left(\frac{E'_{g0}}{T'}\right), \quad (9)$$

$$C\frac{\alpha 2\pi R}{cm\sigma_0}\frac{dU'}{dt'} = I'_{\text{in}} - I'. \quad (10)$$

Omitting primes, we obtain the final system of equations

$$\frac{dT}{dt} = IU - T + 1, \quad (11)$$

$$z\frac{dI}{dt} = U - I\exp\left(\frac{E_{g0}}{T}\right), \quad (12)$$

$$y\frac{dU}{dt} = I_{\text{in}} - I, \quad (13)$$

where $y = C\frac{\alpha 2\pi R}{cm\sigma_0}$ and $z = \frac{\alpha 2\pi R\sigma_0 L}{cm}$ are dimensionless constants representing the ratios of the characteristic times of the charge and inductance accumulation to that of the heat exchange with the ambient medium. Let us consider the behavior of the system in the particular case when the characteristic time of the heat exchange with the ambient medium is significantly shorter than the capacitive and inductive times. Numerically solving the system of Eqs. (11)–(13) using the MathCad program package, we obtained the pattern of the current variation with time presented in Fig. 1 and the system attractor depicted in Fig. 2.

An analysis of the system behavior in time leads to the following conclusions:

(i) The period of autooscillations increases with the z and y values. When the y value increases to a certain level, the system exhibits a transition to decaying oscillations.

(ii) Autooscillations are observed only when the control current falls within a certain interval. The boundaries of this interval correspond to singular points on the S-shaped current–voltage characteristic. Outside the interval, the system exhibits either decaying oscillations or a relaxation process.

(iii) Autooscillations exist for certain values of the semiconductor bandgap width. Beginning with a definite E_{g0} value (about 6.9 for the parameters indicated in the figures), growth in the bandgap width is accompanied by an increase in the amplitude and period of autooscillations. For smaller E_{g0} vales, the autooscillations decay.

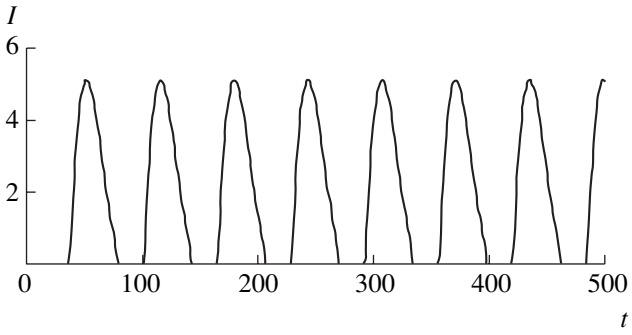

Fig. 1. Time variation of the current in the system with y = 10, z = 10, E_{g0} = 7, and I_{in} = 2.

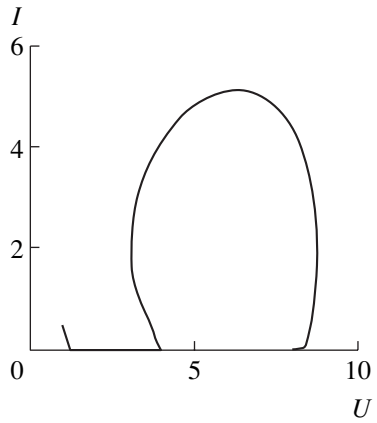

Fig. 2. Attractor (limiting cycle) of the system with y = 10, z = 10, E_{g0} = 7, and I_{in} = 2.

REFERENCES

1. A. F. Volkov and Sh. M. Kogan, Usp. Fiz. Nauk **96**, 633 (1968) [Sov. Phys. Usp. **11**, 881 (1970)].
2. A. Krotkus and Z. Dobrovol'skis, *Electric Conductivity of Narrow-Bandgap Semiconductors* (Mokslas, Vilnius, 1988).
3. A. V. Melkikh, A. A. Povzner, A. G. Andreeva, and I. N. Sachkov, Pis'ma Zh. Tekh. Fiz. **27** (6), 19 (2001) [Tech. Phys. Lett. **27**, 226 (2001)].
4. A. V. Melkikh and A. A. Povzner, Zh. Tekh. Fiz. **72** (7), 141 (2002) [Tech. Phys. **47**, 932 (2002)].

Translated by P. Pozdeev

Technical Physics Letters, Vol. 29, No. 3, 2003, pp. 226–229. Translated from Pis'ma v Zhurnal Tekhnicheskoĭ Fiziki, Vol. 29, No. 6, 2003, pp. 19–25.

Quasi-One-Dimensional Distribution of Macropores in Anodically Etched Uniaxially Stressed Silicon Plates

V. I. Emel'yanov, K. I. Eremin, V. V. Starkov, and E. Yu. Gavrilin

International Laser Center, Moscow State University, Moscow, Russia

Institute for Problems of Microelectronic Technologies, Russian Academy of Sciences, Chernogolovka, Moscow oblast, Russia

Received September 17, 2002

Abstract—Gradual transition from quasi-hexagonal to quasi-one-dimensional order was experimentally observed in an arrangement of macropores etched on the surface of a Si(100) plate inhomogeneously strained by bending. The observed phenomenon is theoretically described within the framework of a defect-deformation mechanism of the formation of ordered ensembles of seeding pores in etched semiconductors and metals.

Introduction. The formation of macropores and nanopores in semiconductors in the course of electrochemical etching has been extensively studied in recent years. This interest is explained by the important practical applications of macroporous silicon in some new fields, such as photonic crystals [1–3], and in solar cell [4], sensor [5, 6], and silicon-on-nothing (SON) technologies [7], as well as by the use of nanoporous silicon for the generation of visible luminescence [8, 9], optical second-harmonic modes [10], etc.

Recently [11], we have developed a new universal defect-deformation (DD) mechanism explaining the spontaneous formation of a seeding ensemble of macropores on the surface of semiconductors and metals and experimentally observed a latent quasihexagonal order in the arrangement of pores on the etched silicon surface. This order, previously considered as accidental, is predicted according to the DD mechanism.

Below, we report experimental data that confirm that increasing inhomogeneous uniaxial compressive strain in silicon leads to the gradual transition from a quasi-hexagonal to quasi-one-dimensional distribution of pores, as explained by the DD mechanism.

Defect-deformation mechanism. The DD mechanism [11] is based on the notion of formation of point defects (interstitials and vacancies) in the subsurface layer of a crystal in the initial (nucleation) stage of etching, followed by the self-organization of these defects as a result of the lateral flows of interstitials caused by a self-consistent, defect-induced deformation. This DD instability leads to the formation of a lattice in the modulated surface relief, with pileups of interstitials at the relief protrusions [12]. Vacancies generated in the course of etching accumulate at the depressions of the surface relief, thus forming a surface lattice in the density of vacancies: $n_v(\mathbf{r}) = A\exp[i\mathbf{qr} + \lambda_\mathbf{q} t]$ + c.c., where $\mathbf{q}$ is the lattice vector and $\mathbf{r}$ is the radius vector on the surface [11, 12].

The increment of the DD lattice growth on an isotropic surface can be expressed as [11, 12]

$$\lambda_q = -D_i q^2 [1 - q^2 A/(B + Cq^3)], \qquad (1)$$

where D_i is the coefficient of diffusion of interstitials and A, B, and C are positive constants determined by the characteristics of the medium and by the parameters of the etching regime. The value of $q = q_m$ for which the increment reaches maximum determines the DD lattice period: $d = 2\pi/q_m$. On an isotropic surface, a special direction of the $\mathbf{q}$ vector appears as a result of spontaneous breakage of symmetry of the DD system.

We can expect that nonlinear pairwise interactions between the DD lattices [12] generate a superposition of three surface DD lattices with the wave vectors forming an equilateral triangle, which corresponds to a hexagonal DD structure [11]. Indeed, a nonlinear computer-aided analysis of a two-dimensional (film) DD model [14] showed that the DD instability development on an isotropic surface leads to the formation of a steady-state, periodic hexagonal DD structure. The vacancy pileups form a hexagonal cellular surface structure of nucleation centers, at which deep pores are developed in the subsequent stage of anodic etching [11].

Etching under uniaxial stress conditions. If an external uniaxial compressive stress is applied to a sample during etching, the activation energy for the diffusion of interstitials in silicon decreases [15], and the

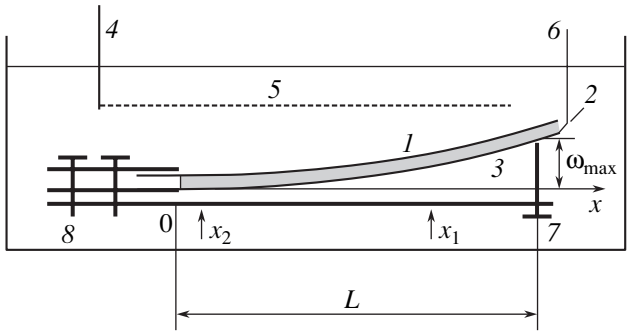

Fig. 1. A schematic diagram of the experiment with electrochemical etching of an inhomogeneously uniaxially strained Si(100) plate: (*1*) silicon plate; (*2*) In–Ga eutectic (anode); (*3*) silicon rubber film isolating the plate bottom surface from etchant; (*4*) cathode; (*5*) etching medium; (*6*) clamp; (*7*) screw; (*8*) clamp. The *x* axis coincides with one of the [100] directions; $x = 0$ corresponds to the clamp; x_1 and x_2 are the coordinates of points imaged in Figs. 2a and 3a, respectively.

coefficient of diffusion along the applied stress direction grows, while that in the perpendicular direction drips. Therefore, the initial isotropic character of the diffusion of interstitials is violated. This corresponds to substituting $D_i \longrightarrow D_i(\theta)$ in formula (1), where θ is the angle between the lattice vector **q** and the axis of compression. The maximum increment corresponds to a DD lattice with the wave vector **q** oriented in the direction of compression ($\theta = 0°$), which implies that uniaxial straining favors a tendency to form a one-dimensional DD lattice (one-dimensional rows of pores).

Experimental results and discussion. To study the effect of straining on the symmetry of an ensemble of pores, we etched the surface of a bent *p*-Si(100) plate (Fig. 1). The plate had a resistivity of 6 Ω cm and was etched in a teflon electrochemical cell for 60 min at a constant current density of $J = 5$ mA/cm^2. The process was conducted in an HF–DMF (1 : 9) mixture at room temperature. The surface of the plate was subject to an inhomogeneous uniaxial compression in the bending direction.

Figures 2a and 3a show micrographs made at two points in a central region of the plate studied in a scanning electron microscope (SEM). The images refer to the points with the coordinates $x_1 = 50$ mm and $x_2 = 5$ mm (see Fig. 1) characterized by a compressive stress of $\sigma_1 = 47$ MPa (Fig. 2a) and $\sigma_2 = 127$ MPa (Fig. 3a). The stress on the etched sample surface varied depending on the distance *x* from the clamp as described by a formula for thin bent plates [16],

$$\sigma(x) = \frac{3Eh\omega_{\max}(x - L)}{2(1 - \nu^2)L^3},$$

where $E = 1.2 \times 10^{12}$ erg/cm^3 is the Young modulus, $\nu \approx 0.3$ is the Poisson ratio, $L = 7.7$ cm is the plate length, $h = 4.6 \times 10^{-2}$ cm is the plate thickness, and $\omega_{\max} = 0.9$ cm is the plate end displacement upon bending.

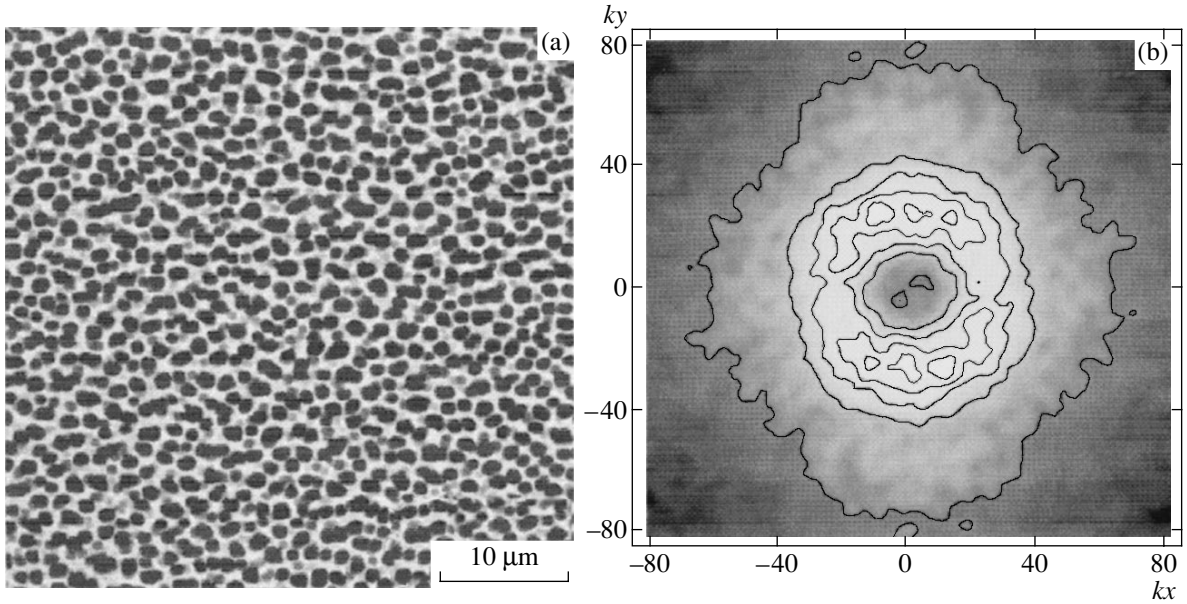

Fig. 2. (a) SEM micrograph of a relatively weakly strained region on the surface of a bent silicon plate ($\sigma_1 = 47$ MPa, the uniaxial compressive stress is applied along the vertical axis); (b) the corresponding 2D Fourier spectrum: k_x and k_y are the dimensionless wavenumbers corresponding to the real wavenumbers $q_x = 2\pi k_x/L_x$ and $q_y = 2\pi k_y/L_y$, where $L_x = L_y = 43$ μm are the dimensions of the surface area scanned in SEM; brighter regions correspond to greater values of $|F(k_x, k_y)|$.

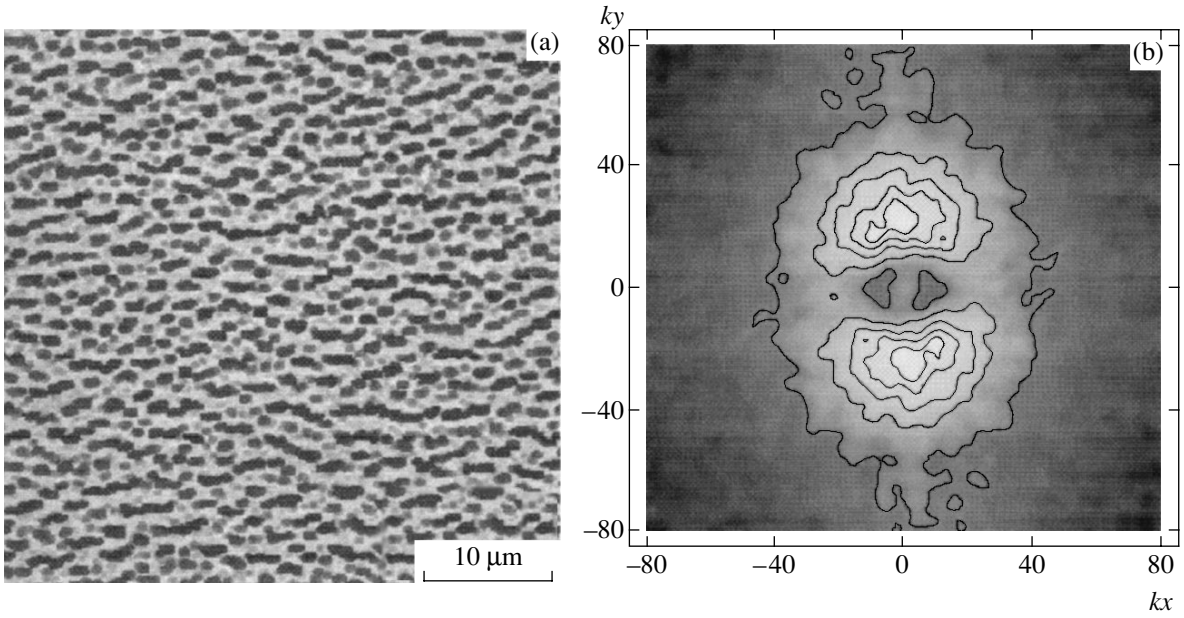

Fig. 3. Same as in Fig. 2, for a relatively stronger strained region on the surface of a bent silicon plate (σ_2 = 127 MPa).

In order to obtain additional information, we performed a two-dimensional (2D) Fourier transform of the SEM micrographs presented in Figs. 2a and 3a. The results of this processing, representing the smoothed amplitude parts of the Fourier spectra $|F(k_x, k_y)|$, are shown in Figs. 2b and 3b. The most interesting feature revealed by the 2D Fourier spectrum of a relatively weakly deformed region (Fig. 2b) is the presence of three pairs of intense maxima, each pair occurring on the ends of diameters passing through the centers of an elliptical ring. The diameter of the central pair is oriented along the compression direction, and the two side pairs are rotated clockwise and counterclockwise by a certain angle relative to this direction. Each pair of maxima corresponds to a lattice in the local image brightness, that is, to a pore lattice.

Thus, the distribution of pores in the region of weak deformation is determined by three pore lattices with wave vectors **q** of approximately equal magnitude, rotated by certain angles with respect to each other, which corresponds to a latent quasihexagonal long-range order in the arrangement of pores. This pattern is explained by the fact that the uniaxial compressive stress, increasing the coefficient of diffusion for interstitials along the stress axis, "entrains" the central DD lattice and aligns the lattice vector in this direction, thus making the central lattice most intense.

In contrast, the tensile stress component perpendicular to the compressive one leads to "repulsion" of the wave vectors of the side DD lattices toward the axis of compression. In the region of relatively large compression, repulsion of the side lattice vectors from the direction of compression becomes so strong that the maxima of the central pair merge with the maxima of the side pairs. As a result, only one pair of relatively broad maxima is observed in the Fourier spectrum (Fig. 3b), which corresponds to the structure of quasiperiodic rows of pores (Fig. 3a).

It should be noted that a 2D Fourier spectrum in the undeformed region with $\sigma \approx 0$ (at the free end of the plate) is generally analogous to that in Fig. 2b, but the contour on which the maxima occur is closer to a circle, and the angles between the diameters connecting the maxima are closer to 60°. In other words, the distribution of pores on the free surface is closer to hexagonal than the pattern in Fig. 2a. Thus, as the compressive stress grows along the plate, the distribution of macropores exhibits a gradual transition from a quasi-hexagonal to a quasi-one-dimensional pattern. Taking into account the universal character of the DD mechanism, such deformation control over the symmetry of the pore ensemble is probably also possible in the case of mesopores and nanopores.

REFERENCES

1. A. G. Cullis, L. T. Canham, and P. D. J. Calcott, J. Appl. Phys. **82**, 909 (1997).
2. D. Kovalev, H. Hackler, G. Polisski, and F. Koch, Phys. Status Solidi B **215**, 817 (1999).
3. L. A. Golovan, V. Yu. Timoshenko, A. B. Fedotov, *et al.*, Appl. Phys. B **73**, 31 (2001).
4. C. Levi-Clement and S. Bastide, Z. Phys. Chem. (Munich) **212**, 123 (1999).
5. R. Angelucci, A. Poggi, L. Dori, *et al.*, Sens. Actuators A **74**, 1 (1999).

6. C. M. A. Ashruf, P. J. French, P. M. Sarro, *et al.*, J. Micromech. Microeng. **10**, 505 (2000).
7. I. Mizishima, T. Sato, S. Taniguchi, *et al.*, Appl. Phys. Lett. **77**, 3290 (2000).
8. A. Chelnokov, K. Wang, S. Rowson, *et al.*, Appl. Phys. Lett. **77**, 2943 (2000).
9. F. Miller, A. Birner, U. Cosele, *et al.*, J. Por. Mater. **7**, 201 (2000).
10. L. A. Golovan', A. B. Fedotov, P. K. Kashkarov, *et al.*, Pis'ma Zh. Éksp. Teor. Fiz. **69**, 274 (1999) [JETP Lett. **69**, 300 (1999)].
11. V. I. Emel'yanov, K. I. Eremin, and V. V. Starkov, Kvantovaya Élektron. (Moscow) **32**, 473 (2002).
12. V. I. Emel'yanov, Kvantovaya Élektron. (Moscow) **28**, 2 (1999).
13. D. Walgraef, N. M. Ghoniem, and J. Lauzeral, Phys. Rev. B **56**, 15361 (1997).
14. V. I. Emel'yanov, Laser Phys. **2**, 389 (1992).
15. M. J. Aziz, Defect Diffusion Forum **153**, 1 (1998).
16. S. A. Ambartsumyan, *Theory of Anisotropic Plates* (Nauka, Moscow, 1967).

Translated by P. Pozdeev

Technical Physics Letters, Vol. 29, No. 3, 2003, pp. 230–232. Translated from Pis'ma v Zhurnal Tekhnicheskoĭ Fiziki, Vol. 29, No. 6, 2003, pp. 26–32.

A Composite Medium with Simultaneously Negative Permittivity and Permeability

G. A. Kraftmakher and V. S. Butylkin

Institute of Radio Engineering and Electronics, Russian Academy of Sciences, Moscow, Russia

e-mail: gkraft@ms.rssi.ru

Received October 30, 2002

Abstract—A new composite medium that possesses simultaneously negative permittivity and permeability in the microwave wavelength range is proposed. The medium is composed of evanescent waveguide structures responsible for the negative permittivity, with embedded cylindrical elements of a one-dimensional chiral medium accounting for the negative permeability. The evanescent waveguide structures exhibit blooming and antiresonances in the reflection coefficient. © *2003 MAIK "Nauka/Interperiodica".*

The problem of creating a medium characterized by simultaneously negative permittivity ε' and permeability μ' and, hence, possessing unusual electromagnetic properties was formulated long ago [1]. However, only recent progress in the development of artificial composite media has provided for a means of solving this task.

Smith *et al.* [2] proposed and realized a composite medium with simultaneously negative ε' and μ', which represented a combination of resonance, ring-shaped conducting inclusions (accounting for the negative effective permeability μ') and a system of conducting rods (responsible for the negative effective permittivity ε'). The formation of a medium possessing simultaneously negative ε' and μ' values in the microwave range was experimentally confirmed by an increase in the coefficient of transmission upon inserting ring inclusions into the initially nontransparent structure of conducting rods. Unfortunately, the low level of the transmitted microwave power (52 to 30 dB) complicates the study of this medium and hinders its practical applications. Therefore, the search for new approaches to creating such media is currently important.

We propose using a composite representing a combination of two media. One of these (accounting for the negative effective permeability μ') consists of cylindrical elements of a one-dimensional chiral medium composed of conducting, oriented separate multithread helices with a common axis, analogous to the systems described previously [3–5]. Figure 1a shows a base material structure comprising a dense periodic grating of parallel copper filaments (with a diameter of 0.1 mm and a separation of $\delta = 0.2$ mm); Fig. 2b shows the structure of a chiral element employing this material. Such chiral samples containing a multiple of 1.5-turn helices were obtained by making rolls with a diameter of $D = 2.5$ mm from a strip of the above material. The rolls were fixed and isolated with the aid of a dielectric shell excluding the contact of helices with the waveguide. The chiral elements were 20 mm long and contained about 80 helices with a twist angle of $\alpha = 70°$.

The interaction of the chiral medium with microwave fields is mediated by resonance circular currents induced in the chiral elements by both electric and magnetic fields. The medium exhibits a resonance response to electromagnetic radiation, referred to below as the chiral resonance. Thermal losses in the helical turns, which carry circular currents excited by an alternating magnetic field, are manifested by magnetic losses. A medium with such chiral inclusions behaves as a magnetodielectric (despite the absence of magnetic components). The chiral inclusions can be considered as resonance loops containing not only active resistance but inductive and capacitive impedance components as well. The resonance behavior of the current induced by a magnetic or electric field accounts for the resonance

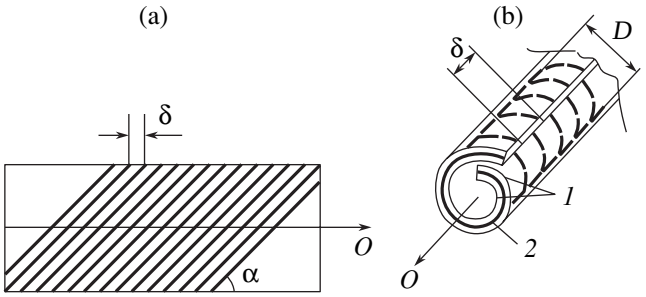

Fig. 1. A component of the medium possessing negative permeability: (a) 0.25-mm-thick material comprising a periodic grating of copper filaments; (b) cylindrical chiral element employing this material, comprising oriented separate multithread 1.5-turn helices with a common axis *O*: (*1*) elastic film material; (*2*) separate conducting helix.

dependence of the effective permeability and permittivity of the composite medium. An increase in the capacitance decreases the resonance frequency, so that resonance effects are manifested in the elements having a length much smaller than the radiation wavelength λ.

Another component of the medium (responsible for the negative effective permittivity ε') represents for the first time an evanescent waveguide structure. A rectangular waveguide, characterized by the propagation constant $\gamma = \frac{2\pi}{\lambda}\sqrt{1(\lambda/2a)^2}$ (H_{10} type wave), can be considered as a medium with an effective permittivity $\varepsilon = 1 - (\lambda/2a)^2$, where a is the wide wall width. As the waveguide size decreases and the evanescent regime is established, ε becomes negative (and the propagation constant becomes imaginary).

The proposed composite medium consists of evanescent waveguide structures (comprising multiple evanescent waveguide cells or parallel metal strips) with embedded cylindrical elements of the one-dimensional chiral medium described above. The microwave properties of such media were studied in waveguides operating in a frequency range from 3.2 to 576 GHz, using samples containing a finite number of cells (Fig. 2). We employed a panoramic voltage standing-wave ratio meter with the main waveguide representing a system of rectangular (48 × 24 mm) waveguides. The evanescent waveguide cells represented a 20-mm section of the main waveguide separated into three parts by metal spacers parallel to the propagation direction (see Fig. 2a) for the *h*-excited chiral resonance, or waveguides of smaller cross sections (23 × 11 mm and 16 × 8 mm) for the 8–12 and 12–18 GHz intervals, respectively (Fig. 2b). Each of the evanescent waveguide structures contained a single cylindrical chiral element with a chiral resonance in the 3–5 GHz interval.

We measured the coefficients of reflection (*R*) and transmission (*T*) of the cylindrical chiral elements in the main waveguide. Chiral resonance peaks of almost equal intensity were observed both for *h*-excitation (with a magnetic microwave field *h* parallel to the axis of helices, whereby the chiral elements behave as magnetodielectrics with resonance behavior of μ" and μ') and for *E*-excitation (with an electric microwave field *E* parallel to the axis of helices, whereby the chiral elements behaves as dielectrics with resonance behavior of ε" and ε'). The frequency dependences of ε' and μ' of the chiral elements in the region of the chiral resonance were measured using half-wave resonators of various lengths. Above the central frequency of the chiral resonance, the system was characterized by negative permittivity and permeability, the resonance values of ε' and μ' being close to each other.

Figure 3a shows the results of measurements of the transmission coefficient *T* in a composite structure corresponding to Fig. 2a, with chiral resonance excited by the magnetic (T_{1h}) and electric (T_{1E}) microwave fields.

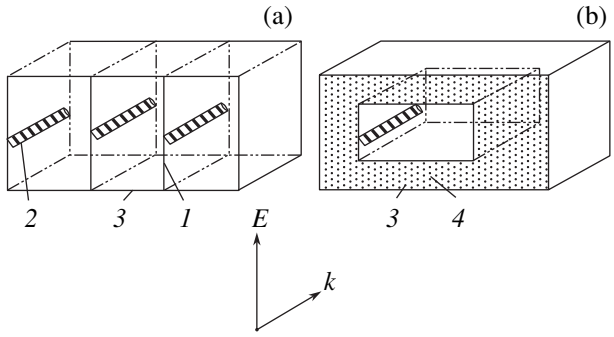

Fig. 2. Two variants of the composite media based on evanescent waveguide cells (for *h*-excitation): (*1*) metal spacers; (*2*) one-dimensional cylindrical chiral elements; (*3*) main waveguide; (*4*) absorber.

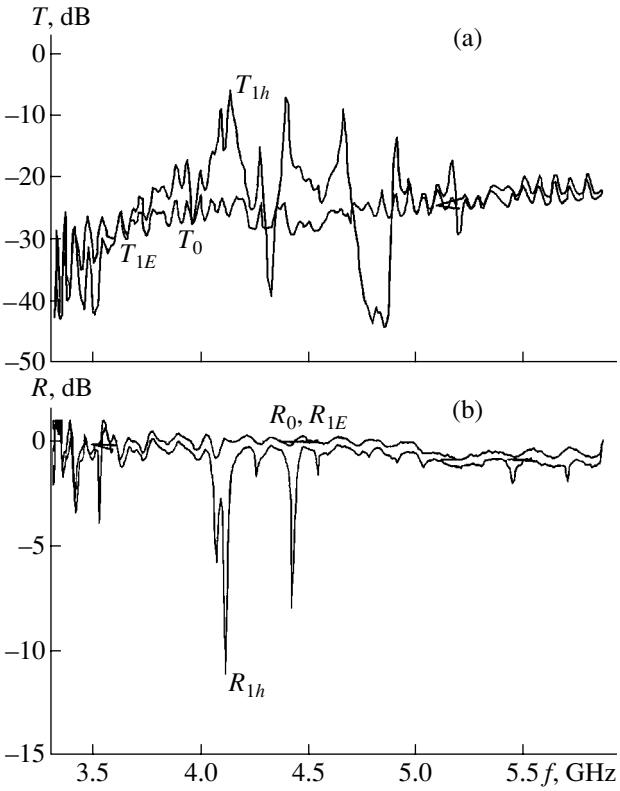

Fig. 3. Frequency dependences of the coefficients of (a) transmission *T* and (b) reflection *R* for an evanescent waveguide structure corresponding to Fig. 2a. Dashed curves show the coefficients of transmission T_0 (reflection R_0) in the absence of chiral elements, coinciding with the values of T_{1E} (R_{1E}) corresponding for the structures with *E*-excited chiral elements. Solid curves show coefficients of transmission T_{1h} (reflection R_{1h}) for the structure with *h*-excited chiral elements.

As can be seen, the evanescent waveguide structures exhibit blooming upon the introduction of chiral elements with orientation corresponding to the *h*-excited chiral resonance. In this case, the cylindrical chiral ele-

ments were situated at the side walls of the evanescent cells (Fig. 2a), at the maxima of the microwave field *h* parallel to the axis of helices. The blooming bands correspond to the chiral resonance peaks observed with the chiral elements arranged in the main waveguide. The multiresonance character of the excitation is related to the strong coupling between helices. In the vicinity of the chiral resonance frequencies, the transmission coefficient T_{1h} (with *h*-excited chiral elements) significantly exceeds T_0 (in the absence of chiral elements), reaching $T_{1h} = -5$ dB. At the same time, the value of T_{1E} (with *E*-excited chiral elements placed at the centers of the evanescent cells, at the maxima of the microwave field *E* parallel to the axis of helices) almost coincides with $T_0 = -(35–25)$ dB. Note that an effective blooming of the evanescent waveguide structures (with T_{1h} exceeding T_0 by more than 20 dB) observed with the cylindrical chiral elements situated at the side walls is observed for element length significantly shorter than the radiation wavelength.

The measurements of the reflection coefficient *R* (Fig. 3b) reveal the blooming effect has a minimum at the chiral resonance frequency (for the *h*-excitation): $R_{1h} = -12$ dB. In the absence of chiral elements or upon their introduction under *E*-excitation conditions, the structures are nontransmitting and almost completely reflect the incident wave ($R_0 \cong 0$ dB, $R_{1E} \cong 0$ dB). Analogous results were obtained for the structures of the type depicted in Fig. 2b.

The observed effects can be explained by taking into account that introduction of the chiral elements with negative μ' into the evanescent waveguide structures characterized by negative ε' leads to the formation of a medium possessing simultaneously negative permittivity and permeability.

Acknowledgments. The authors are grateful to S.L. Prosvirnin for fruitful discussions.

This study was supported by the Russian Foundation for Basic Research, project nos. 01-02-97049 and 01-02-16794.

REFERENCES

1. V. G. Veselago, Usp. Fiz. Nauk **92**, 517 (1967) [Sov. Phys. Usp. **10**, 509 (1967)].
2. D. R. Smith, W. J. Padilla, D. C. Vier, *et al.*, Phys. Rev. Lett. **84**, 4184 (2000).
3. G. A. Kraftmakher and Yu. N. Kazantsev, in *Advances in Complex Electromagnetic Materials* (Kluwer Academic, New York, 1997), pp. 341–358; NATO ASI Ser., Ser. 3 **28**.
4. Yu. N. Kazantsev and G. A. Kraftmakher, Radiotekh. Élektron. (Moscow) **42**, 277 (1997).
5. G. A. Kraftmakher and Yu. N. Kazantsev, Radiotekh. Élektron. (Moscow) **44**, 1510 (1999).

Translated by P. Pozdeev

Technical Physics Letters, Vol. 29, No. 3, 2003, pp. 233–234. Translated from Pis'ma v Zhurnal Tekhnicheskoĭ Fiziki, Vol. 29, No. 6, 2003, pp. 33–37.

Effect of an Adsorption-Active Medium on Quasimicroplastic Deformation in Solids

G. G. Kochegarov

Joint Institute for Geology, Geophysics, and Mineralogy, Siberian Division, Russian Academy of Sciences, Novosibirsk, 630090 Russia

e-mail: teleshev@uiggm.nsc.ru

Revised manuscript received October 29, 2002

Abstract—An adsorption-active medium (distilled water, which is chemically neutral under normal conditions) is capable of influencing the quasimicroplastic (QMP) deformation in solids—a fundamental effect of irreversible deformation in the range of low strains ($\varepsilon \approx 10^{-6}$). The results of experiments with heulandite (a zeolite mineral) showed that the adsorption-active medium reduces the energy barrier for the QMP deformation and increases the rate of this process. The mechanism of the QMP deformation in the presence of the adsorption-active medium remains unchanged, being mediated by single structural relaxation events in the vicinity of point defects. © *2003 MAIK "Nauka/Interperiodica"*.

Introduction. Investigations of the mechanical properties of solids in the range of small strains ($\varepsilon \approx 10^{-6}$), which is traditionally considered as belonging to the elastic region, showed the presence of residual (irreversible) deformations under standard conditions [1, 2]. This phenomenon, owing to the specific character of its manifestation, is called quasimicroplastic (QMP) deformation in solids. QMP nonelasticity is observed both in plastic polycrystalline and single-crystal materials (such as copper) and in typically brittle polycrystalline substances and single crystals such as quartz [1], which is conventionally considered as absolutely brittle material at room temperature [3]. The specific features of the QMP mechanism, responsible for the small inelastic deformation of materials strongly differing in their nature and for their physicochemical properties, allow this phenomenon to be regarded as a fundamental property of solids [1].

This paper reports on the continuation of investigations of the QMP phenomenon and presents the results of experiments devoted to establishing the possible influence of a physicochemical (adsorption) interaction between a solid and a liquid medium on the QMP deformation process.

As is known, a physicochemical interaction with an adsorption-active medium can significantly modify the mechanical properties of various crystals and amorphous solids (the Rehbinder effect) [4]. The change in the surface structure and mechanical properties of solids in a loaded state under the conditions of adsorption interaction with the ambient medium is related to an increase in the mobility of dislocations, which results from a decrease in the surface energy caused by this interaction [5]. Therefore, we may expect that this decrease in the surface energy will also favor a more intense course of the QMP deformation process.

Method of investigation. The experiments were performed with samples of heulandite—a zeolite mineral obtained from the Pashinsk deposit. The ambient medium was distilled water, which is adsorption-active but chemically neutral with respect to most solids under normal conditions (atmospheric pressure, 25°C). The samples were tensile tested using loading–unloading cycles with gradually increasing load in the region of $\varepsilon \approx 10^{-6}$ and a duration of 1–2 s. The elongation of a plane-parallel plate with the linear dimensions $70 \times 5 \times 3$ mm was measured using an optico-mechanical technique. The error of strain measurements in the region of $\varepsilon \approx 10^{-6}$ was about ±10% (according to the method employed, the relative error decreases with increasing deformation).

The sample was characterized by a total strain under load and a residual strain (QMP deformation) upon unloading. The measurements were performed on a sample preliminarily dried at 105°C (referred to below as the dry sample) and on samples saturated with water to various degrees characterized by the water content χ. The material showed no signs of creep under the experimental conditions studied. The experimental procedure has been described in more detail elsewhere [1].

Experimental results and discussion. The effect of the adsorption-active medium on the QMP process is illustrated by the stress–strain curves presented in the figure. As can be seen, saturation of the zeolite with distilled water increases the QMP deformation rate as compared to that in the dry sample. An increase in the χ value from 0.22 to 0.91 wt % is also accompanied by a growth in the magnitude of the QMP deformation. At the same time, the presence of the adsorption-active

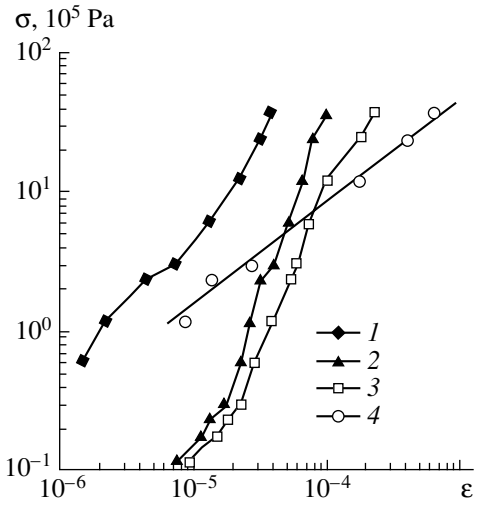

The σ–ε diagrams of a zeolite mineral: (*1*) residual deformation of a dry sample; (*2*, *3*) residual deformation of s sample saturated with water to χ = 0.22 and 0.91 wt %, respectively; (*4*) elastic deformation of the sample with χ = 0.91 wt %.

medium decreases the initial level of stresses corresponding to the onset of the QMP deformation: from $\sigma_d = 6.1 \times 10^4$ Pa for the dry sample to $\sigma_w = 1.2 \times 10^4$ Pa for a water-saturated one. The experimental results also show that, in the region of initial stresses $\sigma < 1.2 \times 10^5$ Pa, only residual deformations (without elastic component) are observed for a wet sample (see curve *2* in the figure). Elastic deformations in this sample appear only at $\sigma_e \geq 1.2 \times 10^5$ Pa, which is one order of magnitude higher than the level of stresses at which irreversible straining takes place (curve *4*).

The structure of zeolites is based on the framework of $[(Si,Al)O_4]$ tetrahedra. Being similar to the skeleton of field spars, this framework is more open: zeolites possess a pore structure featuring voids and channels. The pore opening diameters range from 0.3 to 0.9 nm [6]. Owing to this feature, zeolites are capable of absorbing molecules, including organic substances. This property is used in molecular sieves. The diameter of a water molecule (estimated using the distance between nearest neighbors in ice structure) can be taken as equal to about 0.276 nm [7]. This implies that zeolites can be saturated with water molecules absorbed over virtually the whole material volume. On heating, the absorbed water molecules are removed without breaking bonds in the frame.

The QMP deformation in solids is observed for initial stresses two orders of magnitude lower than those corresponding to the onset of microplastic flow in the plastic materials (i.e., to the start of dislocation motion [8]) and about five orders of magnitude lower than the critical stress of shear in brittle covalent crystals [1]. Estimates of the QMP deformation energy density showed that this value is 8–10 orders of magnitude lower than the energy density of the same material subjected to a plastic flow. This led to the conclusion that QMP deformation proceeds by single structural relaxation events on a substructural level, while the QMP deformation energy is spent mostly on the displacement of point defects (vacancies, interstitials, and substituted atoms occurring in a metastable state and acting as stress concentrators) to more stable structural positions [2].

Apparently, the character of the QMP deformation mechanism does not change in the presence of an adsorption-active medium. Indeed, the QMP deformation in a dry sample is manifested for stresses about five times greater than those in the same material saturated with water ($\sigma_d \approx 5\sigma_w$). Therefore, the QMP deformation energy density in the wet sample is lower as compared to that in the dry state, which significantly reduces the possibility of dislocation motion in the former case. Thus, the adsorption-active medium only decreases the energy barrier for the single structural relaxation events involved the QMP deformation process.

Conclusion. QMP deformation of a solid in an adsorption-active medium proceeds more intensively, which is manifested by increasing residual deformations in the same interval of stresses and by decreasing initial level of stresses producing such deformation. Therefore, the influence of the adsorption-active medium (the Rehbinder effect) is related to substructural changes in the material lattice preceding the motion of dislocations involved in the QMP deformation.

REFERENCES

1. G. G. Kochegarov, Pis'ma Zh. Tekh. Fiz. **25** (17), 29 (1999) [Tech. Phys. Lett. **25**, 688 (1999)].
2. G. G. Kochegarov, Pis'ma Zh. Tekh. Fiz. **26** (11), 41 (2000) [Tech. Phys. Lett. **26**, 467 (2000)].
3. R. J. Stokes, Fracture **7**, 157 (1972).
4. P. A. Rehbinder and E. D. Shchukin, Prog. Surf. Sci. **3** (2), 97 (1972).
5. G. G. Kochegarov, Dokl. Akad. Nauk **376**, 324 (2001) [Dokl. Phys. **46**, 26 (2001)].
6. *Concise Chemical Encyclopedia*, Ed. by I. L. Knunyants (Sov. Éntsiklopediya, Moscow, 1964), Vol. 3, p. 280.
7. *Physical Encyclopedic Dictionary*, Ed. by B. A. Vvedenskiĭ (Sov. Éntsiklopediya, 1960), Vol. 1, p. 289.
8. E. F. Dudarev, *Microplastic Deformation and Yield Stress of Polycrystalline Solids* (Izd. Tomsk. Univ., Tomsk, 1988).

Translated by P. Pozdeev

Technical Physics Letters, Vol. 29, No. 3, 2003, pp. 235–236. Translated from Pis'ma v Zhurnal Tekhnicheskoĭ Fiziki, Vol. 29, No. 6, 2003, pp. 38–41.

The Bragg Law Modified for X-ray Diffraction from a Bent Crystal in the Backscattering Mode

T. Tchen

Moscow State Academy of Fine Chemical Technology, Moscow, Russia
e-mail: docent65@mtu-net.ru; ttchen@e-mail.ru
Received October 10, 2002

Abstract—It is demonstrated for X-ray diffraction from a bent crystal in the backscattering mode that the Bragg angle in the crystal can differ from the value in vacuum by ~10^{-2}. This difference exceeds the angular width of the region of total reflection for the Cu$K\alpha$ radiation backscattered from the (220) plane of a silicon single crystal. The Bragg law modified with allowance for the refraction and crystal bending is presented. © *2003 MAIK "Nauka/Interperiodica".*

The Bragg law determining the angular positions of maxima for the X-ray diffraction in a crystal can be written with allowance for refraction in the following form:

$$2d\sin(\theta_{B,vac} - \Delta\theta^{(refr)}\sin^2\theta_{B,vac}) = \lambda_0(1-\chi_{0r})^{1/2}, \quad (1)$$

where d is the interplanar spacing in the crystal, λ_0 is the radiation wavelength in vacuum, $\chi_{0r} < 0$ is the real part of the Fourier component χ_0 of the X-ray polarizability, and $\Delta\theta^{(refr)}$ is a refraction correction to the Bragg angle $\theta_{B,cryst}$ in the ideal (unbent) crystal relative to the value in vacuum $\theta_{B,vac}$.

Let us expand the left-hand part of Eq. (1) into a Taylor series with respect to $\Delta\theta^{(refr)}$ in the vicinity of $\theta_{B,vac}$ and restrict the expansion to the terms on the order of ~$(\Delta\theta^{(refr)})^2$. Expanding the right-hand part of Eq. (1) in powers of χ_{0r} and also rejecting the terms above second order in this parameter, we arrive at the approximate equation

$$\begin{aligned} 2d[&\sin\theta_{B,vac} - \Delta\theta^{(refr)}\cos\theta_{B,vac}\sin^2\theta_{B,vac} \\ &+ (\Delta\theta^{(refr)})^2\sin^2\theta_{B,vac}\cos\theta_{B,vac}\sin 2\theta_{B,vac} \\ &- (\Delta\theta^{(refr)})^2\sin^5\theta_{B,vac}/2] = \lambda_0\{1-\chi_{0r}/2-(\chi_{0r})^2/8\}. \end{aligned} \quad (2)$$

Equating the coefficients of terms with the same powers of $\Delta\theta^{(refr)}$ and χ_{0r}, we obtain the following relations:

$$2d\sin\theta_{B,vac} = \lambda_0, \quad (3)$$

$$2d(-\Delta\theta^{(refr)}\cos\theta_{B,vac}\sin^2\theta_{B,vac}) = -\lambda_0\chi_{0r}/2, \quad (4)$$

$$\begin{aligned} 2d[&(\Delta\theta^{(refr)})^2\sin^2\theta_{B,vac}\cos\theta_{B,vac}\sin 2\theta_{B,vac} \\ &- (\Delta\theta^{(refr)})^2\sin^5\theta_{B,vac}/2] = -\lambda_0\chi_{0r}^2/8. \end{aligned} \quad (5)$$

Equation (3) is essentially the Bragg law written with neglect of the X-ray wave refraction at the crystal–vacuum interface. Using Eq. (4), we obtain an expression for the refraction correction:

$$\Delta\theta^{(refr)} = \chi_{0r}/\sin 2\theta_{B,vac}. \quad (6)$$

This formula, well known in the theory [1], is valid for the Bragg angles $\theta_{B,vac} \neq \pi/2$.

The terms quadratic in $\Delta\theta^{(refr)}$ and χ_{0r} have to be taken into account only in the case of Bragg diffraction in the backscattering mode ($\theta_{B,vac} \cong \pi/2$). Using relation (5), we obtain

$$\Delta\theta^{(refr)}(\theta_B = \pi/2) = \pm|\chi_{0r}|/2. \quad (7)$$

The only physically meaningful variant with a minus sign in the left-hand part of this formula corresponds to a negative shift in the Bragg angle: $\Delta\theta^{(refr)} = \theta_{B,cryst} - \pi/2 < 0$. At the same time, Chukhovskii *et al.* [2] demonstrated that elastic bending of a crystal gives rise to a linear change Δd in the interplanar spacing d: $\Delta d/d \cong -\cot\theta_B\Delta\theta^{(bent)}$. This leads to an additional change in the Bragg angle, $\Delta\theta^{(bent)}$, the magnitude of which depends on the radiation penetration depth into the crystal. As a result, the total change in the Bragg angle in the near-surface region of the crystal is

$$\Delta\theta = \Delta\theta^{(bent)} + \Delta\theta^{(refr)}, \quad (8)$$

where

$$\begin{aligned} \Delta\theta^{(bent)} &= \tan\theta_{B,vac}\Delta d/d, \\ \Delta d/d &= (\partial u_z/\partial z)|_{z=0} = t/2R_z. \end{aligned} \quad (9)$$

Here,

$$u_z = -x^2/2R_x - y^2/2R_y + [z-(t/2)]^2/2R_z \quad (10)$$

1063-7850/03/2903-0235$24.00

is the z component of the vector $\mathbf{u}$ describing a shift of atoms in the crystal lattice as a result of the elastic bending; $R_{x,y}$ are the radii of crystal curvature in the plane of diffraction scattering and in the perpendicular plane, respectively; R_z is determined by the components of the tensor of inverse elastic modulus [2]; (x, y, z) are the coordinates of an arbitrary atom in the initial (unbent) crystal lattice; and t is the crystal thickness.

In the special case of backscattering, formula (8) can be replaced with allowance for relations (9) by the following equation:

$$(\Delta\theta)_{\theta \cong \pi/2} \cong \Delta\theta^{(refr)} + (\Delta d/d)^{1/2}. \quad (11)$$

For a sufficiently strongly bent plate with $R_z \approx 0.3$ m and $t \sim 100$ μm, we obtain $t/2R_z \sim 10^{-4}$. The polarizability is typically on the order of $\chi_{0r} \sim 10^{-5}$–10^{-6} (for Cu$K\alpha$ in silicon, $\chi_{0r} \cong -1.5 \times 10^{-5}$). As can be seen, for a strongly bent crystal (at a depth of $z \neq t/2$), the dominating factor determining the shift of the Bragg maximum is the bending rather than the refraction. Moreover, in the backscattering mode, the shift amounts to $\Delta\theta \leq 10^{-2}$, which is greater than the angular width of the total reflection region $(\Delta\theta)_{total} \cong |\chi_{hr}|^{1/2} \cong 3 \times 10^{-3}$ for the Cu$K\alpha_1$ radiation backscattered from the (220) plane of a silicon single crystal.

However, at a half-thickness of the crystal ($x = t/2$), the effect of bending on the Bragg angle decreases, and $\Delta\theta^{(bent)}$ can be on the order of or even smaller than the shift $\Delta\theta^{(refr)}$ due to refraction. In addition, a bent crystal can feature another interesting situation, whereby the effect of bending compensates for the refraction correction $\Delta\theta^{(refr)}$, so that $(\Delta\theta)_{\theta \cong \pi/2} \ll \Delta\theta^{(refr)}$.

As the bending radius R_z increases, the dependence of $\Delta\theta$ on R_z becomes less pronounced, and eventually (for $R_z \gg t/\chi_{0r}$) the shift $\Delta\theta$ tends to a constant value determined by refraction.

Thus, the Bragg angle in an elastically bent crystal depends on the X-ray wave penetration depth as $\sim(z - t/2)^{1/2}$, while the shift component due to the refraction is a linear function of the polarizability. The Bragg law can be written with allowance for both refraction and crystal bending in the form of Eq. (1), where $\Delta\theta^{(refr)}$ is equal to $\Delta\theta$ given by formula (8). In the backscattering mode, this formula has to be replaced by $\Delta\theta$ in the form of (11).

REFERENCES

1. Z. G. Pinsker, *X-ray Optics* (Nauka, Moscow, 1982).
2. F. N. Chukhovskii, W. Z. Chang, and E. Förster, J. Appl. Phys. **77**, 1843 (1995).

Translated by P. Pozdeev

Technical Physics Letters, Vol. 29, No. 3, 2003, pp. 237–239. Translated from Pis'ma v Zhurnal Tekhnicheskoĭ Fiziki, Vol. 29, No. 6, 2003, pp. 42–47.

Particle Beam Polarization in Storage Rings Controlled by Longitudinal Magnetic Field

A. Ya. Silenko

Institute for Nuclear Problems, Belarussian State University, Minsk, Belarus

e-mail: silenko@inp.minsk.by

Received October 15, 2002

Abstract—It is suggested to use a longitudinal magnetic field for changing the polarization of particles (electrons, positrons, muons) in the beam of a storage ring. The change from vertical to longitudinal polarization by single or multiple switching of the longitudinal field for a certain time interval is considered. © *2003 MAIK "Nauka/Interperiodica".*

The problem of controlling the polarization of particle beams in storage rings is currently of importance. In this way, it would be possible to obtain beams of longitudinally polarized electrons with the polarization vector parallel to the momentum [1, 2]. A beam polarized in the vertical direction (along a homogeneous magnetic field B_z) can be rendered longitudinally polarized by passing it through the region of a horizontal magnetic field in a rectilinear part of the trajectory. After traveling a certain distance, the particle spin rotates through 90° to align in the momentum direction. Subsequently, the reverse spin transformation is applied to restore the vertical polarization [1, 2]. A beam can be longitudinally polarized using a so-called siberian snake [3].

In the range of nonrelativistic energies, the beam polarization can be effectively controlled by a transverse electric field, which readily rotates the velocity vector while almost not changing the spin [4]. The orientation of a spin ensemble can be also controlled using a high-frequency field in resonance with a free precession of the particle spin [5]. In some papers, including those cited above, the problem of obtaining a stationary closed spin orbit with a fixed direction of the polarization vector at a given azimuth was successfully solved.

This paper proposes an alternative method for controlling the polarization of particle beams. According to this method, the polarization of a beam of polarized electrons, positrons, or muons is changed with the aid of a longitudinal magnetic field B_ϕ. This field can act upon particles along the entire trajectory, which is especially important for storage rings having the circular shape. At all probability, this method can provide for the obtaining of beams with a high degree of polarization. The magnetic field B_ϕ can be generated by a toroidal coil.

It should be noted that, in contrast to the methods mentioned above, the polarization of all particles in the beam controlled by the proposed method is the same and is changed simultaneously for all particles. In this case, projections of the polarization vector on the axes of a cylindrical coordinate system are independent of the azimuth. It is also important to note that the longitudinal magnetic field tangent to the trajectory of particles does not influence their motion.[1] The field either operates for a certain period of time or is switched on and off several times. As a result, the polarization vector (or the doubled average spin) rotates through the required angle.

Rotation of the polarization vector will be characterized by a vector **o** representing the angular velocity of spin precession in the coordinate system related to the moving particle. This vector characterizes the orientation of the mobile spin quantization axis (see [6]). In the presence of both a vertical (B_z) and longitudinal (B_ϕ) magnetic field and a focusing electric or magnetic field, this vector lies in the plane of vectors $\mathbf{e}_\phi$ and $\mathbf{e}_z$ and can be expressed as [7][2]

$$\mathbf{o} = -\frac{e}{2m}\left[\frac{g}{\gamma}B_\phi\mathbf{e}_\phi + (g-2)B_z\mathbf{e}_z\right], \qquad (1)$$

where γ is the Lorentz factor. The angle between the vector **o** and the z axis is determined from the relation [7]

$$\tan\theta = \frac{g}{|g-2|\gamma}\left|\frac{B_\phi}{B_z}\right|. \qquad (2)$$

[1] In the presence of betatron oscillations, the longitudinal magnetic field acts upon the particle trajectory, this action possessing generally focusing character.

[2] Here and below, we use the relativistic system of units in which $\hbar = c = 1$.

1063-7850/03/2903-0237$24.00

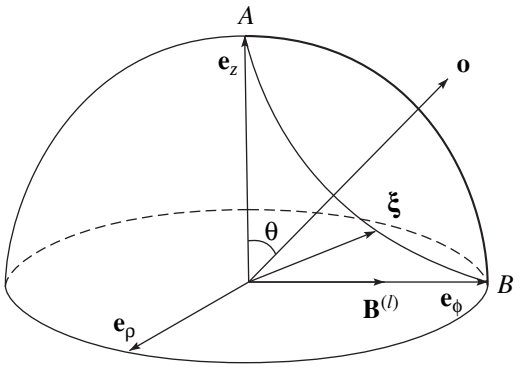

Fig. 1. The beam polarization converted from vertical to longitudinal by single switching of a longitudinal magnetic field: $\boldsymbol{\xi}$ is the polarization vector; $\mathbf{B}^{(l)}$ is the magnetic induction vector of the longitudinal magnetic field; $\mathbf{o}$ is the angular velocity vector of the spin precession in the magnetic field; θ is the angle between vectors $\mathbf{o}$ and $\mathbf{e}_z$; *A* and *B* are the points on the sphere of unity radius indicating positions of the end of vector $\boldsymbol{\xi}$ at the moments when the magnetic field is switched on and off, respectively.

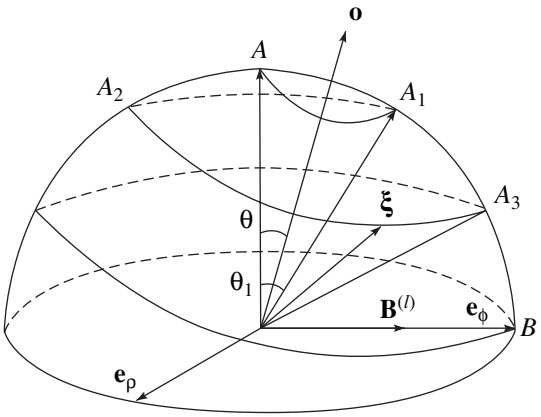

Fig. 2. The beam polarization converted from vertical to longitudinal by triply switching a longitudinal magnetic field: θ_1 is the angle determining a change in the orientation of vector $\boldsymbol{\xi}$ upon the first switching of the field; points *A* (A_1) and A_2 (A_3) indicate the positions of the end of vector $\boldsymbol{\xi}$ at the moments when the magnetic field is switched on (off) for the first and second time, respectively; and point *B* corresponds to the beam acquiring longitudinal polarization. Other notations as in Fig. 1.

In the case under consideration, the period of spin precession is

$$T = \frac{2\pi}{|\mathbf{o}|} = \frac{4\pi m}{|e|\sqrt{\frac{g^2}{\gamma^2}B_\phi^2 + (g-2)^2 B_z^2}}. \qquad (3)$$

For beams of electrons, positrons, and muons, $g/(g-2) \gg 1$.

The vertical polarization of the beam is most readily changed to longitudinal by using an additional field with the strength such that θ = 45°, whereby

$$B_\phi = \pm\frac{(g-2)\gamma}{g}B_z.$$

In this case, the period of precession is

$$T = \frac{4\sqrt{2}\pi m}{|e(g-2)|B_z} = \frac{\sqrt{2}\pi}{|\mu'|B_z},$$

where μ' is the anomalous magnetic moment.

In order to describe the evolution of the beam polarization, let us use the circumstance when (in a cylindrical coordinate system related to the moving particle) the end of the polarization vector ξ moves over a circle on a sphere of unit radius (|ξ| = 1). The position of this sphere is determined by the set of unit vectors $\mathbf{e}_\rho$, $\mathbf{e}_\phi$, $\mathbf{e}_z$. The plane of the circle is perpendicular to vector $\mathbf{o}$ (Fig. 1). In the case under consideration, the magnetic field B_ϕ is switched on for a time period of $\Delta t = T/2$ equal to half of the period of precession. At the moment of switching the field off, the beam of particles initially polarized along $\mathbf{e}_z$ (point *A*) acquires longitudinal polarization along $\mathbf{e}_\phi$ (point *B*).

The beam can be polarized in the longitudinal direction even if the field strength B_ϕ is insufficient for deviating the vector $\mathbf{o}$ by 45° from vertical. According to formula (2), this takes place for a greater energy of particles ($\gamma \gg 1$). Let the vector $\mathbf{o}$ make a relatively small angle θ to the vertical axis. After first switching on the field B_ϕ for $\Delta t_1 = T/2$, where *T* is determined by formula (3), the position of the polarization vector is described by point A_1 on the unit sphere (Fig. 2). The angle between the polarization vector and the *z* axis is $\theta_1 = 2\theta$. Then the transverse magnetic field is switched off and the beam interacts only with the vertical magnetic field B_z during the time period $\Delta t_2 = T_0/2$, where T_0 is the corresponding period of precession:

$$T_0 = \frac{2\pi}{|o_z|} = \frac{4\pi m}{|e(g-2)|B_z} = \frac{\pi}{|\mu'|B_z}.$$

Under the action of vector B_z, the polarization vector exhibits precession about *z* axis and acquires a position described by point A_2. Then the transverse magnetic field is switched on for a time period of $\Delta t_3 = T/2$. As a result, the position of the polarization vector is determined by point A_3 on the unit sphere. This process can be repeated until the beam acquires a longitudinal polarization characterized by point *B*. As can be readily seen, for this purpose the angle θ must obey the condition $\theta = 45°/n$, where *n* is an integer equal to the number of the magnetic field switchings for a time period of $\Delta t = T/2$.

Rotation of the polarization vector caused by rapid switching of the longitudinal magnetic field is negligibly small. The influence of the oscillatory motion in storage rings on the particle beam polarization was

studied in [8, 9]. In the case under consideration, this effect is not large.

According to formula (5), for $\tan\theta \sim 1$ and $|B_\phi/B_z| \le 1$, the change in polarization of the beam of electrons, positrons, or muons can be performed for a Lorentz factor of up to $\gamma \sim 10^3$.

The angular velocity of particle rotation is three orders of magnitude greater than the angular velocity of spin precession. Therefore, during the time required for the particle to make one turn about the circle, the end of the polarization vector rotates through a very small angle. This angle will remain the same on replacing the toroidal solenoid by one or several straight solenoids generating the same average field with the induction $\langle B_\phi \rangle$. The use of straight solenoids can offer technical advantages, since their total length can be significantly shorter than that of the storage ring. However, this configuration involves a certain violation of synchronism in changing the polarization of particles.

A longitudinal magnetic field can provide for almost any change in the beam polarization. However, in contrast to the existing spin rotators [1, 2, 10], use of the proposed system is restricted to the region of small and intermediate energies.

Acknowledgments. The author is grateful to I.A. Koop and B.I. Khazin for valuable remarks and fruitful discussions of results.

REFERENCES

1. D. P. Barber, M. Boge, H. D. Bremer, *et al.*, Phys. Lett. B **343**, 436 (1995).
2. D. P. Barber, Preprint DESY-98-096B (1998); e-print archive: physics/9901041.
3. Ya. S. Derbenev, A. M. Kondratenko, S. I. Serednyakov, *et al.*, Part. Accel. **8**, 115 (1978).
4. I. Koop, E. Pozdeev, Yu. Shatunov, *et al.*, Nucl. Instrum. Methods Phys. Res., Sect. A **427**, 36 (1999).
5. I. B. Vasserman, P. V. Vorobiev, E. S. Gluskin, *et al.*, Phys. Lett. B **198**, 302 (1987).
6. Ya. S. Derbenev and A. M. Kondratenko, Zh. Éksp. Teor. Fiz. **64**, 1918 (1973) [Sov. Phys. JETP **37**, 968 (1973)].
7. A. Ya. Silenko, Zh. Éksp. Teor. Fiz. **114**, 1153 (1998) [JETP **87**, 629 (1998)].
8. F. J. M. Farley, Phys. Lett. B **42B**, 66 (1972).
9. Yu. F. Orlov, *Proceedings of the 13th International Symposium on High Energy Spin Physics (Spin-98), Protvino, 1998*, Ed. by N. E. Tyurin (World Scientific, Singapore, 1999), pp. 509–511.
10. J. Buon and K. Steffen, Nucl. Instrum. Methods Phys. Res., Sect. A **245**, 248 (1986).

Translated by P. Pozdeev

Technical Physics Letters, Vol. 29, No. 3, 2003, pp. 240–242. Translated from Pis'ma v Zhurnal Tekhnicheskoĭ Fiziki, Vol. 29, No. 6, 2003, pp. 48–55.

Far Infrared Radiation Generated during Femtosecond Laser Excitation of a Semiconductor Surface in Magnetic Field

V. L. Malevich

Department of Optical Problems in Informatics, National Academy of Sciences of Belarus, Minsk, Belarus
e-mail: vitaly@optoinform.bas-net.by
Received October 3, 2002

Abstract—The effect of a magnetic field on the generation of electromagnetic radiation pulses in the terahertz frequency range from a semiconductor surface excited by an ultrashort laser pulse is considered within the framework of a hydrodynamic model. The appearance of a photocurrent component in the Hall direction leads to elliptic polarization of the microwave radiation and to a severalfold increase in the generation efficiency. This is consistent with the results of Monte Carlo modeling of a self-consistent field and photogenerated carrier dynamics. © *2003 MAIK "Nauka/Interperiodica".*

As is known [1, 2], the surface of a semiconductor irradiated by short laser pulses with a quantum energy exceeding the bandgap width can generate microwave (terahertz) radiation pulses. This effect is related to a pulse of photocurrent arising during ultrafast screening of the surface electric field by photogenerated charge carriers [3–5]. Depending on the semiconductor parameters and the photoexcitation intensity, the screening may proceed either in the diffusion drift regime or in a collisionless mode. In the former case, the field decays monotonically at a Maxwell relaxation rate, and the generated microwave pulse has a bipolar shape. In the collisionless screening mode, the microwave field decays by oscillating at a plasma frequency.

The microwave radiation generated in the photoexcited subsurface region of the semiconductor is oriented mostly along the sample surface and exhibits total internal reflection due to a typically large refractive index (~3.5). It was demonstrated [6–9] that the microwave generation efficiency can be increased severalfold by applying a magnetic field parallel to the semiconductor surface.

In this study, the effect of a magnetic field on the generation of electromagnetic radiation pulses in the terahertz frequency range from a depleted subsurface region excited by an ultrashort laser pulse was considered within the framework of a hydrodynamic model. It is established that, as the magnetic field intensity increases, the microwave generation efficiency first increases in proportion to the square field strength and then reaches saturation. In addition, the dynamics of screening of the depleted region by photogenerated charge carriers and the effect of microwave generation have been calculated for *n*-GaAs using a multiparticle Monte Carlo method. The two approaches give close results.

Let us consider an *n*-type semiconductor with a depleted surface layer, restricting the analysis to the one-dimensional case when photoexcitation is homogeneous along the sample surface. In addition, taking into account that the effective hole mass is usually much greater than the electron mass, let us ignore the hole contribution to the photocurrent. In the dipole approximation, the field of radiation (generated by the photocurrent arising as a result of the redistribution of photogenerated carriers in the depleted surface region) in the wave zone can be expressed as [10]

$$\mathbf{E}_R = \frac{S}{c^2 R_0}\frac{d}{dt}\left\{\int_0^\infty dx[[\mathbf{jn}]\mathbf{n}]\right\}, \qquad (1)$$

where S is the area of the laser-excited spot on the sample surface, R_0 is the distance from the point of observation to the emitting region, c is the speed of light in vacuum, $\mathbf{j} = -en\mathbf{v}$ is the electric current density, and n and $\mathbf{v}$ are the electron density and velocity, respectively; the unit vector $\mathbf{n}$ is directed to the observation point and the x axis is directed inward to the semiconductor.

The photocurrent arising in a depleted region under the action of the laser radiation is determined by the self-consistent dynamics of the field and photoelectrons. In the presence of a magnetic field, the current density vector $\mathbf{j}$ possesses, besides the component j_x perpendicular to the semiconductor surface, a component j_z oriented in the Hall direction (the magnetic field is assumed to be applied along the y axis), which induces a transverse electric field. However, under the conditions studied, the Hall field is "slow" and the latter transverse component can be ignored. Within the framework of a hydrodynamic plasma model [11], the current components and the longitudinal field compo-

1063-7850/03/2903-0240$24.00

nent F_x are described by the following system of equations:

$$\frac{\partial j_x}{\partial t} + \frac{j_x}{\tau} + \omega_c j_z + \frac{\partial}{\partial x}(v_x j_x) = \frac{\varepsilon}{4\pi}\left(\omega_p^2 F_x - \frac{e}{2m}\frac{\partial F_x^2}{\partial x} - \frac{kT_e}{m}\frac{\partial^2 F_x}{\partial x^2}\right), \quad (2)$$

$$\frac{\partial j_z}{\partial t} + \frac{j_z}{\tau} - \omega_c j_x + \frac{\partial}{\partial x}(v_x j_z) = 0, \quad (3)$$

$$\frac{\varepsilon}{4\pi}\frac{\partial F_x}{\partial t} + j_x = 0. \quad (4)$$

Here, ε is the static dielectric permittivity, m is the effective electron mass, τ is the electron relaxation time with respect to momentum, T_e is the electron temperature, B is the magnetic induction, $\omega_p = (4\pi(N_d^+ + p)e^2/m\varepsilon)^{1/2}$ is the plasma frequency, and $\omega_c = eB/mc$ is the electron cyclotron frequency. Equation (2) was derived using the relation $n = N_d^+ + p - (\varepsilon/4\pi e)(\partial F_x/\partial x)$ following from the Poisson equation, where p and N_d^+ are the densities of nonequilibrium holes and ionized impurities. The photoexcitation level was assumed to be homogeneous at the depth of the depleted layer and, hence, the plasma frequency can be considered as independent of x.

Let the microwave radiation be measured in the xy plane, at an angle of θ relative to the normal. According to Eq. (1), the microwave pulse field has two components, E_{Rp} and E_{Rs}, polarized parallel and perpendicular to the observation plane, respectively. Using Eqs. (1)–(4), these components can be readily expressed as

$$E_{Rp} = \frac{(\varepsilon)^{1/2} S\sin\theta}{4\pi c^2 R_0}\frac{d^2\varphi_s}{dt^2} = -\frac{(\varepsilon)^{1/2} S\sin\theta}{4\pi c^2 R_0}\varphi_{s0}(\omega_p^2 - \omega_{p0}^2)\exp(-t/2\tau)\cos\omega_H t, \quad (5)$$

$$E_{Rs} = \frac{\varepsilon S}{4\pi c^2 R_0}\omega_c\frac{d\varphi_s}{dt} = -\frac{\varepsilon S}{4\pi c^2 R_0}\frac{\omega_c}{\omega_H}\varphi_{s0}(\omega_p^2 - \omega_{p0}^2)\exp(-t/2\tau)\sin\omega_H t, \quad (6)$$

where $\varphi_s(t) = \int_0^\infty dx\, F_x(x, t)$ is the surface potential and $\varphi_{s0} = \varphi_s(t = 0)$ is the initial (dark) surface potential. The final expressions in Eqs. (5) and (6) are obtained upon substituting φ_s as the function of t, determined by solving the equation

$$\frac{d^2\varphi_s}{dt^2} + \frac{1}{\tau}\frac{d\varphi_s}{dt} + \omega_H^2\varphi_s - (\omega_{p0}^2 + \omega_c^2)\varphi_{s0} = 0, \quad (7)$$

where $\omega_{p0} = (4\pi N_d^+ e^2/m\varepsilon)^{1/2}$ and $\omega_H = (\omega_p^2 + \omega_c^2)^{1/2}$ is the frequency of the upper hybrid resonance.

Equation (7) is obtained by integrating Eqs. (2)–(4) over the depleted layer thickness, followed by excluding the current-dependent terms. It was also assumed that $\omega_H \gg \tau^{-1}$, since semiconductors of the $A^{III}B^V$ type most typically feature the collisionless regime. In writing Eq. (7), we have also ignored the last term of Eq. (2) describing the diffusion of charge carriers. As can be readily seen, this assumption is valid provided that the electron temperature satisfies the condition $kT_e/(e\varphi_{s0}) \ll 1$. In the case under consideration, the energy of the electron subsystem increases both as a result of the photogeneration of nonequilibrium carriers and due to the electrons being heated by the field of the depleted layer. Since we are interested in the upper estimate for the electron temperature, we can ignore the radiative energy losses and the part of the energy transferred to the lattice. Then, the electron temperature is given by the approximate relation $kT_e \approx (2/3)(\hbar\omega - \varepsilon_g) + 2N_d^+ e\varphi_{s0}/(9(N_d^+ + p))$, where the first term refers to the photoexcitation ($\hbar\omega$ is the energy of the exciting quantum and ε_g is the semiconductor bandgap width) and the second describes the field-induced heating of electrons. This relation and the condition $kT_e \ll e\varphi_{s0}$ imply that the field-induced heating and diffusion of electrons can be ignored for the exciting radiation frequencies such that $(\hbar\omega - \varepsilon_g)/(e\varphi_{s0}) \ll 1$. The heating of electrons in the field of a depleted layer can be ignored, because this contribution drops with increasing photoexcitation intensity.

As can be seen from Eqs. (5) and (6), the microwave radiation generated in the presence of a magnetic field is elliptically polarized. The ratio of axes of the polarization ellipse is $E_{Rs}/E_{Rp} = (\varepsilon^{1/2}/\sin\theta)(\omega_c/\omega_H)$. The radiation frequency corresponds to the upper hybrid resonance and increases with the pumping field intensity and the magnetic field strength. Using Eqs. (5) and (6), it is easy to show that the dependence of the microwave pulse energy $W(B) \sim \int_0^\infty dt(E_{Rs}^2 + E_{Rp}^2)$ on the magnetic field is determined by the ratio

$$\frac{W(B)}{W(0)} \approx 1 + \frac{\varepsilon}{\sin^2\theta}\frac{\omega_c^2}{\omega_H^2} \quad (8)$$

and, hence, increases with the field strength as $\sim B^2$ and reaches saturation ($\sim 1 + \varepsilon/\sin^2\theta$) for $\omega_c \gg \omega_p$.

The proposed model does not take into account some effects, such as nonparabolic shape of the electron spectrum, heating of electrons, variety of the scattering mechanisms, etc. In order to evaluate the role of

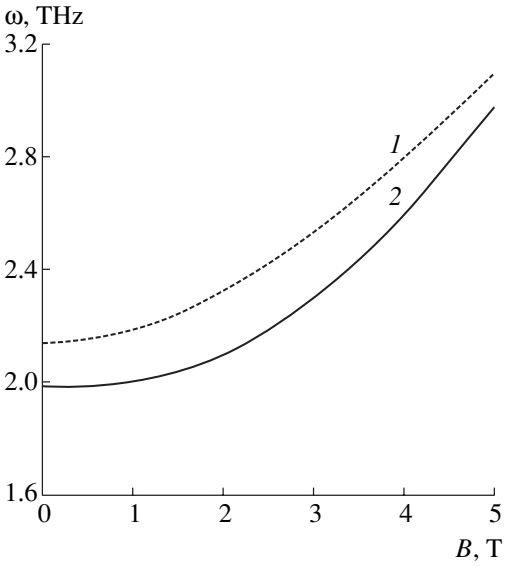

Fig. 1. Plots of the microwave radiation pulse frequency (in the maximum of the spectral distribution) versus magnetic induction in *n*-GaAs ($N_d^+ = 4 \times 10^{15}$ cm^{-3}) excited by a 100-fs laser pulse with a quantum energy of 1.55 eV: (*1*) calculation by the Monte Carlo method; (*2*) upper hybrid resonance frequency. The level of laser excitation at the sample surface corresponds to the carrier density of 5×10^{16} cm^{-3}.

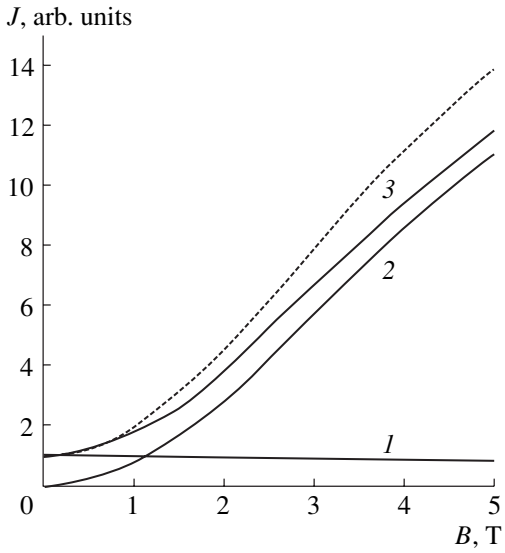

Fig. 2. Plots of the laser-induced microwave radiation pulse intensity versus magnetic induction in *n*-GaAs ($N_d^+ = 4 \times 10^{15}$ cm^{-3}). Dashed curve is calculated using relation (8), solid curves are obtained by the Monte Carlo method for (*1*, *2*) the *p*- and *s*-polarization components, respectively, and (*3*) the total intensity.

these effects, the dynamics of screening of the field of a depleted surface region and the microwave generation in *n*-GaAs ($N_d^+ = 4 \times 10^{15}$ cm^{-3}, $\varphi_{s0} = 0.6$ eV) placed in a magnetic field and excited by 100-fs laser pulses (λ = 800 mm) were studied by Monte Carlo modeling, using the method of macroparticles with randomly played scattering events (described in detail elsewhere [12]). The equations of motion of the macroparticles in crossed electric and magnetic fields were solved by the Runge–Kutta method. The electric field dynamics was calculated by solving the Poisson equation (with neglect of the transverse electric field) at a time step of 5 fs. In Eq. (1), integration of the current with respect to depth was replaced by simple summation of the contributions from separate macroparticles.

The results of modeling showed that the microwave radiation frequency in the presence of a magnetic field (Fig. 1) is close to the upper hybrid frequency. As can be seen from Fig. 2, the plots of the microwave radiation intensity versus magnetic induction obtained by the Monte Carlo method agree well with the data calculated using expression (8). Note that the proposed hydrodynamic model becomes inapplicable when the photoexcitation is produced high into the conduction band (as in the case of microwave radiation excited by laser pulses with an energy of 1.55 eV in *n*-InAs [6–8]), since it is no longer possible to use the energy-independent *m* and τ values.

Thus, when the photoexcitation of a semiconductor takes place near the forbidden band, the main laws of the microwave (terahertz) radiation generation by ultrashort laser pulses in the presence of a magnetic field can be described using the proposed hydrodynamic model. The shape of the microwave radiation pulse is determined by the dynamics of variation of the surface potential in the course of screening of a depleted surface region by photoexcited charge carriers.

REFERENCES

1. X. C. Zhang and D. Auston, J. Appl. Phys. **71**, 326 (1992).
2. B. I. Greene, P. N. Saete, R. D. Douglas, *et al.*, IEEE J. Quantum Electron. **28**, 2302 (1992).
3. R. Kersting, J. N. Heyman, G. Strasser, *et al.*, Phys. Rev. B **58**, 4553 (1998).
4. A. V. Kuznetsov and C. J. Stanton, Phys. Rev. B **48**, 10828 (1993).
5. V. L. Malevich, Surf. Sci. **454–456**, 1074 (2000).
6. N. Sarakura, H. Ohtake, S. Izumida, *et al.*, J. Appl. Phys. **84**, 654 (1998).
7. S. Izumida, S. Ono, Z. Liu, *et al.*, Appl. Phys. Lett. **75**, 451 (1999).
8. V. G. Bespalov, V. Krylov, and D. I. Staselko, *Proceedings of the XVII Int. Conf. on Coherent and Nonlinear Optics (Techn. Digest)* (Minsk, 2001), FC4.
9. M. B. Johnston, D. M. Whittaker, A. Gorchia, *et al.*, Phys. Rev. B **65**, 165301 (2002).
10. L. D. Landau and E. M. Lifshitz, *The Classical Theory of Fields* (Nauka, Moscow, 1973; Pergamon Press, Oxford, 1975).
11. *Plasma Electrodynamics*, Ed. by A. I. Akhiezer, R. V. Polovin, *et al.* (Nauka, Moscow, 1974; Pergamon, Oxford, 1975).
12. V. L. Malevich, Semicond. Sci. Technol. **17**, 551 (2002).

Translated by P. Pozdeev

Technical Physics Letters, Vol. 29, No. 3, 2003, pp. 243–245. Translated from Pis'ma v Zhurnal Tekhnicheskoĭ Fiziki, Vol. 29, No. 6, 2003, pp. 56–62.

An Approximate Analytical Model of Flow in the First Barrel of an Overexpanded Jet

A. V. Omel'chenko, V. N. Uskov, and M. V. Chernyshev

Baltic State Technical University, St. Petersburg, Russia

e-mail: vmu@peterlink.ru

Received October 16, 2002

Abstract—A simple analytical model of flow in the first barrel of a plane overexpanded jet is proposed. The adequacy of the model is confirmed by comparison with the results of numerical calculations. The proposed model is used to solve the problem of determining the Mach disk height in a jet. © *2003 MAIK "Nauka/Interperiodica".*

Consider the efflux of a nonviscous perfect gas at a supersonic velocity ($M_0 > 1$) from a planar profiled nozzle (Fig. 1) in an overexpanded noncalculated ($n < 1$) regime. As a result, a normal shock wave *1* appears at the nozzle edge, the intensity of which $J_1 = 1/n = p_\infty/p_A$ is characterized by the static pressure difference between atmosphere (p_∞) and the nozzle edge (p_A). Once the shock wave intensity J_1 and the Mach number M_0 are known, one can determine the angle $\beta_1(M_0, J_1)$ of the flow rotation at the shock and the Mach number $M_1(M_0, J_1)$ behind the shock (see, e.g., [1]).

In the case of a strongly overexpanded jet ($J_1 \in [J_c(M_0), J_*(M_0)]$, where $J_c(M_0)$ is the intensity of the stationary Mach configuration [2] and $J_*(M_0)$ is the intensity corresponding to the Mach number of unity behind the shock), the shock wave can be irregularly reflected from the symmetry axis, with the formation of a triple shock wave configuration at point *T* (Fig. 1). The jet is supersonic behind the reflected shock wave *2* and subsonic behind the Mach disk *3*. Using the dynamic compatibility conditions on the tangential discontinuity τ originating from point *T* [2]

$$J_1 J_2 = J_3, \quad \beta_1(M_0, J_1) + \beta_2(M_1, J_2) = \beta_3(M_0, J_3)$$

for the given shock wave intensity J_1 and the initial Mach number M_0, it is possible to find the angles β_2 and β_3 of the flow rotation on these shocks and to determine the corresponding intensities J_2 and J_3. For the shock waves depicted in Fig. 1, the angles β_1 and β_3 are negative, while β_2 is positive. When the shock wave *2* reaches the jet boundary *AB*, a centered rarefaction wave *4* is formed at point *B*. Incident upon the tangential discontinuity τ, the latter wave leads to a bending of this discontinuity.

This paper presents an approximate analytical model of flow in the region behind the shock waves originating from point *T*. The model is constructed based on several assumptions. First, we assume that the flow behind shock wave *3* is quasi-one-dimensional. This allows us to relate the ordinate $y(x)$ of the tangential discontinuity τ, the Mach number $M_3(x)$, and the static pressure $p_3(x)$ in the transverse cross section to the analogous quantities y_T, M_{3T}, and p_{3T} at the triple point [2]:

$$\frac{y(x)}{y_T} = \frac{M_{3T}}{M_3(x)}\left[\frac{\mu(M_3(x))}{\mu(M_{3T})}\right]^{1/2\varepsilon},$$
$$\frac{p_3(x)}{p_{3T}} = \left[\frac{\mu(M_{3T})}{M_3(x)}\right]^{(1+\varepsilon)/2\varepsilon}, \qquad (1)$$
$$\mu(M) = 1 + \varepsilon(M^2 - 1).$$

Here, $\varepsilon = (\gamma - 1)/(\gamma + 1)$, γ is the adiabatic index, $p_{3T} = p_1 J_3$, p_1 is the static pressure in the flow in front of the shock wave *1*, and $M_{3T}(M_0, J_3)$ is the Mach number behind the shock wave *3*. The second assumption is that the subsonic flow accelerates to become supersonic behind the Mach disk *3*, the transition taking pace at the critical cross section *CC*' corresponding to a minimum of the $y(x)$ function (Fig. 1). According to the third assumption, the flow behind the shock wave *2* is vortexless and the first family characteristics in the *TBD*

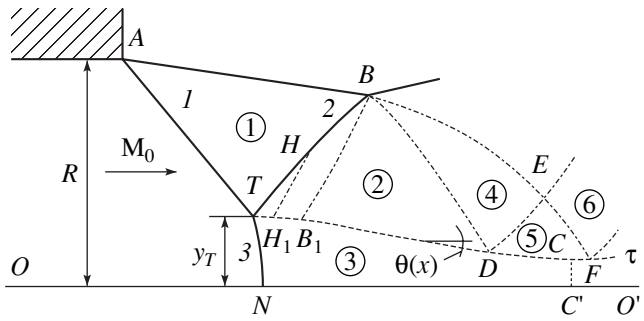

Fig. 1. A pattern of shock waves for the efflux of a plane overexpanded jet of the ideal gas from a profiled nozzle.

1063-7850/03/2903-0243$24.00 © 2003 MAIK "Nauka/Interperiodica"

region are linear. Therefore, the flow in this region represents a simple Prandtl–Meyer wave. The angle ϑ_2 of the current lines relative to the abscissa axis, the static pressure p_2, and Mach number M_2 are related to the corresponding parameters $\vartheta_{2T} = \beta_3$, p_{2T}, and M_{2T} at the point *T* by the following relations [2]:

$$\vartheta_2 = \beta_3 + \omega(M_{2T}) - \omega(M_2), \quad \frac{p_2}{p_{2T}} = \left[\frac{\mu(M_{2T})}{\mu(M_2)}\right]^{(1+\varepsilon)/2\varepsilon},$$
$$\omega(M) = \frac{1}{\sqrt{\varepsilon}}\arctan\sqrt{\varepsilon(M^2-1)} - \arctan\sqrt{M^2-1}. \quad (2)$$

Here, $p_{2T} = p_1 J_1 J_2$, $M_{2T}(M_1, J_2)$ is the Mach number behind jump *2*. The first two assumptions are traditional, being frequently involved in the numerical calculations of flows in supersonic overexpanded jets by the method of characteristics [3, 4]. Justification of the third assumption is provided by an analysis of the results of calculations presented below.

Using the first and third assumptions, together with the conditions of equal static pressures and ($p_3 = p_2$, $p_{3T} = p_{2T}$) and the slopes of the current lines ($\vartheta_2 = \vartheta_3$, $\vartheta_{2T} = \vartheta_{3T}$) on both sides of the tangential discontinuity τ, it is possible to determine the shape of the *TD* region of τ (Fig. 1) upon solving the ordinary differential equation

$$y'(x) = \tan\vartheta \quad (3)$$

with relations (1) and (2). In addition, using the third assumption with a solution of the problem of interaction between the shock wave and a weak discontinuity, it is possible to determine the shape of the curvilinear shock wave *TB* (see [5]). This interaction gives rise to the discontinuity ΔK of the shock wave curvature, the value of which is proportional to the discontinuity ΔN of the current line curvature on the weak discontinuity:

$$\Delta K = \Phi(M, J)\Delta N. \quad (4)$$

The coefficient of proportionality $\Phi(M, J)$ depends on the Mach number M in front of the shock wave and the shock wave intensity *J* at the point of interaction [2].

Recently [5], it was demonstrated that, under the above assumptions, formula (4) leads to the following relationship between the curvature K_{s2} of shock wave *2* and the shock wave intensity J_2, the Mach number M_1 of the flow in front of the shock wave, and the curvature K_ϑ of the current line behind the shock wave:

$$K_{s2} = \Phi(M_1, J_2)K_\vartheta. \quad (5)$$

Here, K_{s2} refers to an arbitrary point *H* of shock wave *2*, and K_ϑ, to the point of intersection of the characteristic H_1H of the first family with the shock wave (Fig. 1). The latter curvature can be expressed through the curvature K_τ of the tangential discontinuity at the point H_1:

$$K_\vartheta = \frac{\chi(\vartheta)}{x_H - x_c},$$
$$x_c = x_{H1} - \frac{\chi(\vartheta)}{K_\tau}, \quad \chi(\vartheta) = -\frac{(1-\varepsilon)(M^2(\vartheta)-1)\cos(\vartheta+\alpha)}{M^3(\vartheta)}, \quad (6)$$

where x_{H1} and x_H are abscissas of the points H_1 and *H*, ϑ is the slope of the current line relative to the abscissa axis, $M(\vartheta)$ is the Mach number of the H_1H characteristic, and $\alpha = \arcsin(1/M)$. As can be readily shown, Eqs. (5) and (6) can be reduced to an ordinary differential equation of the first order with respect to the function $y(x)$ describing the shape of the curvilinear shock wave *2*. The integration has to be performed over the interval $[x_T, x_B]$, with the upper limit being determined from the condition $y_B - y_A = \tan\beta_1 (x_B - x_A)$ (Fig. 1).

The first characteristic *BD* of the centered shock wave *4* is simultaneously the characteristic of the second family of the simple wave *TBD*. Therefore, this characteristic obeys the relation

$$\omega(M_{2D}) + \vartheta_{2D} = \omega(M_{2B}) + \vartheta_{2B},$$

which determines, together with Eqs. (1)–(3), the coordinates of point *D* at which the characteristic *BD* intersects the tangential discontinuity τ. In addition, the characteristic *BD* represents a weak discontinuity for the curvature of the current lines. In particular, point *D* features a break in the curvature of the tangential discontinuity τ. This leads to a change in the curvature sign, whereby the tangential discontinuity to the right of point *D* is convex (Fig. 1).

The results of numerical calculations [3, 4] showed that the angle β_4 of flow rotation in the centered wave *BDF* does not exceed several degrees. Therefore, β_4 can be used as a small parameter for solving the problems of interactions between the simple waves *TBD* and *BDF* and between the wave *BDF* and the tangential discontinuity τ using the method described in [6]. Using this approach, it is easy to obtain an ordinary differential equation describing in the first approximation the shape of the tangential discontinuity τ in the region from point *D* to a point at which the velocity on the lower side of τ reaches the critical value ($M_3 = 1$).

Using the above relations, it is possible to calculate the flow in the case when the height y_T of the Mach disk *3* is given together with M_0 and J_1 (Fig. 1). The Mach disk height is determined by iterations, whereby M_0, J_1, and a certain y_T value are set in each step. Then, the shapes of the shock wave *2* and the tangential discontinuity τ are determined using the algorithm described above. In this way, the tangential discontinuity τ is constructed until one of the conditions $\vartheta_\tau = 0$ or $M_3 = 1$ is fulfilled. In the former case, the height y_T is too large, and in the latter case, it is too small. Taking

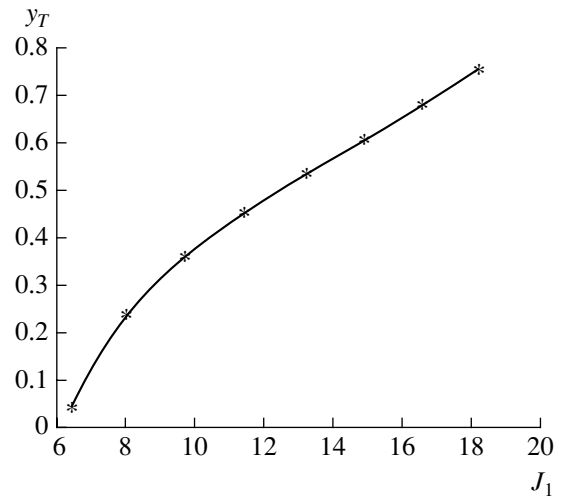

Fig. 2. A comparison of the results of analytical and numerical calculations of the Mach disk height.

into account the conclusions about y_T, the Mach disk height is refined, after which the next iteration is performed. Thus, the task of determining y_T reduces to approaching this value as a boundary in the boundary-value problem.

Figure 2 shows the results of calculation of the Mach disk height for $M_0 = 5$ and various values of J_1. Here, the solid curve is the $y_T(J_1)$ function determined analytically as described above, while asterisks represent the results reported in [3, 4]. As can be seen from these data, the uncertainty of the proposed method does not exceed 0.5%. For comparison, note that the approximate analytical solution to a similar problem of Mach wave reflection in a narrowing channel [7, 8] differed from the experimental and numerical data by 30–40%.

Conclusion. We have proposed a simple analytical model of flow in the first barrel of a plane overexpanded jet of the perfect nonviscous gas outgoing from a profiled nozzle. According to this model, the flow field is calculated by an iterative approach to the boundary condition of a boundary-value problem for a system of ordinary differential equations. The results of calculations show the high precision of the model.

Acknowledgments. This study was supported by the INTAS Foundation, grant no. 99-785.

REFERENCES

1. A. V. Omel'chenko and V. N. Uskov, Izv. Ross. Akad. Nauk, Mekh. Zhidk. Gaza, No. 6, 118 (1995).
2. A. L. Adrianov, A. L. Starykh, and V. N. Uskov, *Interference of Stationary Gasdynamic Discontinuities* (Nauka, Novosibirsk, 1995).
3. V. S. Avduevskiĭ, É. A. Ashratov, and U. G. Pirumov, *Supersonic Nonisobaric Gas Jets* (Mashinostroenie, Moscow, 1985).
4. G. I. Averenkova, É. A. Ashratov, T. G. Volkonskaya, *et al.*, *Supersonic Ideal Gas Jets* (Izd. Mosk. Gos. Univ., Moscow, 1971), Part 2.
5. V. R. Meshkov, A. V. Omel'chenko, and V. N. Uskov, Vestn. S.-Peterb. Univ., Ser. 1, No. 2 (9), 99 (2002).
6. C. C. Lin, J. Math. Phys. **33** (2), 117 (1954).
7. D. J. Azevedo and C. S. Liu, AIAA J. **31**, 83 (1993).
8. H. G. Hornung and M. L. Robinson, J. Fluid Mech. **123**, 155 (1982).

Translated by P. Pozdeev

Technical Physics Letters, Vol. 29, No. 3, 2003, pp. 246–248. Translated from Pis'ma v Zhurnal Tekhnicheskoĭ Fiziki, Vol. 29, No. 6, 2003, pp. 63–68.

Peculiarities of the Impurity Breakdown under Conditions of Transverse Runaway of Hot Electrons

N. K. Metreveli, Z. S. Kachlishvili, F. G. Chumburidze, and L. T. Tskipuri

Tbilisi State University, Tbilisi, Georgia

e-mail: nanametreveli@yahoo.com; faculty@tsu.ge

Received July 15, 2002

Abstract—The phenomenon of impurity breakdown (IB) under conditions of the transverse runaway (TR) of hot electrons is considered. The effect of increasing the degree of compensation on the ratio of the critical IB (E_{IB}) and TR (E_{TR}) fields for various values of the magnetic field is determined. As the magnetic field grows, the two critical values of the electric fields mutually tend to each other. When the degree of compensation increases at a fixed magnetic field strength, the critical IB field approaches the TR threshold field. These results are of interest for studying nonlinear oscillations arising in the vicinity of the E_{IB} and E_{TR} values. *© 2003 MAIK "Nauka/Interperiodica".*

For a system of hot electrons in a magnetic field, it is always important to express the internal field through the applied electric and magnetic fields. Using boundary conditions corresponding to the Hall regime for determining the heating field, we obtain the equation [1]

$$E^2 = E_x^2 + E_y^2 = E_x^2[1 + D^2(E, H, t, s)], \qquad (1)$$

where E_x and E_y are the strengths of the external electric field and the Hall field, respectively;

$$D \equiv \frac{\int_0^\infty x^{\frac{t-s+3}{2}} \exp[-F(x)]dx}{\int_0^\infty x^{\frac{3-s}{2}} \exp[-F(x)]dx}, \quad F(x) = \int_x \frac{dx}{1+\alpha\theta(x)},$$

$$\alpha \equiv \left(\frac{E}{E_0}\right)^2, \quad E_0 \equiv \sqrt{3}\frac{k_0 T}{e(l_0\tilde{l}_0)^{1/2}},$$

$\theta(x) = \frac{x^{\frac{t+s}{2}}}{1+\eta x^t}$ is the heating function; $\eta \equiv \left(\frac{H}{H_0}\right)^2$; H is the applied magnetic field strength, $H_0 \equiv \frac{(2mc^2k_0T)^{1/2}}{el_0}$; t and s are the exponents in the dependences of the electron mean free path on the momentum and energy, respectively: $l(x) = l_0 x^{\frac{t+1}{2}}$, $\tilde{l}(x) = \tilde{l}_0 x^{\frac{s+1}{2}}$; and $x \equiv \frac{\varepsilon}{k_0 T}$ is the dimensionless energy; the other notations are as commonly accepted.

Equation (1) has an analytical solution for the internal field only under the transverse runaway (TR) conditions [2, 3], whereby $t > 0$, $t + s = 2$ (for an arbitrary magnetic field) and $t > 0$, $3t + s = 2$ for a weak magnetic field ($\eta \ll 0.6$). Under the TR conditions, Eq. (1) acquires the form

$$E^2 = \frac{E_x^2}{1 - \Phi\frac{E_x^2}{E^{0^2}}}, \qquad (2)$$

where $\Phi = 1$ for $t + s = 2$, $\Phi = 2.76\eta$ for $3t + s = 2$, $E^0 = \frac{E_0}{\sqrt{t}}\frac{\Gamma\left(\frac{t+3}{2t}\right)}{\Gamma\left(\frac{2t+3}{2t}\right)}$, and Γ is the gamma function. For $E_x \longrightarrow \frac{E^0}{\sqrt{\Phi}} \equiv E_{x,\,TR}$, the heating field strongly increases (i.e., the TR effect takes place).

Let the system contain both shallow and deep impurities. Considering the phenomenon of impurity breakdown (IB) under the TR conditions, we may expect that breakdown from shallow levels will take place before the TR. Obviously, the value of $E_{x,\,TR}$ is independent of the degree of compensation (C_0), whereas the IB critical field ($E_{x,\,IB}$) significantly depends on this value (and tends to infinity as $C_0 \longrightarrow 1$). For $3t + s = 2$, the latter critical field $E_{x,\,TR}$ decreases with increasing magnetic field. In the presence of deep impurity levels, it is evident that (even for $(E_{x,\,IB})_1 > E_{x,\,TR}$) the onset of TR will immediately lead to the IB. This implies that $(E_{x,\,IB})_1$ effectively decreases, so that the density of hot electrons during the TR also exhibits growth.

1063-7850/03/2903-0246$24.00 © 2003 MAIK "Nauka/Interperiodica"

Thus, in the presence of shallow impurities, $E_{x,\,\mathrm{IB}}$ shifts toward $E_{x,\,\mathrm{TR}}$ with an increasing degree of compensation in both cases ($t + s = 2$ and $3t + s = 2$). In the latter case ($3t + s = 2$), the $E_{x,\,\mathrm{IB}}$ and $E_{x,\,\mathrm{TR}}$ values will mutually move toward each other with increasing magnetic field. In the case of deep levels, $(E_{x,\,\mathrm{IB}})_1$ effectively decreases to approach $E_{x,\,\mathrm{TR}}$.

These results are of special interest for studying nonlinear oscillations arising in the vicinity of the E_{IB} and E_{TR} values. Indeed, recent investigations [4] showed that the IB in a compensated semiconductor favors both regular and chaotic oscillations, while the magnetic field plays the role of an external parameter capable of controlling the nonlinear dynamics. On the other hand, we have recently established [5] that the differential conductivity changes sign under the TR conditions changes sign passing through infinity, which implies the possibility of nonlinear autooscillations. The oscillatory instability is usually developed in the vicinity of the critical IB and TR fields. Then, the question naturally arises as to how the character of the oscillatory process will change (under both IB and TR conditions) when the critical fields approach one another as a result of variation of the magnetic field or the degree of compensation. This and related problems are a subject for subsequent research. Here we will establish how the magnetic field and the degree of compensation influence the values of critical fields.

Since we consider the IB under the TR conditions, the $E_{x,\,\mathrm{IB}}$ for both shallow and deep levels has to be determined from Eq. (2). This is evident, because the breakdown is driven by the internal field. Thus, the applied breakdown field is

$$E_{x,\,\mathrm{IB}} = \frac{E_{\mathrm{IB}}}{\sqrt{1 + \Phi\dfrac{E_{\mathrm{IB}}^2}{E^{0^2}}}}. \qquad (3)$$

Using Eq. (2), we obtain an expression for the ratio of the critical IB and TR fields,

$$\frac{E_{x,\,\mathrm{IB}}}{E_{x,\,\mathrm{TR}}} = \frac{1}{\sqrt{1 + \dfrac{\Gamma^2\left(\dfrac{t+3}{2t}\right)}{\Phi(H)\alpha_{\mathrm{IB}}\Gamma^2\left(\dfrac{2t+3}{2t}\right)t}}}, \qquad (4)$$

where $\alpha_{\mathrm{IB}} \equiv \left(\dfrac{E_{\mathrm{IB}}}{E_0}\right)^2$. The values of α_{IB} for various degrees of compensation C_0 is determined from the IB condition (see, e.g., [6]):

$$\frac{C_0}{1 - C_0}\frac{B_T(\alpha_{\mathrm{IB}})}{A_I(\alpha_{\mathrm{IB}})} = 1. \qquad (5)$$

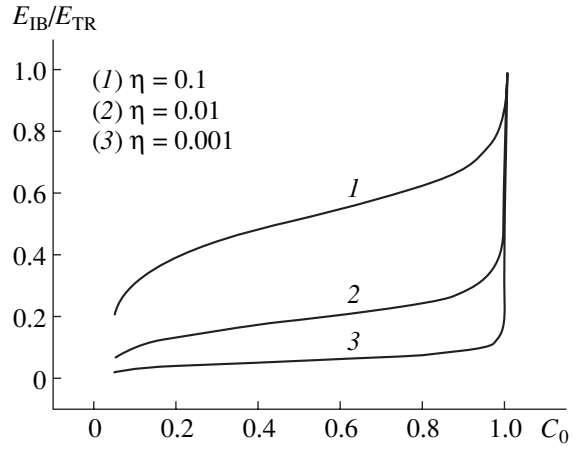

Fig. 1. The plots of $E_{\mathrm{IB}}/E_{\mathrm{TR}}$ versus C_0 for various values of the magnetic field strength in the case of $3t + s = 2$, whereby the momentum is scattered on dipoles ($t = 1$) and the energy is scattered on bending acoustic phonons ($s = -1$) ($T = 20$ K).

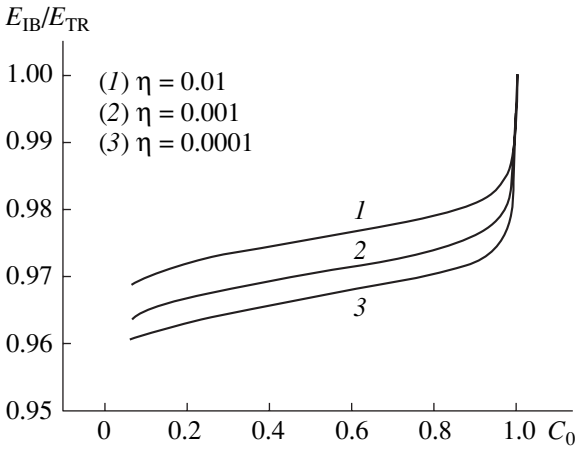

Fig. 2. The plots of $E_{\mathrm{IB}}/E_{\mathrm{TR}}$ versus C_0 for various values of the magnetic field strength in the case of $t + s = 2$, whereby the momentum is scattered on ions ($t = 3$) and the energy is scattered on bending acoustic phonons ($s = -1$) ($T = 20$ K).

Here, $A_I(\alpha_{\mathrm{IB}})$ is the impact ionization coefficient calculated using the differential cross section as determined by Drawin [7] and $B_T(\alpha_{\mathrm{IB}})$ is the recombination coefficient calculated using the effective capture cross section determined [8] using refined Leks theory [9]. It should be emphasized that Eq. (5) gives α_{IB} for every set of the degree of compensation and the magnetic field, after which Eq. (4) yields the corresponding ratio of the critical IB and TR fields.

Figures 1 and 2 show the curves of $E_{\mathrm{IB}}/E_{\mathrm{TR}}$ versus C_0 constructed according to Eq. (4) for $3t + s = 2$ ($t = 1$, $s = -1$) and $t + s = 2$ ($t = 3$, $s = -1$), respectively. As can be seen from these data, the critical IB field tends to a TR threshold field at a rate increasing with the magnetic field.

In conclusion, it should be noted that the above results contradict the well-known fact that the applied breakdown field tends to infinity for $C_0 \longrightarrow 1$. As the degree of compensation increases, the applied breakdown field tends to a TR threshold fields, and (in the $G_0 \longrightarrow 1$ asymptotics) the IB and TR critical fields coincide. Upon merging of these fields, the internal field tends to infinity. This is quite a reasonable behavior, since the real breakdown field in this regime is the internal field. In the presence of deep levels, as soon as the E_x value grows to be on the order of $E_{x,\,\mathrm{TR}}$, the internal field will tend to infinity (i.e., TR takes place), and the IB will take place despite the fact that $(E_{x,\,\mathrm{IB}})_1$ increases with the degree of compensation and deviates from the TR threshold value.

Acknowledgments. This study was supported by the International Scientific-Technological Center, grant no. G-394.

REFERENCES

1. Z. S. Kachlishvili and F. G. Chumburidze, Pis'ma Zh. Tekh. Fiz. **24** (12), 36 (1998) [Tech. Phys. Lett. **24**, 470 (1998)].
2. Z. S. Kachlishvili, Zh. Éksp. Teor. Fiz. **78**, 1955 (1980) [Sov. Phys. JETP **51**, 982 (1980)].
3. Z. S. Kachlishvili and F. G. Chumburidze, Zh. Éksp. Teor. Fiz. **87**, 1834 (1984) [Sov. Phys. JETP **60**, 1055 (1984)].
4. K. M. Jandieri and Z. S. Kachlishvili, Pis'ma Zh. Éksp. Teor. Fiz. **67**, 340 (1998) [JETP Lett. **67**, 358 (1998)]; Fiz. Tekh. Poluprovodn. (St. Petersburg) **35**, 909 (2001) [Semiconductors **35**, 873 (2001)].
5. Z. S. Kachlishvili, N. K. Metreveli, and F. G. Chumburidze, Zh. Tekh. Fiz. **70** (5), 48 (2000) [Tech. Phys. **45**, 571 (2000)].
6. É. I. Zavaritskaya, Trudy Fiz. Inst. Akad. Nauk SSSR **37**, 41 (1966).
7. H. W. Drawin, Z. Phys. **164**, 513 (1961).
8. T. Gegechkori, V. Jakeli, and Z. Kachlishvili, Phys. Status Solidi B **112**, 379 (1982).
9. V. N. Abakumov and I. N. Yassievich, Zh. Éksp. Teor. Fiz. **71**, 657 (1976) [Sov. Phys. JETP **44**, 345 (1976)].

Translated by P. Pozdeev

Technical Physics Letters, Vol. 29, No. 3, 2003, pp. 249–252. Translated from Pis'ma v Zhurnal Tekhnicheskoĭ Fiziki, Vol. 29, No. 6, 2003, pp. 69–75.

The Fundamental Mode Amplitude Buildup in an Oscillating Drop under Internal Nonlinear Resonance Conditions

S. O. Shiryaeva, A. I. Grigor'ev, and D. F. Belonozhko

Yaroslavl State University, Yaroslavl, Russia

e-mail: shir@uniyar.ac.ru

Received September 19, 2002

Abstract—In a liquid drop charged below the critical level for realization of the instability with respect to the intrinsic charge, the fundamental oscillation mode amplitude can grow due to a nonlinear resonance interaction with higher modes. © *2003 MAIK "Nauka/Interperiodica".*

In the context of elucidating the physical mechanisms underlying the lighting discharge initiation in stormy clouds [1, 2], it is of interest to study the possibility of resonance pumping of the fundamental oscillation mode due to its interaction with higher modes in a liquid drop possessing a charge below the critical value according to Rayleigh [3, 4].

Formulation of the problem. Let us consider the time evolution of the shape of a drop of the ideal, incompressible and perfectly conducting liquid with density ρ and surface tension σ. The drop, bearing a total charge of Q and having a volume equal to that of a sphere with radius R, occurs in vacuum. At the initial time $t = 0$, the equilibrium spherical shape of the drop is subject to a virtual axisymmetric perturbation of a certain finite amplitude. The task is to determine the spectrum of capillary oscillations of the drop (i.e., to describe the drop shape) at subsequent times ($t > 0$).

In dimensionless variables such that $R = \sigma = \rho = 1$, the equation describing the drop surface in a spherical coordinate system with the origin placed at the center of mass can be written in the following form: $r(\theta, t) = 1 + \xi(\theta, t)$, where $|\xi| \ll 1$. The problem of the evolution of the drop surface is mathematically formulated as follows:

$$\Delta\psi(\mathbf{r}, t) = 0; \quad \Delta\Phi(\mathbf{r}, t) = 0;$$

$$r \longrightarrow 0: \psi(\mathbf{r}, t) \longrightarrow 0; \quad r \longrightarrow \infty; \quad \Phi(\mathbf{r}, t) \longrightarrow 0;$$

$$r = 1 + \xi(\theta, t): \frac{\partial\xi}{\partial t} = \frac{\partial\psi}{\partial r} - \frac{1}{r^2}\frac{\partial\psi}{\partial\theta}\frac{\partial\xi}{\partial\theta};$$

$$\Delta p - \frac{\partial\psi}{\partial t} - \frac{1}{2}(\nabla\psi)^2 + \frac{1}{8\pi}(\nabla\Phi)^2 = \mathrm{div}\mathbf{n};$$

$$\Phi(r, \theta, t) = \Phi_S(t).$$

This system has to be solved taking into account the conditions of conservation of the total charge and the drop volume and the condition of immobility of the center of mass:

$$-\frac{1}{4\pi}\oint_S(\mathbf{n}\cdot\nabla\Phi)ds = Q,$$

$$S = [r = 1 + \xi(\theta, t), 0 \le \theta \le \pi, 0 \le \varphi \le 2\pi];$$

$$\int_V r^2 dr\sin\theta d\theta d\varphi = \frac{4}{3\pi},$$

$$V = [0 \le r \le 1 + \xi(\theta, t), 0 \le \theta \le \pi, 0 \le \varphi \le 2\pi];$$

$$\int_V \mathbf{e}_r r^3 dr\sin\theta d\theta d\varphi = 0.$$

The initial conditions specify a virtual deformation of the equilibrium spherical shape, with zero initial velocities of all points of the drop surface:

$$t = 0: \xi(\theta) = \xi_0 P_0(\mu) + \xi_1 P_1(\mu) + \varepsilon\sum_{i\in\Xi} h_i P_i(\mu);$$

$$\sum_{i\in\Xi} h_i = 1; \quad \frac{\partial\xi(\theta, t)}{\partial t} = 0.$$

In the above relationships, Ξ is the set of numbers of the initially excited oscillation modes; $\mu \equiv \cos\theta$; Δp is the constant pressure jump between inside and outside of the drop in the equilibrium state; $\mathbf{n}$ is the unit vector of the normal to the drop surface; $\Phi(\mathbf{r}, t)$ and $\psi(\mathbf{r}, t)$ are the potentials of the electric and velocity fields, respectively; $\Phi_S(t)$ is the constant electric potential on the drop surface; ε is the amplitude of the initial perturbation of the drop surface; $P_i(\mu)$ is the Legendre polynomial of the ith order; h_i are coefficients determining the partial contributions of the ith oscillation mode to the

total initial perturbation; and ξ_0 and ξ_1 are constants determined from the conditions of the constant drop volume and the center-of-mass immobility at the initial time.

Problem solution. The above problem can be solved by the asymptotic multiscale method, which yields the following expression describing the time variation of the drop shape:

$$r(\theta, t)1 + \varepsilon\sum_{i\in\Xi} M_i^{(1)}(t)P_i(\mu) + \varepsilon^2\sum_{n=0}^{\infty} M_n^{(2)}(t)P_n(\mu) + O(\varepsilon^3);$$

$$M_i^{(1)}(t) = h_i\cos(\omega_i t);$$

$$M_0^{(2)})(t) = -\frac{1}{2}\sum_{i\in\Xi}\frac{h_i}{(2i+1)}(1+\cos(2\omega_i t));$$

$$M_1^{(2)}(t) = -\sum_{i\in\Xi}\frac{9ih_{i-1}h_i}{(2i-1)(2i+1)}\cos(\omega_i t)\cos(\omega_{i-1}t);$$

$$M_n^{(2)}(t) = [N_n(t) - N_n(0)\cos(\omega_n t)]; \quad n \ge 2;$$

$$N_n(t) = \frac{1}{2}\sum_{i,j\in\Xi} h_i h_j[\lambda_{ijn}^{(+)}\cos((\omega_i+\omega_j)t) + \lambda_{ijn}^{(-)}\cos((\omega_i-\omega_j)t)];$$

$$\omega_n^2 = n(n-1)[(n+2) - W]; \quad W = \frac{Q^2}{4\pi};$$

$$\lambda_{ijn}^{(\pm)} = [\gamma_{ijn} \pm \omega_i\omega_j\eta_{ijn}][\omega_n^2 - (\omega_i \pm \omega_j)^2]^{-1};$$

$$\gamma_{ijn} = K_{ijn}\left[\omega_i^2(n-i+1) + 2n[j(j+1)-1] + [j(i+1) - i(2i-2n+7)+3]n\frac{W}{2}\right] + \alpha_{ijn}\left[\frac{1}{i}\omega_i^2 + n\frac{W}{2}\right];$$

$$\eta_{ijn} = K_{ijn}\left(\frac{n}{2} - i + 1\right) + \alpha_{ijn}\frac{1}{i}\left(1 + \frac{n}{2j}\right);$$

$$K_{ijn} = [C_{i0j0}^{n0}]^2; \quad \alpha_{ijn} = -\sqrt{i(i+1)j(j+1)}C_{i0j0}^{n0}C_{i(-1)j1}^{n0};$$

where C_{i0j0}^{n0} and $C_{i(-1)j1}^{n0}$ are the Clebsch–Gordan coefficients [5].

As can be seen from the expressions for $\lambda_{ijn}^{(\pm)}$, when the frequencies of modes with the numbers i, j, n obey one of the relations

$$\omega_n^2 - (\omega_i \pm \omega_j)^2 = 0, \qquad (1)$$

the expression for the nth mode amplitude $M_n^{(2)}(t)$ contains a small denominator. This is just what reflects the resonance energy exchange between modes with the numbers i, j, and n. Note that i and j are the numbers of modes forming the initial perturbation of the equilibrium spherical drop, while n is the number of a mode excited in the second order of smallness due to the mode interaction.

Analysis of the solution. For the frequencies ω_n determined by Eq. (1) for a charged drop of an ideal liquid with subcritical values of the parameter W, there are no combinations of the ith and jth modes capable of exciting a resonance of the fundamental mode ($n = 2$), although the third, fourth, and other low-number modes exhibit resonance pumping.

Resonance pumping of the fundamental mode can be achieved if we take into account that the oscillation frequencies of a real drop are influenced by the liquid viscosity, which can lead to a decrease in these frequencies under certain conditions. The problem of nonlinear oscillations of a viscous drop is extremely difficult and cannot be strictly solved at present. For a qualitative analysis of the situation, we will use the resonance relation (1) and the well-known dispersion equation [6, 7] describing the capillary oscillations of a charged viscous drop. This equation has two pairs of complex-con-

Tables 1–4. Mode numbers (i and j) and the values of parameter W providing for a resonance pumping of the fundamental oscillation mode of a charged liquid drop with various values of the dimensionless viscosity ν

Table 1

ν = 0.04		
i	j	W
84	86	0.72
85	87	1.70
86	88	2.46
87	89	3.03
97	95	3.29
98	96	2.95
99	97	2.54
100	98	2.08
101	99	1.56
102	100	0.99
103	101	0.37

Table 2

ν = 0.06		
i	j	W
35	37	1.30
36	38	2.62
44	42	3.10
45	43	2.57
46	44	1.93
47	45	1.20
48	46	0.37

Table 3

ν = 0.1		
i	j	W
16	14	3.12
17	15	2.41
18	16	1.48
19	17	0.36

Table 4

ν = 0.2		
i	j	W
5	3	1.75
6	4	0.29

jugate solutions differing by the signs of frequencies, which can be readily obtained using a computer program package for analytical calculations (of the MATHEMATICA type).

In what follows, we employ the solution with a negative real part (describing the decay of oscillations) and positive imaginary part (determining the frequencies of oscillations). The solutions to the dispersion equation are determined on a three-sheet Riemann surface, since they involve a cubic root of imaginary unity (possessing three complex values). Our analysis refers to the sheet on which $\sqrt[3]{-1} = -1$. Finally, in the low-viscosity approximation ($\nu \ll 1$, ν being the dimensionless kinematic viscosity), we obtain an expression describing the frequency of oscillations with a correction for the viscosity:

$$\omega_n = \sqrt{n(n-1)[(n+2)-W]} \times\left[1-\frac{(n-1)[13+4n(5+2n)]}{2n(2+n-W)}\nu^2\right].$$

Substituting this expression into Eq. (1), we can determine the modes capable of providing the required resonance interaction.

Tables 1–4 show the results of calculations for various values of the dimensionless viscosity ν, corresponding to the conditions under which the interaction of higher ith and jth modes leads to a resonance buildup of the fundamental mode amplitude. The third columns give the values of the parameter W providing for the given resonance. It should be recalled that the critical value of this parameter corresponding to the instability of a spherical charged drop with respect to the intrinsic charge is $W = 4$. As can be seen from the data in the tables, there are many possibilities for resonance pumping of the fundamental mode even for values of W one order below the critical level. This circumstance is grounds for optimism from the standpoint of the possibility of realization of the conditions for lightning discharge initiation as a result of a crown discharge in the vicinity of a large drop falling freely in a storm cloud [1, 2]. Indeed, charges of a sufficiently large magnitude have already been observed in experiments performed under natural conditions [8]. It should be noted that a

crown discharge can be initiated in the vicinity of a large drop acquiring an elongated shape as a result of the fundamental mode excitation. This can take place even at a value of W significantly below the critical level, owing to an increase in the electric field strength at the drop vertex resulting from the redistribution of charge [1, 9–11]. The excitation of high oscillation modes in a large (R = 0.1–2.5 mm) drop falling freely in a storm cloud can result from its collisions with smaller drops (R = 4–15 μm) accounting for the maximum fraction of drops in a cloud [8].

The above approach, while not quite correct, can be justified by the following circumstance. For a resonance interaction of the capillary-gravitational waves, the position of the resonance of the intramodal interaction is independent of the presence of viscosity and is the same for both ideal [12] and viscous [13] liquids.

Conclusion. Nonlinear resonance pumping of the fundamental oscillation mode of a charged liquid drop by the excited higher modes can take place even at values of intrinsic charge significantly below the critical level (in the sense of linear stability).

Acknowledgments. This study was supported by Presidential Grant No. 00-15-9925.

REFERENCES

1. V. A. Dyachuk and V. M. Muchnik, Dokl. Akad. Nauk SSSR **248**, 60 (1979).
2. A. I. Grigor'ev and S. O. Shiryaeva, Phys. Scripta **54**, 660 (1996).
3. J. A. Tsamopoulos and R. A. Brown, J. Fluid Mech. **147**, 373 (1984).
4. S. O. Shiryaeva, Izv. Ross. Akad. Nauk, Mekh. Zhidk. Gaza, No. 3, 163 (2001).
5. D. A. Varshalovich, A. N. Moskalev, and V. K. Khersonskiĭ, *Quantum Theory of Angular Momentum* (Nauka, Leningrad, 1975; World Scientific, Singapore, 1988).
6. A. I. Grigor'ev and A. É. Lazaryants, Izv. Akad. Nauk SSSR, No. 5, 11 (1991).
7. S. O. Shiryaeva, M. I. Munichev, and A. I. Grigor'ev, Zh. Tekh. Fiz. **66** (7), 1 (1996) [Tech. Phys. **41**, 635 (1996)].
8. *Clouds and Cloudy Atmosphere (A Handbook)*, Ed. by I. P. Mazin, A. Kh. Khrgian, and I. M. Imyanitov, (Gidrometeoizdat, Leningrad, 1989).
9. A. I. Grigor'ev and S. O. Shiryaeva, Zh. Tekh. Fiz. **61** (3), 19 (1991) [Sov. Phys. Tech. Phys. **36**, 258 (1991)].
10. S. I. Shchukin and A. I. Grigor'ev, Zh. Tekh. Fiz. **69** (8), 49 (1999) [Tech. Phys. **44**, 913 (1999)].
11. A. N. Zharov, S. O. Shiryaeva, and A. I. Grigor'ev, Zh. Tekh. Fiz. **69** (12), 26 (1999) [Tech. Phys. **44**, 1420 (1999)].
12. A. H. Nayfeh, J. Fluid Mech. **48**, 385 (1971).
13. D. F. Belonozhko, A. I. Grigor'ev, and S. O. Shiryaeva, Pis'ma Zh. Tekh. Fiz. **28** (19), 1 (2002) [Tech. Phys. Lett. **28**, 795 (2002)].

Translated by P. Pozdeev

Technical Physics Letters, Vol. 29, No. 3, 2003, pp. 253–255. Translated from Pis'ma v Zhurnal Tekhnicheskoĭ Fiziki, Vol. 29, No. 6, 2003, pp. 76–81.

Photothermoelectric Converters of Concentrated Radiation

A. M. Kasymakhunova and M. Nabiev

Fergana Polytechnical Institute, Fergana, Uzbekistan
Fergana State University, Fergana, Uzbekistan

Received October 15, 2002

Abstract—Photothermoelectric converters (PTECs) are proposed for the energy supply of low-power-consumption devices. The photoelectric units of PTECs employ high-efficiency solar cells based on the *p*-$Al_xGa_{1-x}As$–*n*-GaAs heterosystem. The thermoelectric units employ a ternary alloy of the *n*-BiTeSe–*p*-BiTeSb type. A new PTEC with a two-stage photoelectric unit, which offers a higher efficiency as compared to a device with a single-stage photocell, is developed. © *2003 MAIK "Nauka/Interperiodica".*

Rapid progress in photoelectric cell technology has led to the appearance of autonomous power supply sources meeting high primary conversion requirements, including high sensitivity, fast response, reliability, portable design, ecological safety, and virtually unlimited working life. From both theoretical and experimental standpoints, it is of interest to study solar energy converters combined with other devices [1, 2]. This can provide for a more effective use of radiant energy and lead to the development of systems possessing higher conversion coefficients.

Existing photothermoelectric converters (PTECs) include the following main parts [3]: (i) a photoelectric cell (photocell), (ii) a thermoelectric cell (thermocell), and (iii) a spacer isolating the rear side of the photocell from the hot junctions of the thermocell. Photocells intended for operation under the conditions of concentrated radiation are additionally provided with cooling systems. In practice, the role of cooling agent is most frequently performed by water. PTECs operate as follows. A radiant flux (light) incident onto a photocell is partly directly converted into electric energy as determined by the efficiency η_{ph}, while the remainder of the radiant energy, converted into heat, is transferred via electrically insulating but thermally conducting ceramic spacer to the hot junctions of the thermocell. As a result of the temperature difference between the hot (T_1) and cold (T_2) junctions, the heat transferred to the thermocell T_1 is also partly converted into electric energy with an efficiency of η_{th}.

In order to increase the PTEC efficiency, we employed highly effective heterophotocells based on $Al_xGa_{1-x}As$–GaAs semiconductor heterostructures [4] and silicon-based solar cells. The maximum efficiency was achieved in a system employing a two-stage photoelectric converter [5]. Based on this principle, we have developed a device intended for charging car batteries. This PTEC-based device, called an autonomous charging unit (ACU), is capable of generating a current of up to 8 A.

PTECs implementing photocells based on semiconductor heterostructures of the *p*-$Al_xGa_{1-x}As$–*n*-GaAs type were fabricated using technology [4] based on the molecular beam epitaxy technique. The substrates represent *n*-GaAs doped with tellurium up to (4–5) × 10^{17} cm^{-3}. The epitaxial layer of a zinc-doped *p*-$Al_xGa_{1-x}As$ solid solution has a thickness of 1.5 μm and a carrier density of ~5×10^{18} cm^{-3} (at an AlAs content of ~50 mol %). Depending on the composition, the semiconductor bandgap varies from 1.87 to 2.1 eV. The *n*-GaAs substrate is provided with a continuous ohmic contact, while the illuminated side of the *p*-$Al_xGa_{1-x}As$ film bears 1-μm-wide strip ohmic contacts. The working area of each photocell is 1.0– 2.0 cm^2.

Similarly to the system described in [4], radiation with a quantum energy below the bandgap width (Eg_2) of the solid solution passed through this layer virtually without absorption to reach the narrow-bandgap (Eg_1) *n*-GaAs substrate. Apparently, a part of this radiation with the energy exceeding Eg_1 was absorbed in the substrate to generate electron–hole pairs separated by the field in the *p*–*n* junction. The effective operation of such converters is explained by the increase in the region of maximum spectral sensitivity as a result of the carrier regeneration immediately in the *p*–*n* junction region. The value of the separation coefficient *Q* in the interval of quantum energies from 1.5 to 2.0 eV is close to unity, which is evidence of negligibly small losses related to the recombination of charge carriers at the heterojunction and in the bulk before separation. For this reason, the spectral sensitivity exhibits only a slight decrease in the 1.5–2.0 eV photon energy interval.

The thermoelectric unit of the PTEC is based on a ternary semiconductor alloy of the *n*-BiTeSe–*p*-BiTeSb

1063-7850/03/2903-0253$24.00 © 2003 MAIK "Nauka/Interperiodica"

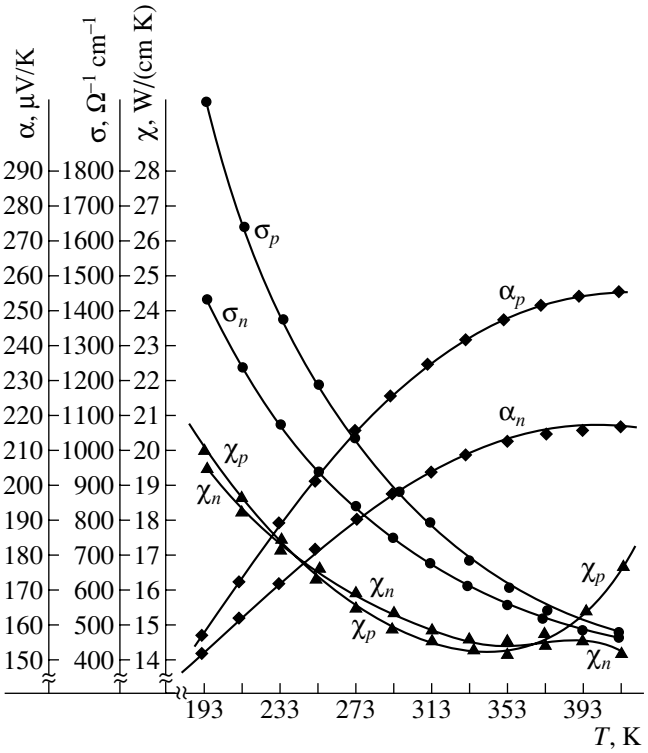

Fig. 1. Temperature variation of the main parameters of positive (α_p, σ_p, χ_p) and negative (α_n, σ_n, χ_n) branches of thermoelectric converters.

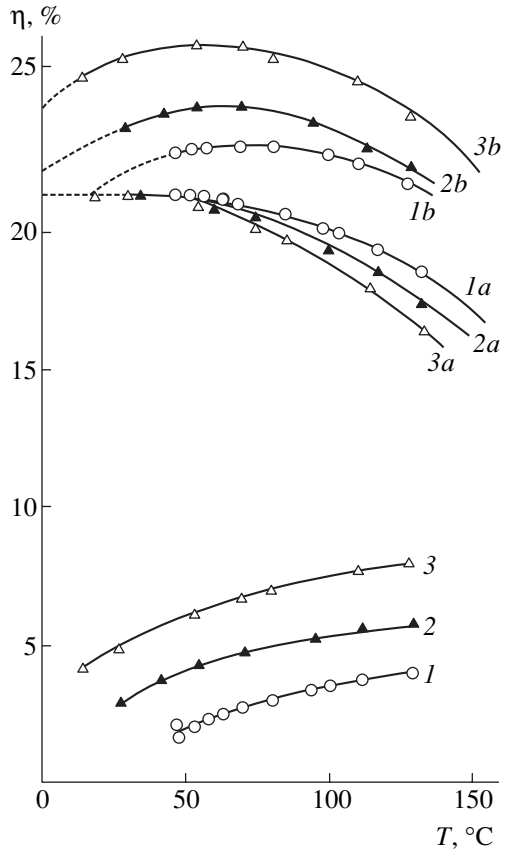

Fig. 2. Plots of the (*1*, *2*, *3*) conversion efficiency of the thermoelectric converter and (*1b*, *2b*, *3b*) overall efficiency of PTEC with two-stage photocell versus hot junction temperature T_1 and (*1a*, *2a*, *3a*) conversion efficiency of photocell versus its temperature for the cold junction temperature T_2 = +20°C (*1*, *1a*, *1b*), –20°C (*2*, *2a*, *2b*), and –60°C (*3*, *3a*, *3b*).

system obtained by zone melting [6]. These alloys possess a high thermoelectric quality factor ($Z \sim 3 \times 10^{-3}$ K^{-1}). The height of the thermocell branches was 1.4 mm; the elements were cut into halves with an electric erosion tool. Figure 1 illustrates the thermoelectric properties of BiTeSe and BiTeSb elements used in the positive and negative branches of thermocells, respectively. In the temperature interval from 20 to 150°C, this alloy system provided for an average thermoelectric quality factor of $Z \sim 2.7 \times 10^{-3}$ K^{-1}.

The results of experimental investigations of the electric and thermal characteristics of thermocells with dimensions $4 \times 4 \times 0.14$ cm showed that a decrease in the height of thermocell branches leads to an increase in the working current and in the thermal flux supplied from hot junctions. Since ACU was intended for operation under the conditions of concentrated radiation, the system is provided with effective heat removal.

The field of concentrated radiation incident onto the working surface of the PTEC was photometrically evaluated. The effective area of this surface is virtually equal to the total area of photocells (~240 cm^2) employed in the PTEC. The light intensity factor was about 20. The laboratory and field tests of ACU showed the following performance characteristics: voltage, 12 V; working current, up to 8 A; overall dimensions, $160 \times 160 \times 15$ mm; mass, ≤0.5 kg.

In addition, we developed a PTEC possessing maximum efficiency (Fig. 2) [5]. This device differs from that described above in that the single-stage photoelectric unit is replaced by a two-stage converter. The temperature dependence of the photoconversion efficiency η_{ph} measured in the field tests shows that η_{ph} first slowly (with a temperature coefficient of $\delta = 0.01\%$) and then more rapidly ($\delta = 0.03\%$) drops. However, this drop is compensated by an increase in the efficiency of thermoelectric conversion. The lower the temperature of the cold thermocell junction, the higher the total efficiency of the PTEC. The difference between the temperature of the photocell and that of the hot junction of the thermocell does not exceed 2–3 K (Fig. 2).

On the whole, the proposed PTECs employing highly effective photo and thermoelectric converters offer a convenient means of energy supply for low-power-consumption devices removed far from electric

mains and other traditional power sources. The proposed devices are advantageous to simple photoelectric cells employed in the existing low-power supply sources for home appliances and remote transducers.

REFERENCES

1. M. M. Koltun and I. P. Gavrilova, Geliotekhnika, No. 1, 3 (1978).
2. A. B. Adamovich and V. A. Gorshenin, RF Patent Application No. 95113632 (27.08.1997).
3. E. Iordanishivili, A. M. Kasymakhunova, and Kh. U. Gafurov, Geliotekhnika, No. 1, 14 (1985).
4. Zh. I. Alferov, V. M. Andreev, M. B. Kagan, *et al.*, Fiz. Tekh. Poluprovodn. (Leningrad) **4**, 2378 (1970) [Sov. Phys. Semicond. **4**, 2047 (1970)].
5. T. K. Zhabborov, A. M. Kasymakhunova, Kh. Olimov, and A. Kamolov, Patent Application of Republic of Uzbekistan, IDP 2002 04 14 (04. 07. 2002).
6. B. M. Gol'tsman, V. A. Kudinov, and I. A. Smirnov, *Semiconductor Thermoelectric Materials Based on* Bi_2Te_3 (Nauka, Moscow, 1972).

Translated by P. Pozdeev

Technical Physics Letters, Vol. 29, No. 3, 2003, pp. 256–258. Translated from Pis'ma v Zhurnal Tekhnicheskoĭ Fiziki, Vol. 29, No. 6, 2003, pp. 82–86.

Stochastic Resonance in an Asymmetric Bistable System

O. V. Gerashchenko

St. Petersburg Institute of Nuclear Physics, Russian Academy of Sciences, Gatchina, Leningrad oblast, Russia

e-mail: gerashch@pnpi.spb.ru

Received October 22, 2002

Abstract—The phenomenon of stochastic resonance in a simple bistable stochastic system, representing an overdamped Kramers oscillator featuring white noise and a periodic rectangular signal with a constant component, has been studied theoretically and using an analog model. An increase in the constant component, determining a static asymmetry of the potential, leads to a decrease in the signal to noise ratio as compared to the symmetric case. © *2003 MAIK "Nauka/Interperiodica".*

As is known, adding noise of an optimum intensity to a useful signal passing through a nonlinear system can improve the data transmission, this phenomenon being known as stochastic resonance [1, 2]. This letter reports on a theoretical and experimental investigation of stochastic resonance in a bistable (double-potential-well) dynamic system representing an overdamped Kramers oscillator with a periodic rectangular signal containing white noise and a constant component. Selecting a rectangular signal allows the problem to be solved for an arbitrary signal amplitude without being restricted to perturbation theory.

Consider the equation of an overdamped Kramers oscillator:

$$\frac{dx}{dt} = -\frac{\partial U_0(x)}{\partial x} + F + \sigma\xi(t) + AR(t),$$

$$U_0(x) = -\frac{a}{2}x^2 + \frac{b}{4}x^3, \quad \langle\xi(t)\xi(t')\rangle = \delta(t-t'), \quad (1)$$

$$\delta U_0 = U_0(0) - U_0(x_0) = \frac{a^2}{4b}, \quad \pm x_0 = \pm\sqrt{\frac{a}{b}},$$

where $\xi(t)$ is the white noise, $R(t) = \pm 1$ is the periodic rectangular signal with a period T, $\pm x_0$ are the stable points of the unperturbed system, and a, b, F, σ, and A are constant parameters. Denoting by τ the correlation time of the (real) white noise and assuming that $a \sim b$, we adopt the following hierarchy of characteristic times in the system under consideration:

$$T \gg w_0^{-1} \gg a^{-1} \gg \tau \longrightarrow 0;$$
$$w_0 = \frac{a}{\pi/2}\exp\left(-\frac{a^2}{2b\sigma^2}\right). \quad (2)$$

Here, w_0 is the characteristic frequency of switching under the action of white noise. If the intensity of external action is lower than the barrier height δU_0, $x(t)$ can be approximated by a dichotomic signal: $x(t) = x_0 d(t)$, $d(t) = \pm 1$. Thus, we deal with a two-state model system. In the Kramers approximation, the time- dependent probability of transitions between states is

$$\alpha_\mp = w_{\mp 1 \to \pm 1} = w_0 \exp[\pm p \pm \nu R(t)],$$
$$p = \frac{2x_0 F}{\sigma^2}, \quad \nu = \frac{2x_0 A}{\sigma^2}, \quad (3)$$

and the control equation for the probability distribution density of the nonstationary process can be written as

$$\frac{dP(\pm 1, t)}{dt} = \alpha_\mp(t)P(\mp 1, t) - \alpha_\pm(t)P(\pm 1, t). \quad (4)$$

Let us consider the behavior of $x(t)$ for large times ($t \sim T$), whereby the white-noise-induced transitions can be considered as uncorrelated. Taking into account the formula

$$f[AR(t)] = \frac{1}{2}[f(A) + f(-A) + R(t)(f(A) - F(-A))], \quad (5)$$

which is valid for an arbitrary function f, we obtain the following expression for the correlation function [3]:

$$K(t) = C\delta(t) + B_2\langle R(0)R(t)\rangle,$$

$$C = S(0) = \frac{x_0^2}{2w_0}(\cosh^{-3}(p+\nu) + \cosh^{-3}(p-\nu)), \quad (6)$$
$$B_2 = \frac{x_0^2}{4}(\tanh(p+\nu) - \tanh(p-\nu))^2,$$

$$S(\omega) = C + \frac{8}{\pi}B_2\sum_k \frac{\delta(\omega - (2k+1)\Omega)}{(2k+1)^2}.$$

1063-7850/03/2903-0256$24.00

For $v \ll 1$, this yields

$$C = \frac{x_0^2}{w_0 \cosh^3(p)}, \quad B_2 = \frac{x_0^2 v^2}{\cosh^4(p)}, \qquad SNR = \frac{8}{\pi}\frac{B_2}{C} = \frac{8 w_0 v^2}{\pi \cosh(p)}. \tag{7}$$

To check these results, the stochastic system was modeled by an analog bistable nonlinear electronic circuit. Since the above results indicate that the only important features of the potential $U_0(x)$ are the presence of one unstable point and two stable states, the consideration was restricted to an overdamped oscillator with a piecewise linear current–voltage characteristic $I(x)$ (Fig. 1) analogous to that studied previously [4, 5]. The scheme in Fig. 1 is described by the equations

$$RC\frac{dx}{dt} = -(x + RI_N(x)) + V(t) = -RI(x) + V(t), \qquad V(t) = F + AR(t) + \sigma\xi(t), \tag{8}$$

where $V(t)$ is the applied voltage, $I_N(x)$ and $I(x)$ are the current–voltage characteristics of the nonlinear element and the whole circuit, respectively, and $x(t)$ is the time variation of the voltage. Introducing dimensionless time ($t \longrightarrow t/RC$), we obtain the corresponding equation fully analogous to Eq. (1). Using the current–voltage characteristic, we can determine the values of $x_1 \approx 2.4$ V, $x_0 \approx 2x_1 \approx 4.7$ V, and the potential barrier (expressed in units of voltage) $dU_0 \approx 11$ V^2. The total voltage $V(t)$ in the circuit represents a sum of the Gaussian noise $\xi(t)$ (physical white noise) with the correlation frequency $1/2\pi\tau \approx 30$ kHz (which is greater than all other characteristic frequencies in the system under consideration), and a periodic rectangular signal with the amplitude A and the frequency $f_s = \Omega/2\pi = 3$ Hz. The inverse relaxation time of the nonlinear system is $1/2\pi RC \approx 1400$ Hz. By changing the Gaussian noise intensity, it was possible to control the frequency w_0 of switching between the two stable states of the system.

The spectral power density of the output signal $x(t)$ at zero frequency, $S(0)$, and that at the frequency of the rectangular signal, $S(f_s = \Omega/2\pi = 3\ \text{Hz}) = B_2/\Delta f$, where $\Delta f = 0.16$ Hz is the frequency discretization step during the spectral measurements, were measured in experiment. Figure 2 shows the signal to noise ratio (SNR)

$$SNR = \frac{8}{\pi}\frac{B_2}{C} = \frac{8}{\pi}\frac{S(f_s)\Delta f}{S(0)}, \tag{9}$$

plotted by these data as a function of the constant bias voltage F.

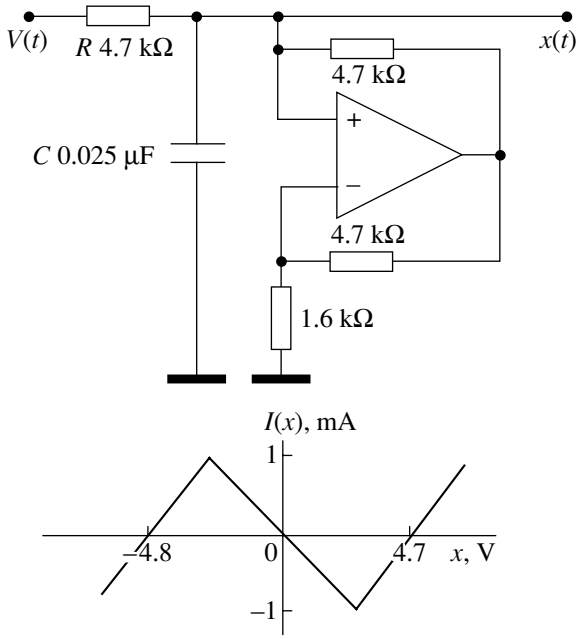

Fig. 1. Schematic diagram and current–voltage characteristic of the analog model of an overdamped oscillator: $V(t)$ is the applied voltage representing a sum of the periodic rectangular signal, constant bias, and white noise; $x(t)$ is the output signal studied.

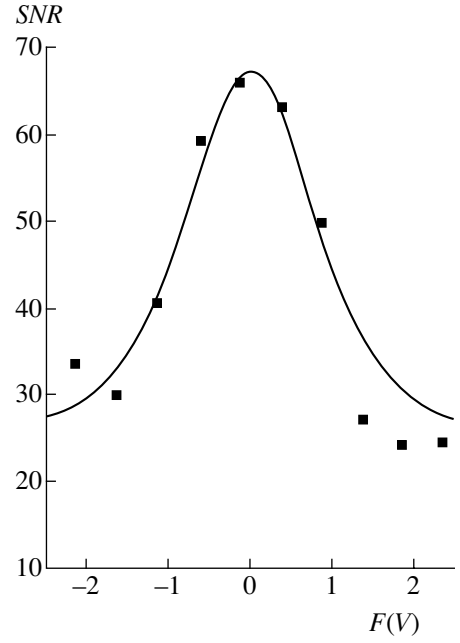

Fig. 2. A plot of the signal to noise ratio (SNR) versus bias voltage F: solid curve is calculated by Eq. (9) fit to the experimental values of parameters; points represent the experimental data.

Thus, a bistable (double-potential-well) nonlinear system featuring white noise and a static asymmetry of the signal (constant bias) has been theoretically studied and experimentally modeled. It is established that a

constant signal component, accounting for the asymmetry in the potential energy, decreases the signal to noise ratio.

Acknowledgments. This study was supported by the Russian Foundation for Basic Research (project no. 02-02-16979) and by the Federal Programs "Quantum Macrophysics" and "Investigation of Collective and Quantum Effects in Condensed Media."

REFERENCES

1. L. Gammaitoni, P. Hanggi, P. Jung, and F. Marchesoni, Rev. Mod. Phys. **70**, 223 (1998).
2. V. S. Anishchenko, A. V. Neiman, F. Moss, and L. Shimansky-Geier, Usp. Fiz. Nauk **169**, 7 (1999) [Phys. Usp. **42**, 7 (1999)].
3. S. L. Ginzburg and M. A. Pustovoit, Phys. Rev. E **66**, 021107 (2002).
4. O. V. Gerashchenko, Zh. Éksp. Teor. Fiz. **116**, 1477 (1999) [JETP **89**, 797 (1999)].
5. O. V. Gerashchenko, S. L. Ginzburg, and M. A. Pustovoit, Eur. Phys. J. B **19**, 101 (2001).

Translated by P. Pozdeev

Technical Physics Letters, Vol. 29, No. 3, 2003, pp. 259–261. Translated from Pis'ma v Zhurnal Tekhnicheskoĭ Fiziki, Vol. 29, No. 6, 2003, pp. 87–94.

Pulsed 5-GW Resonance Relativistic BWT for a Decimeter Wavelength Range

S. A. Kitsanov, A. I. Klimov, S. D. Korovin, I. K. Kurkan, I. V. Pegel', and S. D. Polevin

Institute of High-Current Electronics, Siberian Division, Russian Academy of Sciences, Tomsk, Russia

e-mail: polevin@lfe.hcei.tsc.ru

Received October 8, 2002

Abstract—The results of numerical modeling and experimental investigation of a high-power, resonance relativistic backward wave tube are presented. By using the working TM_{01} mode reflections from the ends of the electrodynamic system, optimum conditions for the electron beam interaction with both the (–1)st harmonic of the backward electromagnetic wave and the main harmonic of the concurrent wave are achieved. A single mode generation with 5 GW output power and a 30% efficiency was obtained in experiments at a frequency of 3.6 GHz. The working frequency can be controlled within 15% (at the half maximum power level) by changing the slow-wave structure period at the constant electron beam parameters. *© 2003 MAIK "Nauka/Interperiodica".*

Presently, the relativistic backward wave tube (BWT) is among the most effective coherent radiation sources capable of operating on a gigawatt power level in the centimeter wavelength range [1, 2]. This system readily adapts to variable electron beam parameters, attains the working regime in a short time, and exhibits a narrow output radiation spectrum. The electrodynamic system of a BWT is relatively simple and characterized by a high electric strength. Unfortunately, the usual relativistic BWT, in which the electron beam interacts with the (–1)st harmonic, is characterized by a small efficiency not exceeding 15–20% for an electron energy of 0.5–1 MeV [3]. The optimum length of the interaction space in this case amounts to $L_{ins} \approx (5–9)\lambda$, where λ is the radiation length.

In real BWTs, the output radiation is usually extracted toward the collector. This is accomplished by using a reflecting below-cutoff waveguide section on the cathode side of a slow-wave structure (SWS), which results in the appearance of a concurrent wave in the interaction space. Both numerical and experimental results [4, 5] showed that the influence of the concurrent wave on the energy pumping process in a relatively short interaction space becomes significant as a result of the monotron effect [6], when the electron flight angle in the concurrent wave amounts to

$$\theta_{tr} = kL\left(\frac{1}{\beta_e} - \frac{1}{\beta_{ph}}\right) \approx \frac{5}{2}\pi. \quad (1)$$

Here, $k = 2\pi/\lambda$ is the wavenumber, $c\beta_e$ is the electron velocity, and $c\beta_{ph}$ is the phase velocity of the main harmonic of the concurrent wave. In this case, the generation efficiency depends on the amplitude ratio and the phase difference between the (–1)st harmonic of the backward wave and the main harmonic of the concurrent wave, as well as on the interaction space length.

Levush *et al.* [7] theoretically studied the effect of reflections from the SWS ends on the relativistic BWT operation, but they ignored the concurrent wave and took into account only the electron beam interaction with the (–1)st harmonic of the backward wave. As a result, the resonance BWT efficiency in the single-mode regime did not exceed 20%.

Below, we present the results of numerical modeling and experimental investigation of a high-power, resonance relativistic BWT with allowance for the electron beam interaction with both backward and concurrent electromagnetic waves. The study aimed at increasing the generation efficiency and output power and reducing the device length, which is especially important for the development of oscillators operating in the decimeter wavelength range.

Figure 1 shows a schematic diagram of the resonance relativistic BWT design. The electron beam, generated in a magnetically isolated coaxial vacuum diode,

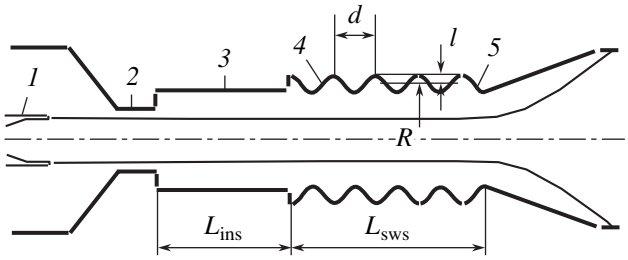

Fig. 1. Schematic diagram of a resonance BWT oscillator: (*1*) cathode; (*2*) below-cutoff section; (*3*) smooth waveguide insert; (*4*) slow-wave structure; (*5*) output reflector.

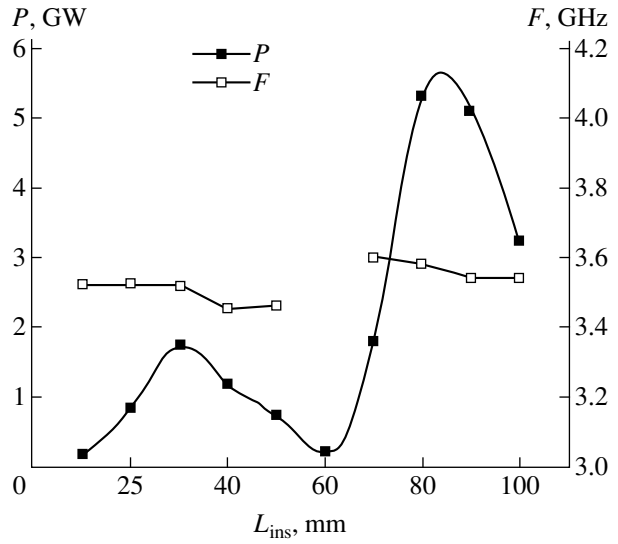

Fig. 2. Plots of the output radiation power and working frequency versus length of the waveguide insert between the below-cutoff section and the SWS (d = 45 mm, H = 20 kOe).

was injected into the electrodynamic system via a below-cutoff waveguide section, which ensures reflection of the backward wave toward the collector. The electrons were emitted from an explosive-emission graphite cylindrical cathode. The RF field distribution was improved, and the optimum conditions for the electron beam interaction with both the (–1)st harmonic of the backward electromagnetic wave and the main harmonic of the concurrent wave were achieved by using partial reflection of the working TM_{01} mode from the collector end of the SWS. The reflection was achieved through reduction in the mean SWS radius and allowed the Q value of SWS to be controlled. A smooth cylindrical waveguide section between the below-cutoff section and the SWS was used for adjusting the optimum phase shift between the main harmonic of the concurrent wave and the (–1)st harmonic of the backward wave. The ratio of the harmonic amplitudes on the electron beam trajectory was determined by the SWS corrugation depth. The impedance of the vacuum diode was controlled by varying the gap between cathode and anode. A focusing magnetic field with a strength of up to 30 kOe was generated by a pulse coil.

The BWT geometry was optimized using the numerical particle-in-cell PIC-code KARAT [8]. The modeling was performed with a magnetically isolated electron diode, to which the voltage was applied in the form of a TEM wave via a coaxial line. The SWS length was selected taking into account formula (1) and was varied within $L_{sws} = (2–4)\lambda$. The results of modeling showed that the optimum geometry of the electrodynamic system corresponds to $L_{sws} \approx 2.5\lambda$, $L_{ins} \approx \lambda$, $l \approx \lambda/8$, $R \approx \lambda/2$, $d \approx \lambda/2$, $Q \approx 100$, and $R_b/R \approx 0.7$. For this geometry, the BWT efficiency amounts to ~30% and only slightly varies in a broad range of the electron beam power (5–20 GW). The optimum impedance of the vacuum diode is about 90 Ω, and the microwave oscillation rise time is about 20 ns.

It was found that variation of the length of the smooth cylindrical waveguide insert between the below-cutoff section and the SWS is accompanied by periodic jumplike changes in the longitudinal standing wave ratio. The number of field variations along the electrodynamic system changed from two to six. The jumps were accompanied by multimode generation and a significant drop in the output power. For the same value of the longitudinal standing wave ratio, the frequency variation was 3–4%.

We also studied the possibility of controlling the working frequency of a resonance BWT with broad limits by varying the SWS period at the constant electron beam parameters. For a relatively small SWS corrugation depth ($l \ll R$), the Cherenkov synchronism condition can be expressed as

$$\frac{\Delta\lambda}{\lambda} \approx \frac{\lambda}{d}\frac{\beta_e}{(1+\beta_e\beta_{ph})}\frac{\Delta d}{d}.$$

For a BWT with an electron energy of 1 MeV, this yields

$$\frac{\Delta\lambda}{\lambda} \approx (0.4–0.5)\frac{\Delta d}{d}.$$

The results of numerical modeling showed that the possible frequency tuning bandwidth of a resonance BWT is limited from below and above by the critical frequencies of SWS and the below-cutoff section, respectively, and can reach up to 25% (at half-maximum power level). However, variation of the SWS period requires adjusting the waveguide insert length between the SWS and the below-cutoff section for optimization of the electron beam interaction with the concurrent electromagnetic wave.

Experimental investigations of the resonance BWT operating in a decimeter wavelength range were performed with a high-current electron accelerator of the Sinus-7 type [9]. The oscillator was optimized with respect to the vacuum diode impedance and the waveguide insert length between the SWS and the below-cutoff section. Variation of the insert length (Fig. 2) led to a change in the working frequency within ~3%. A multimode generation with a characteristic drop in the output power was observed at an insert length of ~0.7λ. In the optimum regime of operation at a frequency of 3.6 GHz, the BWT efficiency reached about 30%. At a cathode voltage of 1.2 MV and the electron beam current of 15 kA, the output radiation power amounted to 5.3 GW for a microwave pulse duration of ~25 ns (full width at half maximum, FWHM). The microwave radiation power was determined using calibrated dipole antennas, with integration over the directivity pattern. The energy measured by a calorimeter (analogous to that described in [2]) reached ~100 J.

Figure 3 shows typical pulse shapes of the cathode voltage, electron beam current, and microwave detector

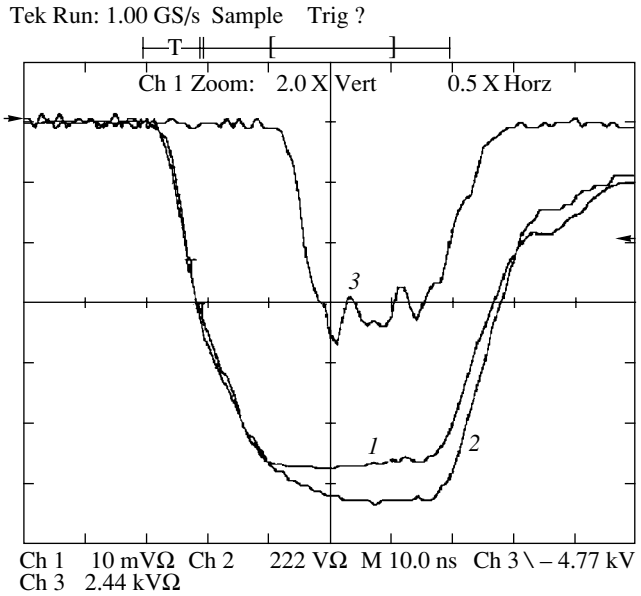

Fig. 3. Typical oscillograms of the (*1*) cathode voltage, (*2*) electron beam current, and (*3*) microwave detector signal.

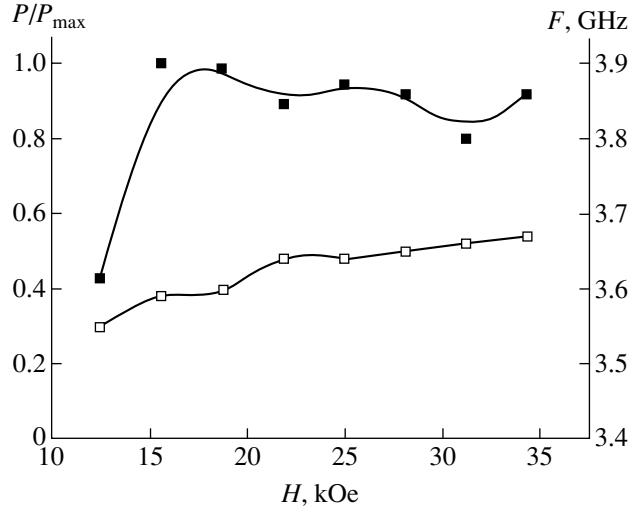

Fig. 4. Experimental plots of the output radiation power and working frequency versus focusing magnetic field strength (cathode voltage, 12 MV; beam current, 15 kA).

signal. The directivity pattern corresponded to a TM_{01} mode emitted from a horn antenna. The experimental efficiency, similar to that in the numerical modeling, changed rather insignificantly when the electron beam power was varied from 5 to 19 GW. The optimum diode impedance was about 80 Ω.

A plot of the output radiation power versus the focusing magnetic field (Fig. 4) exhibited a drop in the range of magnetic fields below 15 kOe. According to the results of numerical modeling this decrease in the output power is related to a partial loss of electrons from the beam to the SWS surface as a result of interaction with intense RF fields. As the electron beam energy decreases, the threshold shifts toward lower magnetic fields. The presence of a lower limit with respect to the focusing magnetic field strength can be also related to the cyclotron absorption of the electromagnetic field energy by the electron beam [10, 11].

In experiments with the SWS period changed from 38 to 48 mm, with the corresponding adjustment of the waveguide insert length, the working frequency could be varied within 15% (at half maximum power level), while the electron beam parameters and the focusing magnetic field remained unchanged.

Thus, improvement of the longitudinal distribution of the RF field as a result of the working TM_{01} mode reflections from the ends of the electrodynamic system and optimization of the electron beam interaction with both backward and concurrent electromagnetic waves allowed the resonance BWT efficiency to increase up to 30%. An important advantage of the resonance BWT in comparison to a usual relativistic BWT is a smaller interaction space length (~3λ), which decreases the energy consumption related to the focusing magnetic field. In a decimeter wavelength range, a BWT operating in a single-mode regime exhibited an output radiation power of about 5 GW. It was demonstrated that the working frequency of a resonance BWT can be varied to within 15% by changing the SWS period.

REFERENCES

1. B. V. Bunkin, A. V. Gaponov-Grekhov, A. S. El'chaninov, *et al.*, Pis'ma Zh. Tekh. Fiz. **18** (9), 61 (1992) [Sov. Tech. Phys. Lett. **18**, 299 (1992)].
2. A. V. Gunin, S. A. Kitsanov, A. I. Klimov, *et al.*, Izv. Vyssh. Uchebn. Zaved., Fiz. **39** (12), 56 (1996).
3. V. L. Bratman, N. S. Ginzburg, N. F. Kovalev, *et al.*, in *Relativistic Microwave Electronics* (IPF AN SSSR, Gor'kiĭ, 1979), pp. 249–274.
4. A. S. El'chaninov, F. Ya. Zagulov, N. F. Kovalev, *et al.*, Pis'ma Zh. Tekh. Fiz. **4**, 1443 (1978) [Sov. Tech. Phys. Lett. **4**, 584 (1978)].
5. S. D. Korovin, S. D. Polevin, A. M. Roitman, *et al.*, Pis'ma Zh. Tekh. Fiz. **20**, 12 (1994) [Tech. Phys. Lett. **20**, 5 (1994)].
6. V. K. Yulpatov, Izv. Vyssh. Uchebn. Zaved., Fiz. **13**, 1784 (1970).
7. B. Levush, T. Antonsen, A. Bromborsky, *et al.*, IEEE Trans. Plasma Sci. **PS-20** (3), 263 (1992).
8. V. P. Tarakanov, *User's Manual for Code KARAT* (BRA, Springfield, 1992).
9. S. D. Korovin and V. V. Rostov, Izv. Vyssh. Uchebn. Zaved., Fiz. **39** (12), 21 (1996).
10. A. S. Elchaninov, F. Ya. Zagulov, S. D. Korovin, *et al.*, *Proc. 4th Int. Conf. on High Power Electron and Ion Beams* (Palaiseau, 1981), Vol. 2, pp. 847–852.
11. É. B. Abubakirov, V. I. Belousov, V. N. Varganov, *et al.*, Pis'ma Zh. Tekh. Fiz. **9**, 533 (1983) [Sov. Tech. Phys. Lett. **9**, 230 (1983)].

Translated by P. Pozdeev